

Dissertation
submitted to the
Combined Faculties of the Natural Sciences and Mathematics
of the Ruperto-Carola-University of Heidelberg, Germany
for the degree of
Doctor of Natural Sciences

Put forward by

Fabian Klein

born in: Trier, Germany

Oral examination: 17.10.2018

Simulations of an accretion disk surrounding a supermassive black hole and its interaction with a nuclear star cluster

Referees:

APL. PROF. DR. RAINER SPURZEM

PROF. DR. CORNELIS P. DULLEMOND

To Theresia and Paul-Josef Jasiulek

Simulations of an accretion disk (AD) surrounding a supermassive black hole (SMBH) and its interaction with a nuclear star cluster

We investigate the time evolution of an AD surrounding a SMBH in an active galactic nucleus (AGN) and its dynamical interactions with a the nuclear star cluster (NSC). The AD is important in these interactions because of its dissipative force acting on the NSC stars, resulting in an increased mass flow to the SMBH and asymmetries in the phase space distribution due to its rotation. As the StarDisk project (Just et al., Kennedy et al.) only treated a static AD, viscous hydrodynamical simulations including gravity and self-gravity are used in this thesis to take dissipative feedback and lifetime checks of the AD into account. These simulations were performed using the PLUTO code along with additional modules written by Rolf Kuiper and equilibrium initial condition similar to Shakura & Sunyayev. The results were a quasi-static state as well as the confirmation of the scale-height assumptions from Kennedy et al. and the estimation of the accretion rate reproducing the expected result from Shakura & Sunyayev. Furthermore, the obtained data was used to interpolate the dissipative forces in the direct N-body code NBODY6++GPU and carry out a first test. The inclusion of more physics into the hydrodynamics as well as the advancement of the NBODY6++GPU project to real applications are both tasks for future research.

Simulationen einer Akkretionsscheibe (AS) um ein supermassives schwarzes Loch (SMSL) und ihre Wechselwirkungen mit einem zentralen Sternenhaufen

Wir untersuchen die Zeitentwicklung einer ein SMSL umgebenden AS in einem aktiven Galaxienkern (AGK) und ihre dynamische Wechselwirkung mit einem zentralen Sternenhaufen (ZSH). Die AS ist wegen ihrer dissipativen Kräfte, die auf die Sterne im ZSH wirken, sehr wichtig für diese Wechselwirkungen, welche in einem erhöhtem Massenfluss zum SMSL sowie Asymmetrien in der Phasenraumverteilung, ausgelöst durch die Rotation, führen. Da das StarDisk Projekt (Just et al., Kennedy et al.) die AS als statisch behandelt hat, wurden in dieser Arbeit viskose hydrodynamische Simulationen, welche auch die Gravitation und Eigengravitation beinhalten, durchgeführt, um die dissipative Rückkopplung und die Lebensdauer der Scheiben miteinzubeziehen. Diese Simulationen wurden mithilfe des PLUTO Codes unter Verwendung von zusätzlichen Modulen entwickelt von Rolf Kuiper und Gleichgewichtsbedingungen ähnlich denen von Shakura & Sunyayev durchgeführt. Das Ergebnis war ein quasi-statischer Zustand, welcher Annahmen zur Skalenhöhe von Kennedy et al. bestätigte und eine Abschätzung der Akkretionsrate konnte die erwarteten Resultate von Shakura & Sunyayev reproduzieren. Weiterhin wurden die gesammelten Daten verwendet, um durch Interpolation die dissipativen Kräfte im direkten N-Teilchencode NBODY6++GPU zu verwenden und einen ersten Test durchzuführen. Das Hinzufügen weiterer Physik in die Hydrodynamik bildet zusammen mit dem Voranbringen des NBODY6++GPU Projektes zur Durchführbarkeit von echten Anwendungen die Aufgaben für zukünftige Forschung.

Contents

1. Introduction and Motivation	1
1.1. quasi-stellar radio sources (QUASARS) and the history of Active Galactic Nuclei (AGN)	1
1.1.1. First discoveries	1
1.1.2. Radio astronomy reveals new objects	1
1.1.3. QUASARS and their optical counterparts	2
1.1.4. Confirmation of cosmological redshifts and new questions	3
1.1.5. Energy source and central engine	4
1.1.6. The “Black Hole Paradigm” becomes the accepted theory	4
1.1.7. Unified models	5
1.2. Emission as a proof for the structure of AGN	7
1.2.1. Detailed analysis of structure of AGN Accretion Disk (AD) of the paper series starting from Collin-Souffrin (1987)	10
1.3. Newer developments explored with a review paper	13
1.3.1. “The AGN Family: New Multi-wavelength observations” (Netzer 2018)	14
1.3.2. “Mapping and Modelling the Broad Line Emitting Region (BLR) and Measuring BH Masses” (Netzer 2018)	15
1.3.3. “Accretion Disks and Disk Winds” (Netzer 2018)	16
1.3.4. “Star Formation Galactic-Scale Winds Mergers and Feedback” (Netzer 2018)	16
1.3.5. Cosmology: “Something Wrong: All AGN-Based Methods” (Netzer 2018)	17
2. Physics of Accretion Disks	21
2.1. Theoretical foundations of α -Disks	21
2.1.1. Disk structure	24
2.1.2. Profiles derived in Shakura and Sunyaev (1973)	25
2.1.3. More rigorous proof in other papers	26
2.2. Fluid dynamics description	28
2.2.1. Time evolution equations	28
2.2.2. Viscosity	29
2.2.3. Radiation hydrodynamics	33
2.2.4. Spherical coordinates	37
2.2.5. Gravitational forces	37
2.2.6. Self-gravity	38

2.3.	Equilibrium initial conditions	39
2.3.1.	Assumptions	39
2.3.2.	Derivations from vertical force-balance	39
2.3.3.	Determination of pressure profile	41
2.3.4.	Derivation of \mathbf{v}_φ from radial force balance	41
2.3.5.	Normalisation constant for ρ	42
2.3.6.	Self-gravity	43
2.3.7.	On the scale-height	43
2.3.8.	Resulting initial conditions	44
2.3.9.	Viscosity corresponding to the initial conditions	44
2.3.10.	Toomre Q	45
2.4.	The drag force as the force the stars feel from the AD for N-body simulations	48
3.	Numerical simulations using the PLUTO code and NBODY6++GPU	51
3.1.	Astrophysical system	51
3.2.	The PLUTO Code	53
3.2.1.	Basic discretisation scheme	53
3.2.2.	Available grids	54
3.2.3.	Riemann solver	55
3.2.4.	Time discretisation schemes	55
3.2.5.	Interpolation schemes	56
3.2.6.	Modules by Rolf Kuiper	59
3.3.	Set-up	64
3.3.1.	Target system	64
3.3.2.	Parameters resulting from the chosen system	65
3.3.3.	Units	65
3.3.4.	Boundary conditions	66
3.4.	Numerical simulations without self-gravity	70
3.4.1.	Initial conditions	70
3.4.2.	Results in axis-symmetric 2D simulations	70
3.4.3.	Results in 3D	82
3.5.	Numerical simulations with self-gravity	90
3.5.1.	Initial conditions	90
3.5.2.	Results in axis-symmetric 2D simulations	90
3.5.3.	Results in 3D	101
3.6.	Using the data to do simulations with NBODY6++GPU	112
3.6.1.	Creating a read-in module for the hydrodynamic simulation data	112
3.6.2.	Extrapolation of hydrodynamic simulation data to smaller radii	116
3.6.3.	First preliminary test	119
4.	Conclusions and Outlook	121
4.1.	Conclusions for the hydrodynamical simulations with PLUTO	121
4.2.	Conclusions for the hydrodynamical simulations with NBODY6++GPU	122

4.3. Outlook	122
A. List of Acronyms	127
B. Bibliography	131

1. Introduction and Motivation

1.1. quasi-stellar radio sources (QUASARs) and the history of Active Galactic Nuclei (AGN)

This subsection describes the study of QUASARs from their very beginnings to the present day. This is mostly based on Shields (1999).

1.1.1. First discoveries

The first evidence of AGN already appeared at the beginning of the 20th century when astronomers tried to determine whether the so called “spiral nebulae” were distant objects or not. Essentially, they were asking the question if there is only one galaxy or several of them. According to Shields (1999) Fath at Lick observatory first discovered AGN emission lines in NGC 1068. This happened while creating a spectroscopic survey of several “spiral nebulae” in order to prove that they are an unresolved collection of stars which should have a continuous spectrum with stellar absorption lines. He described the spectrum as “composite, showing bright and absorption lines” (Shields 1999). Many astronomers, among them Hubble who said their spectra were “planetary nebula” type, had confirmed these lines in many spiral nebulae. Moreover, they had also found that the emission lines were covering a substantial range of wavelengths. Thus, Seyfert started the first real study of the galaxies with nuclear emission lines in 1943. Shields (1999) also describes Seyfert’s method. He superimposed the spectra emission lines with a G-type solar spectrum and discovered variations in the width of the lines for the objects considered. This introduced the main distinction between the narrow forbidden and permitted lines of e.g. NGC 1068 and the broad hydrogen lines in e.g. NGC 4151. In honour of his work galaxies with high-excitation nuclear emission lines are called “Seyfert Galaxies”. As confirmed in Shields (1999) Seyfert’s paper was, unfortunately, not enough to start the new field. The final impetus was a newly developing field that emerged in the wake of the new radio technology.

1.1.2. Radio astronomy reveals new objects

Again supported by Shields (1999) Jansky found the first astronomical radio source, located in the Sagittarius constellation in the densest part of the Milky Way (MW), while investigating the sources of static interfering with trans-atlantic radio communications at Bell labs. This confirmed suspicions of astronomical radio sources already raised by Maxwell at that time and disproved that the earth’s ionosphere is repelling

1. Introduction and Motivation

all astronomical radio signals. Initially, he suspected the sun as the source of the radiation. Later, he rejected this idea in favour of a more distant astronomical object as the periodicity was a sidereal day and not a solar day. Furthermore, the signal was strongest when pointing the antenna at Sagittarius. While most professional astronomers did not take notice of Jansky's work it inspired electrical engineer and amateur radio operator Grote Reber to construct a radio telescope in his backyard near Chicago in 1937. Using this, he confirmed Jansky's discoveries, achieved publications in a journal and created a radio map of the sky after refusing a research appointment. This should become the basis for the rapid growth of radio astronomy after the second world war. He also was the first to note that the "ratio of radio radiation to optical light was vastly larger for the MW than for the sun" (Shields 1999). People and research effort originating from radar research during the second world war were redirected to radio astronomy after it had ended. This resulted, most notably, in the groups of Cambridge and Manchester in the UK as well as the CSIRO in Australia.

By the means of surveys, discrete sources were discovered. An example is the MW survey by Hey, Parsons and Phillips in 1946. Specifically, Cygnus A. Bolton, Stanley and Slee (1949) were finally able to identify some optical counterparts for the radio signals aided by sea-cliff technique observations (interferometry using the sea surface as a second reflector). Positions determined by Smith enabled optical identification of e.g. Cyg A by Baade and Minkowski in 1954. This then led to further investigations determining the distance to be 31 Mpc as well as high luminosities (determined from $H_0 = 540 \text{ km s}^{-1} \text{ Mpc}^{-1}$ as the Hubble constant at that time) of $8 \times 10^{42} \text{ erg s}^{-1}$ (radio) and $6 \times 10^{42} \text{ erg s}^{-1}$ (optical). Measurements by Hanbury Brown, Jennison and Das Gupta in 1952 also revealed that Cyg A was an elongated source with dimensions roughly $2' \times 0.5'$

1.1.3. QUASARs and their optical counterparts

As described in Shields (1999) the last step on the road to AGN was the discovery of so called quasar (Later reduced to "quasi-stellar object" QSO). After Minkowski's studies of radio galaxies Allan Sandage and Maarten Schmidt undertook the task of optical identification of the radio galaxies found. They worked together with Thomas A. Matthews, who had new accurate positions of them on hand. Sandage first found a stellar object of 16th magnitude "with a faint nebulosity" (Shields 1999) and broad emission lines in unfamiliar wavelengths as well as being variable in intensity. Additionally, excess ultraviolet emission lines were present. As many more objects like these were found, names were developed for them such as "quasi-stellar radio sources" (QSRs), "quasi-stellar sources" (QSS) and finally QUASARs which became established. While initially it was thought that there "was a remote possibility that it may be a distant galaxy of stars", it was generally thought these objects are "a relatively nearby star with most peculiar properties" (both Shields (1999)). The breakthrough was on February 5th, 1963 when Schmidt identified a part of the spectrum as the Balmer lines with a redshift of $z = 0.16$. After consultation with some

colleagues (Jesse L., Greenstein and J.B. Oke) Schmidt learned that Oke had also identified a $H\alpha$ line in this object and that Greenstein had obtained a spectrum that suggested a redshift of $z = 0.37$ for another object. After these results were published it was clear that the spectrum was just a very redshifted one. Despite of initially claiming “the objects might be Galactic stars with a very high density, giving large gravitational redshift” (Shields 1999) it became clear that this was not reconcilable with the width of the lines and the presence of forbidden lines. Amongst several explanation models it was also proposed that the redshift was due to Hubble expansion, thus making the objects extragalactic. Nonetheless, the extreme optical brightness of the object “10-30 times brighter than the brightest giant ellipticals” (Shields 1999), the radio surface brightness much larger than for radio-galaxies, an estimated distance of 500 Mpc as well as a nuclear region of 1 kpc in diameter were still seen as puzzeling. The reason was that those numbers would imply a time-scale of 1.0×10^5 yrs and a total radiated energy of 1.0×10^{59} erg. After some more discussions, the cosmological redshift was accepted, because the width of the emission lines would require an object of $M \geq 1.0 \times 10^9 M_{\odot}$ in order to explain the redshifts as gravitational (Hoyle and Fowler 1963a). While the debate about the central energy source (though a “collapsed object” was proposed according to Hoyle and Fowler (1963a)) continued, several different classes of QUASARs were discovered, also in the radio quiet regime. For the latter, see e.g. studies of Sandage, although his initial numbers were reduced by later works.

1.1.4. Confirmation of cosmological redshifts and new questions

Through their high redshifts, the QUASARs sparked some cosmological and extragalactic science. These studies confirmed QUASARs to have roughly similar chemical abundances as found in our galaxy. This suggests, they have reached modern chemical composition much earlier. Also, the abundance of neutral hydrogen in intergalactic space (see e.g. Gunn and Peterson (1965) who set a tight upper limit for it) was found to be similar to the one of QUASARs. Furthermore, cosmological redshifts were confirmed more rigorously by discovering matching redshifts for galaxy clusters with QUASARs in them (Gunn 1971). One more point was identifying the “fuzz” (Shields 1999) surrounding the quasar objects as the presence of a host galaxy (Kristian 1973).

After this identification, the next big step was the analysis of similarities with the Seyfert galaxies. The similarities were seen (e.g. broad wings) and the deeper analysis lead to the two distinct regions in AGN, namely the Narrow Line Emitting Region (NLR) and Broad Line Emitting Region (BLR). The physical phenomenon was further investigated focusing on the energy source, the continuum source, emission-line regions as well as which factors determine whether a galaxy has an AGN or not (see Shields (1999) and the references therein). As Subsection 1.2 goes into much detail about the emission regions, this will not be discussed at this point.

1.1.5. Energy source and central engine

The question of how the AGN is powered was a debate sparked even before the discovery of their redshifts and inspired many ideas that all had AGN as “sites of concentrated, violent activity” (Shields 1999). These included chain reactions of supernovae in dense nuclear star clusters (Burbidge 1961), mass-death of massive stars in a coeval star cluster at the end of their lifetime (Cameron 1962) and a supermassive star (Hoyle and Fowler 1963a;b) of up to $1.0 \times 10^8 M_{\odot}$ as “a source of gravitational and thermonuclear energy” (Shields 1999). Also, the model of a Super Massive Black Hole (SMBH) accreting mass was proposed by Salpeter (1964) as well as Zel’dovich (1964). This model would have the correct energy (material gradually spinning until reaching the innermost orbit) from a reasonable mass as well correct time-scales. Salpeter already imagined a turbulent momentum transport allowing matter to come closer to the central SMBH. This already points to the much later Shakura and Sunyaev (1973). Despite of these theories’ many merits it received limited attention. This finally changed through Lynden-Bell (1969), who argued that the SMBH could represent a “dead quasar” (Lynden-Bell 1969) and should be common in galactic nuclei. The tracing is possible via the mass-to-light ratios of nearby galaxies. This would also explain the prevalence of AGN in earlier periods of the universe. Additionally, Lynden-Bell (1969) also explored the disk structure that should be present in this accreting scenario, its predicted thermal emission and its dissipation by magnetic and turbulent processes. Effective temperatures of $\approx 1.0 \times 10^5$ K are expected which one would need for photoionisation and line emission. It is argued that “with different values of the [black hole mass and accretion rate] these disks are capable of providing an explanation for a large fraction of the incredible phenomena of high-energy astrophysics, including galactic nuclei, Seyfert galaxies, quasars and cosmic rays.” (Shields 1999). Further evidence for the relativistic nature of the system came from theory and further observations as described in Shields (1999).

1.1.6. The “Black Hole Paradigm” becomes the accepted theory

After not being included in a “widespread effort” (Shields 1999) for many years the understanding of AGN as a SMBH with an Accretion Disk (AD) around it were put in a new light after the discovery of the first stellar mass black holes. Some of the discoveries from X-Ray observations included binary-star systems where one component being a neutron star or black hole. In the neutron star case these systems, known as binary “X-ray pulsars”, are emitting X-ray radiation by gas drawn from the non-compact part of binary impacting on the compact component. Another class of systems, e.g. investigated in Oda et al. (1971), shows no periodic variations like the before-mentioned. Instead, they possess rapid flickering implying a much smaller size of the object. Also, orbit analysis gave masses too large for a neutron star (see e.g. Webster and Murdin (1972), Tananbaum et al. (1972)). The final conclusion, as found by Thorne and Price (1975), was that one sees X-ray radiation created by high temperature gas from the non-compact companion spiralling into a black hole

via a disk. This discovery, together with cataclysmic variables, protostars and last but not least AGN fueled advances in AD physics with the α model as prominently presented in Shakura and Sunyaev (1973), Novikov and Thorne (1973). This model still is the standard model used up to the present day. A more detailed analysis, primarily of Shakura and Sunyaev (1973) as Novikov and Thorne (1973) primarily determines relativistic corrections relevant for the innermost regions, can be found in Section 2.1. More details on the structure and how well it described the observed spectra can be found in Subsection 1.2. In short words a geometrically thin disk is assumed and the angular momentum transport and local energy release is described by the stresses encoded in the dimensionless α -parameter. Also, the disk is divided in three radial regions according to dominating pressure (radiation pressure/thermal pressure) and electron scattering and the opacity source. Energy production in AGN is primarily located in the innermost region dominated by radiation pressure and electron scattering. Thus, atmosphere and interior are electron scattering dominated modifying the emission spectrum from of a blackbody spectrum. Mostly, AD models can explain the bulk of aspects of the observed spectra (blue continuum, X-ray radiation) as shown in Shields (1999).

The model of thermal emission turned up to be too simplified for a full description. As detailed in Shields (1999) one needs additional X-ray heating processes in order to explain continuum variations faster than all possible thermal processes. Another problem is the polarisation being far too low for an electron scattering dominated atmosphere. Both of these problems are still under ongoing investigation.

1.1.7. Unified models

As a wide range of QUASARs was discovered with a wide range of intensities and emission line widths they were all initially seen as separate objects. When the connection to Seyfert galaxies became known, the idea emerged that some of the features only dependent on the angle we are looking at the system at. As Urry and Padovani (1995) describes the primary difference whether the system is radio-loud or radio-quiete. Radio-loud means

$$\frac{F_{5\text{GHz}}}{F_{\text{optical, B}}} \geq 10, \quad (1.1)$$

where $F_{5\text{GHz}}$ is the flux in the 5 GHz band and $F_{\text{optical, B}}$ is the optical flux in the B-Band (Kellermann et al. 1989). The observed objects were grouped in different categories as shown in Tab. 1.1. As seen in the table, apart from radio-strength, the strength and narrowness/broadness of the optical lines is the main grouping criterion. The highest intensities are seen in the Blazars which have similar subcategories. It should be noted that this table is by no means exhaustive. As explained in Urry and Padovani (1995) all of the effects can just be interpreted as results of different viewing angles of the same type of system. Fig. 1.1 illustrates the way unification works. Like e.g. Urry and Padovani (1995) expresses radio emission is collimated in the direction of the jet as the jet is the major source of them. Consequently, radio emission is only strong if the jet-emitting side of the AGN is facing the observer. One

1. Introduction and Motivation

of the main reasons for this is special relativistic beaming (“Headlight effect”), which is being caused by the special relativistic Doppler-factor which is, according to e.g. Urry and Padovani (1995), given by

$$\delta = [\gamma(1 - \beta \cos \theta)]^{-1}, \quad (1.2)$$

where $\gamma = (1 - \beta^2)^{-1/2}$ is the special relativistic γ factor, θ is the line of sight angle, $\beta = v_{\text{bulk}}/c$ is the relativistic β factor, c is the speed of light and v_{bulk} is the bulk velocity of the emitting matter. The specific intensity for this beaming is, as mentioned e.g. in Urry and Padovani (1995), given by

$$I_\nu(\nu) = \delta^3 I'_\nu(\nu'), \quad (1.3)$$

where $I_\nu(\nu)$ is the specific intensity in the observer’s frame, ν is the frequency of the radiation in the observer’s frame, I'_ν is the specific intensity in the rest frame of the emitter and ν' is the frequency of the radiation in the emitter’s frame. Even small aberrations from looking at the source head on, especially at highly relativistic speeds, cause major differences in the observed intensities that depend on the third power of the Doppler-factor as seen in equation (1.3). As the emitting matter of the AGN is mostly at highly relativistic speeds it is also often hard to even detect its radio emissions when the viewing angle is not good enough. In conclusion, all the radio-quiet AGN are, in the idea of unification, those viewed under the “backwards” angles i.e. facing away from the jet. This can clearly be seen in Fig. 1.1. The differences in the optical lines observed from AGN are, in this theory, related to an obscuring toroidal object of matter existing around the accretion disk. In Fig. 1.1 it really is a torus, however, more modern points of view acknowledge that the shape is probably more irregular. This is discussed in Schartmann et al. (2007) and a graphical representation can be found in Fig. 1.2. Despite of these changes, its effect stays the same as before. Mainly, the broad line region can be, depending on the viewing angle, obscured by the “torus“. Evidence of this can be found by the presence of some highly polarised (and thus scattered) broad line components and parts of the X-Ray continuum in otherwise no broad-line showing objects. This can for example be seen when comparing certain subtypes of Seyfert I with certain subtypes of Seyfert II galaxies. Again, the angle under which the object is seen mainly determines the observations made. These, for the case of the optical lines, incorporate the presence or absence of broad and narrow lines as well as the presence of the scattered optical lines. Summed up unification is able to redeem the wide variety of partly similar objects seen at roughly the same general spots and redshifts as the same physical system only varying in parameters like mass or material supply. This concludes the excursion to the history of AGN observations and the development of theories.

		Higher Luminosity					
		↓↓				↓↓	
		Type 2	Narrow, weak	Type 1	Broad, bright	Type 0	Unusual
Radio quiet	}	Seyfert II	same SI	Seyfert I	not luminous		
				QSO	$M_B < -23.5$		
Radio loud	}	NLRG	Narrow Radio Farnoff-Riely I FR II symm. radio jets	BLRG	Radio galaxy	Blazars	BL Lac OVV HPQ... Highly variable
				SSRQ	Steep spect.		
				FSRQ	Flat spect. Radio Beaming		
Biggest Luminosity							



 Decreasing angle to line of sight

Table 1.1.: Inspired by Table 1 in Urry and Padovani (1995) illustrating the categorisation of some common AGN objects. Abbreviations: **O**ptically **V**iolent **V**ariable, **N**arrow **L**ine **R**adio **G**alaxy, **B**road **L**ine **R**adio **G**alaxy, **Q**uasi **S**tellar **O**bject, **S**teep **S**pectrum **R**adio **Q**uasar, **H**ighly **P**olarised **Q**uasar

1.2. Emission as a proof for the structure of Active Galactic Nucleus (AGN)

As direct observations of the internal structural of AGN are not possible one has to deduce the structure properties from the emission and absorption features of the entire electromagnetic spectrum received from the AGN. For a long time an Accretion Disk (AD) has been hypothesized to be the essential driving part of the luminosity of AGN. One of the most famous examples is the pioneering paper Shakura and Sunyaev (1973). Finally, Malkan and Sargent (1982) gave, according to Collin-Souffrin (1987), the first observational support for this hypothesis in 1982 by showing that the optical and UV continuum of the quasars can be interpreted as a thermal emission spectrum of an AD. The optical and UV emission can be split up in the Broad Line Emitting Region (BLR) (e.g. Collin-Souffrin (1987)) and the Narrow Line Emitting Region (NLR). As Collin-Souffrin (1987) and many other works explain the BLR is thought to be composed of an assembly of small clouds ionised by the non-thermal continuum produced by the central engine of the AGN. This can be inferred by the fact that the effective emitting volume is much smaller than the typical size of the emitting region. This can be inferred from the "variability time scale and the ionization parameter" (Collin-Souffrin 1987). In Collin-Souffrin (1986) Collin-Souffrin describes the general properties of the BLR. Initially, she introduces High Ionisation Line (HILs) and low ionization lines (LIL) as two distinct sets of lines probably emitted by different regions inside of the BLR. HILs are defined as the L_α , CIII, CIV, HeI, HeII, NV and OVI lines, whereas the Balmer, MgII, CII and FeII are defined as the LILs. Using detailed arguments from ionisation models, Coullin-Souffrin proves that and also gives hints to other proofs explicitly mentioning the one from B. Wills

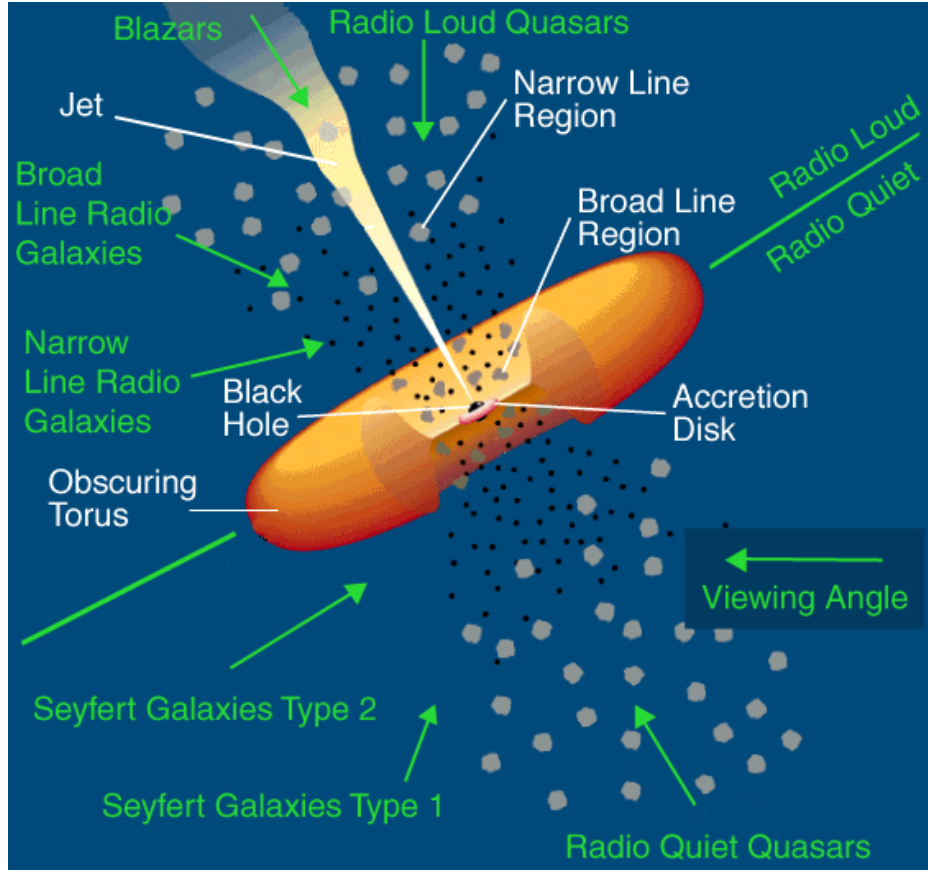


Figure 1.1.: Sketch of AGN system as imagined by the unification showcasing the different types seen under certain viewing angles along with a obscuring torus. No clear creator determinable for this figure. It was taken from Molina (2018), but it appears in many other places. It seems to be a coloured and annotated version of Fig. 1 in Urry and Padovani (1995)

from the same IAU symposium as Collin-Souffrin (1986). The electron density can approximately be determined by looking at the line intensities (see e.g. Davidson and Netzer (1979)). The upper bounds are $\approx 10^9 \text{ cm}^{-3}$ or $\approx 10^{12} \text{ cm}^{-3} - 10^9 \text{ cm}^{-3}$ for one single source region and two separate source regions, respectively. The temperature is estimated to be $< 30\,000 \text{ K}$ pointing to the fact that ionisation in the HIL region must be radiative and not collisional. Furthermore, Collin-Souffrin estimates an upper limit for the size of the BLR from the time variation of the emission lines for Seyfert Galaxies to $0.1 \text{ pc} < R < 1 \text{ pc}$ as an upper limit. The ionisation parameter is also introduced as the “ratio of the ionizing photon number density to the electron density” (Collin-Souffrin 1986).

$$U = \frac{L_\nu}{\alpha'^4 \pi R^2 c n_e}, \quad (1.4)$$

where U is the ionisation parameter, L_ν is the luminosity of a continuum source at the Lyman edge, α' is the spectral index of the Lyman continuum, c is the speed

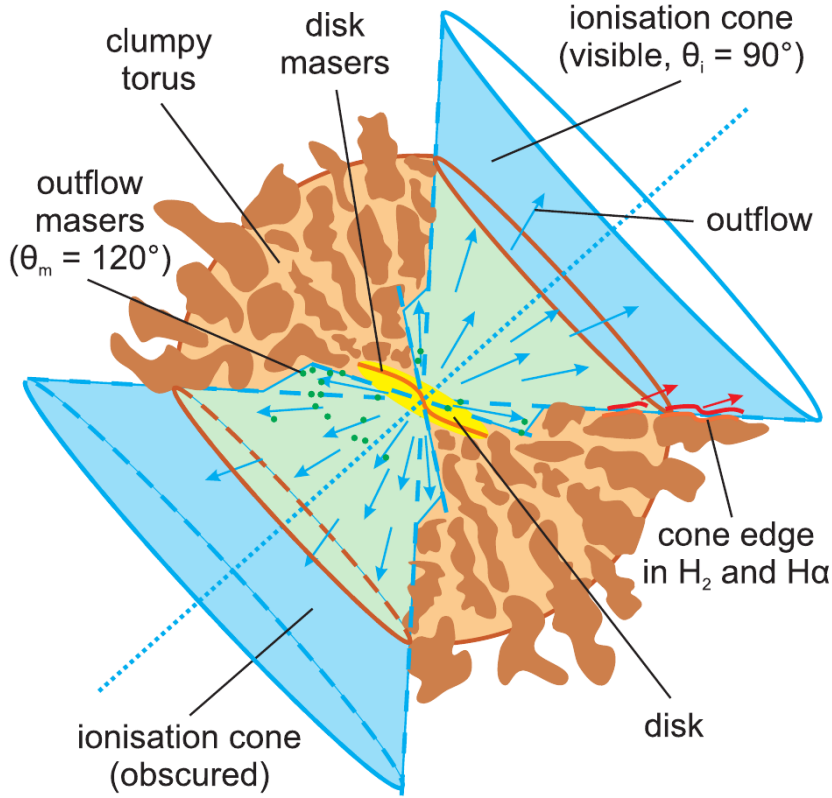


Figure 1.2.: A more realistic illustration of the obscuring "torus" and its position within the central part of the AGN, taken from Schartmann et al. (2007).

of light n_e is the electron density and R is the distance from the continuum source. Detailed photoionisation models can yield line intensities dependent on said ionisation parameter for the radiative ionisation mechanism present in the HIL region. From that it can be concluded that not all of the HIL originate from the same region for all AGN objects. Collin-Souffrin also draws first conclusions of the geometrical structure in Collin-Souffrin (1986). Starting from the consensus of the BLR consisting of a "large number of high-velocity clouds" (Collin-Souffrin 1986) filling only a tiny fraction of the overall emitting volume of the system Collin-Souffrin draws some conclusions. Firstly, she mentions, after listing the observational and theoretical evidence for the BLR assumption, that a "disk shaped structure" (Collin-Souffrin 1986) could be present. In this structure the emitting region would be "confined to a thin outer shell" (Collin-Souffrin 1986). As the column density N is the most important parameter for these emitting regions, detailed photoionisation models (Kwan and Krolik 1981) predict a limited range of $1 \times 10^{22} \text{ cm}^{-2}$ to $1 \times 10^{23} \text{ cm}^{-2}$. The disk as the emitting object can be supported with some further arguments described in Collin-Souffrin (1987). Collin-Souffrin explains that Keplerian motions are not the likely reason for the line width

1. Introduction and Motivation

and line-profiles (see references in Collin-Souffrin (1987)) as quasi-stellar radio sources (QUASARs) and AGN have similar profiles roughly independent of the luminosity. These profiles would imply Keplerian rotation at distances $10^3 - 10^4 R_S$, where R_S is the Schwarzschild radius., from the centre which contradicts the fact that some of the emitting gas should also be at larger distances. The problem of the missing narrow emission lines from face-on seen disks, as inferred by the model showcased in Collin-Souffrin (1987), can be overcome by assuming a slight warping of the disk. Alternatively, the perpendicular jet released should make the object appear as a BL Lac object also resolving the issue. In the case of not having enough UV and X-ray continuum energy in order to account for BLR lines in AGN or QUASARs, another discrepancy emerges. This discrepancy is that this lead to contradistinctions in column densities, which can also be resolved by assuming a geometrically thin disk illuminated from above as described in Collin-Souffrin (1987). In the same paper, the dissipation of gravitational energy in the disk is also mentioned as an energy loss mechanism. Collin-Souffrin (1987) stresses theoretical arguments for the disk to be the source of the emissions. The disk would give a natural formation and confinement mechanism for the clouds.

The models presented in Collin-Souffrin (1987), using the α disk formalism of Shakura and Sunyaev (1973) as a basis, are able to explained the emission as coming from an optically thin layer of the disk. The power source is the heating by the down-scattered part of the non-thermal continuum from the AGN. Furthermore, hard X-ray heating of the is presented as the source of the “missing energy” in the budget of the BLR (see reference in Collin-Souffrin (1987)) as well as the infra-red $5 \mu\text{m}$ bump. One can thus reproduce some features of the line emission by the disk model presented here. Temperatures are estimated to be in the $1 \times 10^3 \text{ K}$ range, but are admittedly not modelled very well in Collin-Souffrin (1987). This is addressed in Collin-Souffrin and Dumont (1990) and Dumont and Collin-Souffrin (1990b).

1.2.1. Detailed analysis of structure of AGN AD of the paper series starting from Collin-Souffrin (1987)

Collin-Souffrin and Dumont (1990) describes the radial structure of the disk in more detail and gives hints for its vertical structure. Also, the X-Ray illumination by the central engine is included more rigorously, but still limited to luminosities $L_{\text{bold}} \leq 1 \times 10^{46} \text{ erg s}^{-1}$. In terms of radial range the range $R > 10^2 R_{\text{SW}}$ is looked upon, for reasons of not treating self-consistent gravitating disc structure as well as gravitational instabilities due to self-gravity or the surrounding star-cluster of the AGN. Collin-Souffrin and Dumont again adopt the α disk formalism and assume a radiative X-Ray continuum heating for $R > 10^4 R_{\text{SW}}$.

1.2.1.1. Disk without illumination

Collin-Souffrin and Dumont (1990) treats a disk without illumination. It is assumed that “the gravitational energy release $D(R)$ ” (Collin-Souffrin and Dumont 1990), equal

to the radiation flux of the disk, is given by

$$D(R) = \frac{3GM\dot{M}_{\text{BH}}}{8\pi R^3} \text{erg cm}^{-2} \text{s}^{-1}, \quad (1.5)$$

where G is the gravitational constant, M_{BH} is the mass of the central black hole and \dot{M} is the accretion rate. The geometrical thickness $H(R)$, is estimated by “twice the scale-height of a gas in hydrostatic equilibrium assuming a constant temperature” (Collin-Souffrin and Dumont 1990) as

$$H(R) = 2c_{\text{S}0}R^{\frac{3}{2}}(GM_{\text{BH}})^{-\frac{1}{2}} \text{cm}, \quad (1.6)$$

“where $c_{\text{S}0}$ is the sound velocity at the disk centre” (Collin-Souffrin and Dumont 1990). The “disk centre” is the equatorial plane. This equation is equivalent to equation (2.15) taken from Shakura and Sunyaev (1973) and the later derived equation (2.124). The additional factor of two is just a matter of definition as shown in the calculations leading to equation (2.124). Using the fact that gas pressure p_{gas} dominates in the outer regions ($R > 1.0 \times 10^2 R_{\text{S}}$, these are the regions considered later in the simulations) one can conclude

$$H(R) = 2 \left(\frac{k_{\text{B}}T_{\text{c}}(R)}{\mu m_{\text{p}}} \right)^{\frac{1}{2}} R^{\frac{3}{2}} (GM)^{-\frac{1}{2}} \text{cm}, \quad (1.7)$$

where $T_{\text{c}}(R)$ is the temperature in the equatorial plane, μ is the mean molecular mass, k_{B} is Boltzmann’s constant and m_{p} is the proton mass. The accretion rate is given by

$$\dot{M} = 2\pi H(R)Rn_{\text{c}}(R)m_{\text{p}}v_{\text{R}} \text{g s}^{-1}, \quad (1.8)$$

where $n_{\text{c}}(R)$ is the density in the equatorial plane and v_{R} is the radial velocity given by

$$v_{\text{R}} = \alpha c_{\text{S}} \frac{H}{R}. \quad (1.9)$$

α is the parameter from Shakura and Sunyaev (1973) and is “assumed to be a constant in the disk and (...) of the order or smaller than unity” (Collin-Souffrin and Dumont 1990). The effective temperature is defined as the one generated through gravitational energy release as

$$\sigma T_{\text{eff}}^4 = D(R), \quad (1.10)$$

where σ is the Stefan-Boltzmann constant. As stated in Collin-Souffrin and Dumont (1990) the temperature in the equatorial plane is connected to to the effective temperature T_{eff} T by

$$T_{\text{c}} \approx T_{\text{eff}}(0.75\tau)^{\frac{1}{4}}, \quad (1.11)$$

“where τ is the mean optical thickness and is much larger than units” (Collin-Souffrin and Dumont 1990). Furthermore, the surface temperature, which is important for emission, is stated to be very close to the effective temperature by Collin-Souffrin. Also, Collin-Souffrin and Dumont (1990) explores the simplifications if $\tau < 1$ reducing

1. Introduction and Motivation

equation (1.11) to

$$T_c \approx T_{\text{eff}} \tau^{-\frac{1}{4}}. \quad (1.12)$$

These equation allow to derive the radial structure of the disk in case the mean opacity is known. Collin-Souffrin concludes that the disk is optically thick in its inner parts and optically thin in the outer parts as the surface density decreases with increasing radius (mass-conservation). The surface temperature is mentioned to decrease via $R^{-\frac{3}{4}}$ (akin to the profile derived in Shakura and Sunyaev (1973) for region “a”) and T_c also follows a radial variation. An important fact to be mentioned is that the disk is vertically isothermal in the optically thin outer regions and in the range of 1×10^3 K to 1×10^4 K for disk around stars and 1×10^3 K for massive disks according to Collin-Souffrin and Dumont (1990). Collin-Souffrin and Dumont (1990) justifies the vertically constant temperature with the “thermostatic effect of the atomic and line cooling which is a strongly temperature-dependent function”. By again looking at the introduction if Collin-Souffrin and Dumont (1990), we find that the “inner” regions here refer to the interval

$$R \in [1.0 \times 10^2 R_S, 1.0 \times 10^3 R_S], \quad (1.13)$$

whereas the “outer” regions refer to the interval

$$R \in [1.0 \times 10^3 R_S, 1.0 \times 10^4 R_S]. \quad (1.14)$$

1.2.1.2. Disk with illumination

Now, Collin-Souffrin considers a non-thermal continuum that is illuminating the disk, causing heating and ionisation as long as the column density allows X-Ray photons to penetrate into the equatorial plane. Moreover, as shown in the subsequent paper Dumont and Collin-Souffrin (1990a) the assumption of a continuum extending up to 100 keV along “with a spectral index close to or smaller than unity” (Collin-Souffrin and Dumont 1990) results in gas of column density $1 \times 10^{25} \text{ cm}^{-2}$ heated up to 7×10^3 K. At higher column density (increases for decreasing radius) the penetrating length of X-rays becomes smaller, eventually becoming less than the disk height. “this radiatively heated layer is optically thin to visible radiation” (Collin-Souffrin and Dumont 1990). In this radial region, the disk will be hotter than without illumination changing from a infra-red molecular emission to atomic line spectrum in visible and ultraviolet. The strong cooling outside of this region leads to the separation into a thin hot radiative outer layer, that has most of the mass flow, and a cold inner layer that is gravitationally heated. The inner layer can be either optically thin or thick, critically depending on the amount of dust (Explored in more detail in Collin-Souffrin and Dumont (1990)). At exactly the boundary (R_{25}) between the regions it is said to be isothermal both vertically and horizontally at roughly 1.0×10^3 K. Fig. 1.4 displays the profiles resulting from the careful calculations in the paper, using the different regimes and regions as defined in Fig. 1.3 and Tab. 1.2. It should be noted that the radius dubbed “ ρ ” in the paper is in units of $1.0 \times 10^4 R_S$. The radial range considered

1.3. Newer developments explored with a review paper

Regime	T	Opacity dominated	Regime	$\rho <$
A	$T_c \geq 2 \times 10^4 \text{ K}$	by e^- scattering	1	$0.14\alpha^{-\frac{2}{9}} f_\epsilon^{-\frac{4}{9}} f_L^{\frac{2}{3}} L_{44}^{-\frac{2}{9}}$
B	$3 \times 10^3 \text{ K} < T_c < 1 \times 10^4 \text{ K}$	by Atomic processes	2	$3.65\rho_1$
C	$1.4 \times 10^3 \text{ K} < T_c < 3.0 \times 10^3 \text{ K}$	by Molecules	3	$4.65\rho_2$
D	$T_{\text{equil}} \approx 1.4 \times 10^3 \text{ K}$	N/A	4	$> \rho_3$
E	$T_c < 1.4 \times 10^3 \text{ K}$	by grains		

Table 1.2.: Explanation of Regions and Regimes as used in Tab. 1.3, radius again in units of $1.0 \times 10^4 R_S$, $T_c = T_c$ is the temperature in the equatorial plane, H is the thickness, n_c is the density in the equatorial plane and τ is the optical thickness (opacity related)

corresponds to the range later considered in this thesis where $R \geq 1.0 \times 10^3 R_S$ will be considered. Thus, we should see some similarities. Thus, we are dealing with the parts dubbed “outer parts” in this paper series later. We can see the growing thickness of the disk and the varying central temperature depending on the heating process and X-ray penetration depth. These results are more detailed than the ones presented in Shakura and Sunyaev (1973). The thickness is shown to almost linearly grow over the entire radial range, i.e. no difference caused by self-gravity, as assumed in later models, can be seen here. The gas pressure is shown to dominate in all regions in the model presented here, which is an interesting result. Consequently, it should be possible to do simulations without its inclusion for wide ranges. However, for a full treat, especially for lower R is required for acquiring more complete solutions. This alternative models, slightly based on Shakura and Sunyaev (1973), contains lots of hints on the origins of the spectrum and could be a basis for its determination in future work.

1.3. Newer developments explored with a review paper

In order to get an idea about the developments up to the present day we take a look at Netzer (2018) primarily focusing on the difference between the subfields dubbed “right” (great progress, understanding of big picture present) and these which are dubbed “wrong” (still missing crucial details). Very short summaries are provided here, while more detailed information can be found partly in Netzer (2018) and mostly in its references which are partly referenced here.

1.3.1. “The Active Galactic Nucleus (AGN) Family: New Multi-wavelength observations” (Netzer 2018)

1.3.1.1. “Something Right: Systematic Study of LINERS [Low-ionisation nuclear emission line regions], Seyferts, High Luminosity AGN and Objects Containing Disk-Like Broad Line Emitting Region (BLR)s” (Netzer 2018)

Netzer (2018) described progress in this field is primarily driven by new surveys and instruments making much larger surveys of AGN available. The SDSS survey is mentioned amongst various smaller surveys such as COSMOS and BAT, which can give much insight on the topics above. Márquez et al. (2017) looked at LINERs and Seyfert 2s galaxies. Using a multi wavelength approach, it was confirmed that most LINER objects are AGN-powered in the local universe. Furthermore, using a study of spectral X-ray variability, long term oscillations were confirmed as very common and related primarily to hard X-rays at energies of 2 keV to 10 keV. Additionally, more evidence for LINERs residing at the low end of AGN luminosity was found via mid-infrared imaging. Richards (2017) offered a type-I AGN catalogue from SDSS cross-referenced with HST, combined with a new division mechanism which uses eigenvector groups. Lira et al. (2018) presented reverberation mapping employed on a sample of high luminosity quasi-stellar radio sources (QUASARs) at high z on a time period of over 10 years, observed photometrically and spectroscopically. Lusso and Risaliti (2018) is mentioned to “provide a fresh look at X-ray sources ” (Netzer 2018). They used SDSS data cross-matched to the XMM-Newton catalogue 3XMM-D36, to conclude a modified non-linear relation between the 2 keV and 250 μm ultraviolet emission in quasars following the equation

$$L_X \propto L_{UV}^\gamma, \quad (1.15)$$

where L_X is the emitted X-ray luminosity, L_{UV} is the emitted UV luminosity and γ is some exponent. Starting from this, Lusso and Risaliti (2018) arrived at a tighter correlation of $L_X - L_{UV}$ to the full width at half maximum of the MgII broad line and redshift evolution was observed. Netzer (2018) also mentioned two methods developed by Agnello (2017) in order to scan for selecting strongly lensed QUASARs in wide-field surveys. Having been successfully applied to e.g. SDSS, it is now suggested to use them on GAIA data to automatically identify e.g. galactic streams.

1.3.1.2. “Something wrong: A complete picture of Radio AGN” (Netzer 2018)

Mainly referring to the extensive review by Padovani (2017), Netzer (2018) concludes that there is yet no agreed-upon general understanding of all the radio sources related to AGN. Despite lots of data and more details, described as an “AGN zoo” (Padovani 2017), only incremental progress is reported in the last two decades.

1.3.2. “Mapping and Modelling the BLR and Measuring BH Masses” (Netzer 2018)

1.3.2.1. The subfields dubbed “right”

Netzer (2018) mentions the successful subfield of “Reverberation Mapping in One and Two Dimensions” (Netzer 2018), where location and kinematics were determined for e.g. NGC 5548 by HST (Hubble space telescope) and ground based telescopes. Netzer (2018) expects great advancement for the analysis of the BLR. Moreover, the results of Horne and Agn Storm Team (2015), Fausnaugh et al. (2017) offer new insights into time dependent broad and narrow emission lines which also result in more structural information on the Accretion Disk (AD). Secondly, regarding the subfield of “The R-L Relationship and Single-Epoch Mass Measurements” (Netzer 2018). It is described that several authors managed to provide a great collection of sources that determined the weighted radius of the broad $H\beta$ line by “correlated line and continuum variations” (Netzer 2018). Some more results have been found for the BLR motion and a coupling of size of the $H\beta$ emission region to the “Eddington ratio of the accreting BH” (Netzer 2018). A great new result, according to Netzer (2018), is that it was determined that the emitting regions for the $CIV\lambda 1549$ and $Ly\alpha$ line are a factor of 2-3 closer to the black hole than previously assumed. It is stressed that this question has been unanswered for 10-15 years, and that sometimes long-term observations are required to arrive at answers. Furthermore, VLT/GRAVITY will enable the community to directly determine the sizes of the BLR in type-I AGN and, recent more detailed type-1 studies begin to reveal fundamentally different physics from the current picture.

1.3.2.2. The subfields dubbed “wrong”

Almost no progress is reported for the subfield of “Phase-Space Modelling of the BLR” (Netzer 2018). Although there are the great 2D reverberation mapping maps, as reported earlier, the lack of good data for other sources prevents the community from developing consistent models connecting spatial positions and dynamics. The state of this research field is reported to be the same than as the first optical UV RM studies were made 20 years ago. On a positive note, Czerny et al. (2017) presented a better location pinpointing of the BLR clouds within the “dusty outer parts of the accretion disk” (Netzer 2018). It is indicated that these (and similar) models could be tested employing next generation 2D BLR models. Apart from these facts, Netzer (2018) mentions that ideas revolving around the dependency of radial position of the BLR might give insight into better mass estimates for the black holes. As a last point in this subsection, Netzer (2018), mentions new efforts to improve the estimates of the black hole masses. More specifically, Mejía-Restrepo et al. (2018) is cited for a new proposed method of using the broad emission lines under the assumption of virialised gas moving in “close vicinity to the active black holes” (Mejía-Restrepo et al. 2018). However, this method is plagued by uncertainties in the gas cloud distribution according to Mejía-Restrepo et al. (2018). It should be noted that this was only reported to be useful for AGN high in luminosity and redshift.

1.3.3. “Accretion Disks and Disk Winds” (Netzer 2018)

1.3.3.1. “Right”

Netzer (2018) positively addresses the subfield of “Thin Accretion Disk Models and the Optical-UV SED” (Netzer 2018) for managing to fit the optical-UV continuum to the “canonical spectrum of a thing accretion disk” (Netzer 2018) for AGN with an Eddington ratio not too large and a Super Massive Black Hole (SMBH) mass that is not too high ($1.0 \times 10^8 M_{\odot}$ to $1.0 \times 10^9 M_{\odot}$). While he acknowledges that all theoretical models and simplified numerical simulations predict the presense of disk winds especially close to the SMBH. More specifically, Elitzur and Netzer (2016) is mentioned for advocating dust-free winds as a necessary component of disks with a strong magnetic field. On the other hand, it is pointed out that there are not any observations giving undoubted proof for these winds. However, some results that are dropping strong hints are described. Some observations of “polar dust” found in interferometry data. Netzer (2018) proposes the result of looking at the lens magnification map of a system lensed by a foreground star, allowing to combine location and velocity of the BLR of the lensed object, as one of the most important new results. While this highlights the contribution of Hutsemékers et al. (2017), it is also admitted that this method can only be used for a very limited number of sources.

1.3.3.2. “Wrong”

While some “wrong” was already mentioned for the winds, Netzer (2018) points out that although huge theoretical and observational effort is put fourth, thin ADs exceeding an Eddington ratio of ≈ 0.3 are not understood as of now. The main reason is that there are discrepancies between observations and theory.

1.3.4. “Star Formation Galactic-Scale Winds Mergers and Feedback” (Netzer 2018)

1.3.4.1. “Something Right: Observational Evidence for Outflow and Mergers” (Netzer 2018)

This subfield is presented very positively. Enormous observational effort made it possible to release high quality velocity maps for a wide range of objects showing (for a range of redshifts) “outward motion of ionized and molecular gas” (Netzer 2018). The interpretation of this is an association with the vicinity of the SMBH creating X-ray outflows, the Narrow Line Emitting Region (NLR) or even regions further away in the host galaxy. Additionally, it is reported that new instruments like the JWST (and others) will contribute a lot to the further enrichment of this subfield.

1.3.4.2. “Something Wrong: Interpreting Outflow and Feedback” (Netzer 2018)

A quite bleak picture is painted here for the status of this subfield. Because accurate outflow measurements are not possible, the important influence these have to the quenching of star formation and the general structure of the host galaxy, summed up as AGN feedback, cannot be reliably estimated and compared to observations. While molecular outflows are somewhat understood, apart from the CO line production, ionised outflows have too many uncertainties to be useful for this subfield. Netzer (2018) furthermore presents current feedback models as still not adequate for any determination of influence on the galactic scale. The main problem is the inability to decide whether energy conserved or momentum conserved outflows have the bigger effect. On the one hand, the observations have improved a lot, but neither theory nor simulations could draw reliable conclusions up to now. As an upside, Lira et al. (2018) is cited as a reference for the better understood influence of larger structures such as powerful radio jets and X-ray cavities. Contradicting results are reported for the correlation of AGN luminosity and star formation rate in high and low redshift sources. Again, contradictions appear when looking at near companion galaxies as a trigger for star formation between the remarkable (but still contradicting) results of Fogasy, J. et al. (2017), Kimball et al. (2015), Trakhtenbrot et al. (2017).

1.3.5. Cosmology: “Something Wrong: All AGN-Based Methods” (Netzer 2018)

Netzer (2018) describes that no reliable tools yet exist to use AGN physics to help mapping the universe and its expansion. While many ideas have been put forth in some references within Netzer (2018) describing possible methods “systematic uncertainties in all the methods, combined with lack of understanding of some of the involved processes” (Netzer 2018) are preventing the AGN community from reducing uncertainties to a level that can be trusted.

1. Introduction and Motivation

Table 1

Regime	A	C	E					
Region	1	2	4					
Opacity	0.4	10^{-3}	$1 \text{ cm}^2 \text{ g}^{-1}$					
Multiplication factors								
T_c	2510	760	3020	$\alpha^{-1/5}$	$f_\epsilon^{-2/5}$	$f_L^{3/5}$	$L_{44}^{-1/5}$	$\rho^{-9/10}$
N_{25}	98	324	80	$\alpha^{-4/5}$	$f_\epsilon^{-3/5}$	$f_L^{2/5}$	$L_{44}^{1/5}$	$\rho^{-3/5}$
H_{15}	0.12	0.068	0.14	$\alpha^{-1/10}$	$f_\epsilon^{-1/5}$	$f_L^{-7/10}$	$L_{44}^{9/10}$	$\rho^{21/20}$
n_{c10}	630	3780	480	$\alpha^{-7/10}$	$f_\epsilon^{-2/5}$	$f_L^{11/10}$	$L_{44}^{-7/10}$	$\rho^{-33/20}$
τ	260	2.2	540	$\alpha^{-4/5}$	$f_\epsilon^{-3/5}$	$f_L^{2/5}$	$L_{44}^{1/5}$	$\rho^{-3/5}$
Regime	B							
Opacity	$3 \cdot 10^{-40} T^{10} \text{ cm}^2 \text{ g}^{-1}$							
T_c	26000	$\alpha^{1/5}$	$f_\epsilon^{2/5}$	$f_L^{-3/5}$	$L_{44}^{1/5}$	$\rho^{9/10}$		
N_{25}	9.2	$\alpha^{-6/5}$	$f_\epsilon^{-7/5}$	$f_L^{8/5}$	$L_{44}^{-1/5}$	$\rho^{-12/5}$		
H_{15}	0.4	$\alpha^{1/10}$	$f_\epsilon^{1/5}$	$f_L^{-13/10}$	$L_{44}^{11/10}$	$\rho^{39/20}$		
n_{c10}	18	$\alpha^{-13/10}$	$f_\epsilon^{-8/5}$	$f_L^{20/10}$	$L_{44}^{-13/10}$	$\rho^{29/20}$		
τ	$3.3 \cdot 10^6$	$\alpha^{4/5}$	$f_\epsilon^{13/5}$	$f_L^{-22/5}$	$L_{44}^{9/5}$	$\rho^{33/5}$		
Regime	D	Dbis	F					
Region	3							
Multiplication factors								
T_c	1400	2000	7000					
N_{25}	175	122	35	$\alpha^{-1} f_\epsilon^{-1} f_L$				$\rho^{-3/2}$
H_{15}	0.093	0.11	0.21			f_L^{-1}	L_{44}	$\rho^{3/2}$
n_{c10}	1500	800	135	$\alpha^{-1} f_\epsilon^{-1} f_L^2$			L_{44}^{-1}	ρ^{-3}
τ	^a	< 1	< 1					

^a The opacity cannot be determined as it varies too rapidly.

Figure 1.3.: Profile equations from model presented in Collin-Souffrin and Dumont (1990). τ is the mean vertical thickness, H_{15} is twice the scale height in $1 \times 10^{15} \text{ cm}$, n_{c10} is the central density in $1 \times 10^{10} \text{ cm}^{-3}$, N_{25} is the column density measured in $1 \times 10^{25} \text{ cm}^{-2}$, $L_{44} = 1 \times 10^{44} \text{ erg s}^{-1}$ is the Luminosity, f_ϵ is the efficiency of mass-energy conversion divided by 0.1 (canonical value), $f_L = \frac{L_{\text{bol}}}{L_{\text{edd}0.1}}$ is the ratio of the bolometric luminosity divided by the Eddington luminosity and 0.1 and $\rho = \frac{R}{10^4 R_S}$, Explanation of Regime and Regions see Tab. 1.2

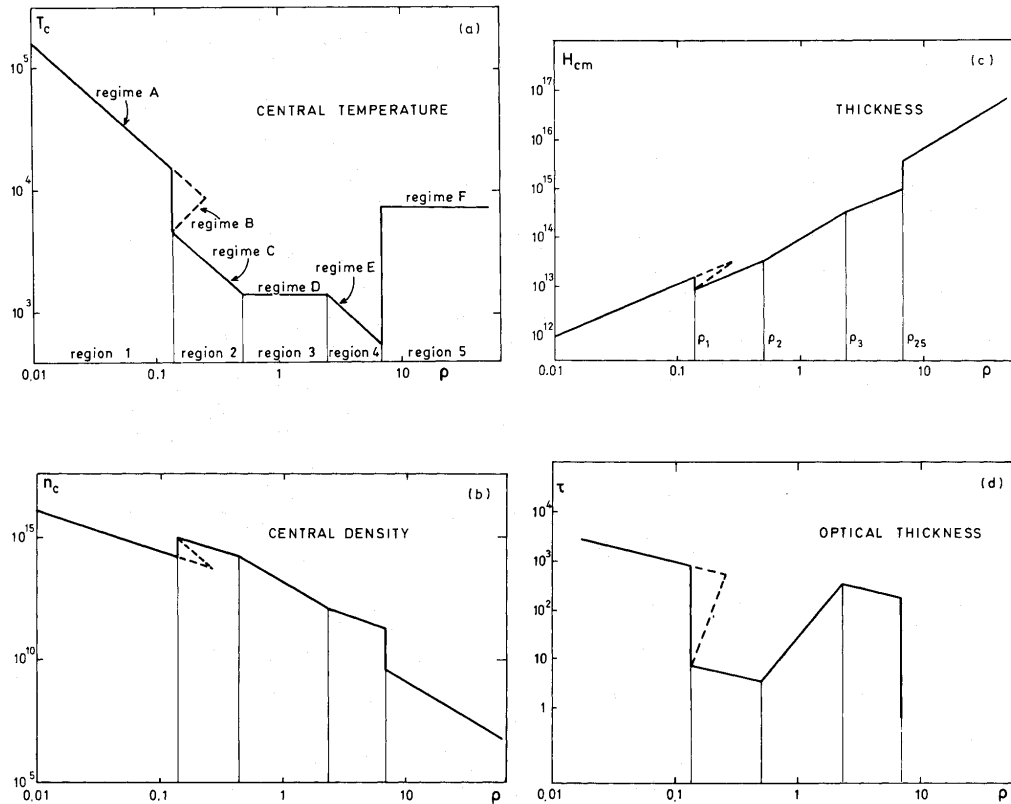


Fig. 1a-d. Central temperature, central density, thickness and optical thickness, as functions of the radius divided by $10^4 R_G$. The different (simplified) opacity regimes are indicated. Broken lines are for the non physical regimes

Figure 1.4.: Profiles from model presented in Collin-Souffrin and Dumont (1990)

2. Physics of Accretion Disks

2.1. Theoretical foundations of α -Disks

In Shakura and Sunyaev (1973) Shakura and Sunyayev present the basis for the α -Disk formalism. The goal of the paper is to explain the observational appearance of black holes in binary systems. The main characteristic of such systems, as for Active Galactic Nucleus (AGN) systems, is the presence of a black hole that is actively accreting matter. Here, the source of the material is the companion star. Shakura and Sunyaev (1973) mentions, that as the material originating from the companion star has high angular momentum relative to the black hole, a pure free-fall of (cold) matter into the black hole cannot happen. Thus, a mechanism for removing this angular momentum must to be at work in order for the black hole to accrete matter. An Accretion Disk (AD) supplies such a mechanism and is also able to partly explain the emission spectra. This includes soft X-rays, optical radiation as well as UV radiation. It is mentioned in Shakura and Sunyaev (1973), that it is possible for this radiation to outshine the companion star in observations. The central factor for the luminosity is identified to be the accretion rate \dot{M} , e.g. the amount of matter accreted per time unit. Following Shakura and Sunyaev (1973), three cases are observed:

- $\dot{M} \in [1.0 \times 10^{-9} M_{\odot} \text{ yrs}^{-1} - 3.0 \times 10^{-8} M_{\odot} \text{ yrs}^{-1}]$, (Subcritical case)
The AD around the BH is a powerful source of X-ray radiation with $1 \text{ keV} \lesssim h\nu \lesssim 10 \text{ keV}$ and $1.0 \times 10^{37} \frac{\text{erg}}{\text{s}} \lesssim L \lesssim 1.0 \times 10^{38} \frac{\text{erg}}{\text{s}}$. A dropping flux of accreting matter will result in a decrease of the effective temperature of the radiation and its luminosity.
- $\dot{M} > 1.0 \times 10^{-9} M_{\odot} \text{ yrs}^{-1}$
The luminosity of the disk will exceed solar values and will be dominated by re-radiation of X-rays and UV radiation from the central part of the AD. In certain circumstances gas can be evaporated and thus auto-regulate accretion.
- $\dot{M} \gg 1.0 \times 10^{-8} M_{\odot} \text{ yrs}^{-1}$
The luminosity has stabilised at $L \approx \frac{\dot{M}}{M_{\odot}} 1.0 \times 10^{38} \text{ erg yrs}^{-1}$. Only a small fraction of matter enters the Schwarzschild radius, the rest flows out of the central regions with high velocity. In this supercritical case the black hole may appear to be a hot, bright optical star with strong outflow.

2. Physics of Accretion Disks

In order to treat the gas of the AD we introduce

$$E_{\text{tot}} = E_{\text{gas}} + E_{\text{rad}} \quad (2.1)$$

$$p_{\text{tot}} = p_{\text{gas}} + p_{\text{rad}} \quad (2.2)$$

where E_{tot} is the total energy density, E_{gas} is the energy density of the gas, E_{rad} is the radiation energy density, p_{tot} is the total pressure, p_{gas} is the gas pressure and p_{rad} is the radiation pressure. These quantities are given by

$$c_{\text{S}}^2 = \frac{2E_{\text{tot}}}{\rho} \quad (2.3)$$

$$v_{1\text{D}}^2 = \frac{k_{\text{B}}}{\mu m_{\text{H}}} T \quad (2.4)$$

$$E_{\text{gas}} = \frac{3}{2} \rho v_{1\text{D}}^2 \quad (2.5)$$

$$p_{\text{gas}} = \frac{2}{3} E_{\text{gas}} = \rho v_{1\text{D}}^2, \quad (2.6)$$

where c_{S} is the sound speed, ρ is the gas volume density, $v_{1\text{D}}$ is 1D thermal sound speed of the gas, T is the gas temperature, m_{H} is the mass of an hydrogen atom, μ is the relative mass constant of the gas and k_{B} is Boltzmann's constant. The central point of the accretion theory is the effectiveness of the angular momentum transport mechanism. Integral to this are the turbulent motions of the matter as well as the magnetic field that is assumed to exist. Shakura and Sunyaev (1973) introduces the α parameter describing the efficiency of the angular-momentum transport mechanism defined as

$$\alpha = \frac{v_{\text{T}}}{c_{\text{S}}} + \frac{H^2}{4\pi\rho c_{\text{S}}^2}, \quad (2.7)$$

where

$$\frac{\rho c_{\text{S}}^2}{2} = \frac{3}{2} \rho \frac{k_{\text{B}}}{m_{\text{p}}} T + E_{\text{rad}} \quad (2.8)$$

is the total internal energy density of the matter, E_{rad} is the radiation energy density, v_{T} is the turbulent velocity, c_{S} is the sound speed of the gas, H is the magnetic field, ρ is the volume gas density, k_{B} is Boltzmann's constant, T is the gas temperature and m_{p} is the proton mass. As shown later in Shakura and Sunyaev (1973) $\alpha \leq 1$ is valid in the subcritical regime. The subcritical regime is, according to Shakura and Sunyaev (1973) if

$$\dot{M} \leq \dot{M}_{\text{crit}} = 3.0 \times 10^{-8} \frac{0.06 M_{\text{BH}}}{\eta \text{ yrs}}, \quad (2.9)$$

where \dot{M}_{crit} is the critical accretion rate, M_{BH} is the black hole mass and η is the efficiency at which gravitational energy is released. Moreover, it is assumed that α is constant over the entire disk. Presuming the accretion disk scenario, the paper proposes a concrete picture for the angular momentum loss mechanism. Particles

in different layers of the disk lose angular momentum by friction between adjacent layers, thus spiraling into the black hole and converting gravitational to rotational energy as well as dissipated into thermal energy and radiation. The paper primarily treats the subcritical regime of the disk as characterised by equation (2.9). Also, Newtonian physics is used, since general relativistic effects are only needed below $10R_{\text{SW}}$ (where $R_{\text{SW}} = 2GM/c^2$ is the Schwarzschild radius of the black hole). This region's contribution to the radiation output can be, however, ignored for the system considered. Assuming the energy $0.06c^2$ is released per unit mass of infalling matter and $L = 0.06c^2\dot{M}$ as the luminosity of the AD the angular momentum model is constructed. The idea is angular momentum transport by differentially rotating tangential stresses between adjacent layers in a medium connected by a magnetic field, turbulence and radiative viscosity. It is shown that the magnetic field energy cannot exceed the thermal energy of the gas because of the differentially rotating nature leading to chaotic and small scale magnetic field loops. Despite no consistent theory of turbulence in the disk being available, the paper presents a model using results from laminar flows of incompressible fluids. The turbulence is consequently perturbed at high Reynolds numbers. Taking into account turbulence from release of gravitational energy as well as the radiative flux to surface layers, one can conclude that the turbulence cell can only be of the order of the disk half-thickness z_0 . Thus one can conclude that the stress-tensor element (see Subsection 2.2.2 for details) is given by

$$-\sigma_{R\varphi} = \alpha\rho c_s^2, \quad (2.10)$$

where R is the cylindrical radius and φ is the cylindrical coordinate angle. It should be noted that while magnetic fields are almost certainly present, the turbulence is not so clearly proven to exist, according to this paper. One can conclude that $\alpha < 1$, because $\alpha > 1$ would mean supersonic turbulence that would induce extreme heating and thus to $\alpha \leq 1$. Also, $\alpha < 1$ is likely as magnetic angular momentum transport is possible in this case. $\alpha \ll 1$ may also occur for wide range of initial conditions. Actually, α should at least depend on the cylindrical radius. However, considering experiments involving turbulence Shakura and Sunyaev (1973) infer that

$$1.0 \times 10^{-15} \left(\frac{\dot{M}}{\dot{M}_{\text{cr}}} \right) < \alpha < 1. \quad (2.11)$$

The α -formalism thus allows us to make predictions about external properties of the AD without knowing the details about the mechanism driving the angular momentum transport. It is furthermore derived that the disk's luminosity is, for essentially subcritical fluxes of $\dot{M} = 1.0 \times 10^{-12} M_{\odot} \text{ yrs}^{-1}$ to $1.0 \times 10^{-10} M_{\odot} \text{ yrs}^{-1}$, given by $L = 1.0 \times 10^{34} \text{ erg s}^{-1}$ to $1.0 \times 10^{36} \text{ erg s}^{-1}$. In this context the paper also states $T_{\text{S}} = 3.0 \times 10^5 \text{ K}$ to $1.0 \times 10^6 \text{ K}$ as the maximum surface temperature for the inner regions of the disk. These also release the bulk of the energy (mainly radiated in the UV and X-ray bands). This energy is re-radiated energy emitted by the central engine. The paper mentions a layered approach to this problem which allows an estimation of

2. Physics of Accretion Disks

the emitted spectrum. Further details are omitted here as no radiation spectrum was determined in the course of this thesis.

2.1.1. Disk structure

On top of its more broad elaborations, concrete structures and profiles for the AD are calculated in Shakura and Sunyaev (1973). To first order, the rotation of the gas can be assumed to be Keplerian i.e.

$$v_{K,0} = \sqrt{\frac{GM}{R}}, \quad \omega = \sqrt{\frac{GM}{R^3}} = \frac{v_K}{R}. \quad (2.12)$$

Here, $v_{K,0}$ is the Keplerian velocity only depending on R ($z = 0$), R is the cylindrical radius, ω is the angular velocity and G is the gravitational constant. Equation (2.2) in Shakura and Sunyaev (1973) is in our notation

$$u_0 \frac{\omega R^2}{t} = -u_0 v_R \frac{\omega R^2}{R} - \frac{1}{R} \Sigma_{R\varphi} R^2, \quad (2.13)$$

where u_0 is the surface density, v_R is the velocity in the R direction and $\Sigma_{R\varphi}$ the stress between adjacent layers i.e. $\int_0^h \sigma_{R\varphi}$. When assuming stationary conditions we can conclude that $v_R = 0$ and $\dot{M} = 2\pi u_0 v_R R = \text{const}$ (stress between adjacent layers). For a non-rotating black hole, pure Newtonian physics we get arrive at

$$\dot{M}\omega = 2\pi\alpha u_0 c_s^2, \quad (2.14)$$

when using equation (1.2) in Shakura and Sunyaev (1973). This is equation (2.4) in Shakura and Sunyaev (1973) when assuming that $R \gg R_S$. It assumed that the radial velocity is $v_R \ll v_K$ in the disk. In stationary conditions $\dot{M} = \text{const}$. Assuming vertical hydrostatic equilibrium and a vertically constant sound speed c_s gives the half-thickness (i.e. the vertical height at which the density of the equatorial plane has dropped to e^{-1}) of the disk z_0 as

$$z_0 = \frac{c_s}{v_\varphi} R. \quad (2.15)$$

In the following $z_0 = h$ will be used as the general notation throughout the rest of this thesis. For determining some of the radiative properties of the disk it is required to think about opacity and radiation pressure. The two relevant opacity processes are the Thompson scattering (gouverned by the σ_T cross section) on free electrons and the free-free absorption of electrons (gouverned by the σ_{ff} cross section. In the optically thick regions inside the disk $E_{\text{rad}} = a_{\text{rad}} T^4$, where T is the temperature and a_{rad} is the radiation constant. Also, $c_s^2 = E_{\text{rad}}/(3\rho)$ is valid in radiation pressure dominated regions, whereas $c_s = \frac{k_B T}{\mu m_p}$ is valid in gas-pressure dominated regions. All of this gives rise to the three regimes distinguished in Shakura and Sunyaev (1973) dubbed

- a) $p_{\text{rad}} > p_{\text{gas}}$, matter-radiation interaction is dominated by Thompson scattering

on free electrons ($\sigma_T > \sigma_{\text{ff}}$)

- b) $p_{\text{rad}} < p_{\text{gas}}$, matter-radiation interaction is still dominated by Thompson scattering on free electrons ($\sigma_T > \sigma_{\text{ff}}$)
- c) $p_{\text{rad}} < p_{\text{gas}}$, matter-radiation interaction is dominated by free-free absorption ($\sigma_T < \sigma_{\text{ff}}$)

a) describes the innermost regions of the disk which neighbours region b) separated by R_{ab} which can be determined from

$$\frac{R_{\text{ab}}}{3R_{\text{SW}}} \left(1 - \left(\frac{R_{\text{ab}}}{3R_{\text{SW}}} \right)^{-\frac{1}{2}} \right)^{-\frac{16}{21}} = 150 \left(\alpha \frac{M_{\text{BH}}}{M_{\odot}} \right)^{\frac{2}{21}} \left(\frac{\dot{M}}{\dot{M}_{\text{crit}}} \right)^{\frac{16}{21}}, \quad (2.16)$$

where $\dot{M}_{\text{crit}} = 3 \times 10^{-8} \frac{M}{\text{yrs}}$ (equation (2.17) in Shakura and Sunyaev (1973)). As

$$\frac{R_{\text{ab}}}{3R_{\text{SW}}} \left(1 - \left(\frac{R_{\text{ab}}}{3R_{\text{SW}}} \right)^{-\frac{1}{2}} \right)^{-\frac{16}{21}} \geq 1 \quad (2.17)$$

one can conclude that region a) only exists if

$$\frac{\dot{M}}{\dot{M}_{\text{crit}}} \geq \frac{1}{170} \left(\frac{\alpha M}{M_{\odot}} \right)^{-\frac{1}{8}} \quad (2.18)$$

Following suit is the region c) whose border to region b) is defined by the equation (equation (2.20) in Shakura and Sunyaev (1973))

$$R_{\text{bc}} = 6.3 \times 10^3 \left(\frac{\dot{M}}{\dot{M}_{\text{crit}}} \right)^{\frac{2}{3}} \left(1 - \left(\frac{R_{\text{bc}}}{3R_{\text{SW}}} \right)^{-\frac{1}{2}} \right)^{\frac{2}{3}}. \quad (2.19)$$

2.1.2. Profiles derived in Shakura and Sunyaev (1973)

Shakura and Sunyaev (1973) uses its considerations to derive, amongst other things, expressions for the surface density u_0 , half-thickness z_0 (dubbed scale height h throughout most of this thesis) and the radial velocity v_R . All formulas assume $v_r \ll v_{\varphi}$ which requires

$$\frac{R}{3R_{\text{SW}}} - 1 > 1.0 \times 10^{-6} \alpha^{\frac{8}{7}} \left(\frac{\dot{M}}{\dot{M}_{\text{crit}}} \right)^{\frac{3}{7}} \quad (2.20)$$

along with $R > 49/36R_{\text{SW}}$. In all of the cases considered in this thesis R will always be at least one (most of the time two or three) orders of magnitude higher than the

2. Physics of Accretion Disks

Schwarzschild radius, thus justifying $3R_{\text{SW}}/R \approx 0$, which also implies

$$\left(1 - \left(\frac{3R_{\text{SW}}}{R}\right)^{-\frac{1}{2}}\right) \approx 1. \quad (2.21)$$

For a) this results in (equation (2.16) in Shakura and Sunyaev (1973))

$$u_0 = \frac{64\pi}{9\alpha} \frac{c^2}{\sigma_{\text{T}}} \sqrt{\frac{R^3}{GM_{\text{BH}}} \frac{1}{\dot{M}}} \quad (2.22)$$

$$v_R = \frac{\dot{M}^2}{128\pi^2} \frac{\sigma_{\text{T}}}{c^2} 9\alpha \sqrt{GM_{\text{BH}}} R^{-\frac{5}{2}} \quad (2.23)$$

$$h = \frac{3}{8\pi} \frac{\sigma_{\text{T}}}{c} \dot{M}, \quad (2.24)$$

where σ_{T} is the cross-section and $u_0 = \int_{-\infty}^{\infty} \rho dz$ is the surface density. Advancing to b) one obtains (equations (2.19) and (2.11) in Shakura and Sunyaev (1973))

$$u_0 = \left(\frac{1}{2\pi} \frac{m_{\text{p}}}{\alpha k_{\text{B}}}\right)^{\frac{4}{5}} \left(\frac{9}{32\pi} \frac{\sigma_{\text{T}}}{c}\right)^{-\frac{1}{5}} a_{\text{rad}}^{\frac{1}{5}} \dot{M}^{\frac{3}{5}} G^{\frac{1}{5}} M^{\frac{1}{5}} R^{-\frac{3}{5}} \quad (2.25)$$

$$v_R = \left(\frac{1}{2\pi} \frac{m_{\text{p}}}{\alpha k_{\text{B}}}\right)^{-\frac{4}{5}} \left(\frac{9}{32\pi} \frac{\sigma_{\text{T}}}{c}\right)^{\frac{1}{5}} a_{\text{rad}}^{-\frac{1}{5}} \dot{M}^{\frac{2}{5}} G^{-\frac{1}{5}} M^{-\frac{1}{5}} R^{-\frac{2}{5}} \quad (2.26)$$

$$h = \left(\frac{1}{2\pi\alpha}\right) \left(\frac{m_{\text{p}}}{k_{\text{B}}}\right)^{-\frac{2}{5}} \left(\frac{9}{32\pi} \frac{\sigma_{\text{T}}}{c}\right)^{\frac{1}{10}} a_{\text{rad}}^{-\frac{1}{10}} \dot{M}^{\frac{1}{5}} G^{-\frac{7}{20}} M^{-\frac{7}{20}} R^{\frac{21}{20}} \quad (2.27)$$

whereas in c) the profiles determined are (equation (2.19) in Shakura and Sunyaev (1973))

$$u_0 = \frac{1}{2\pi} \left(\frac{99}{25600\pi^3} \frac{\text{cm}^5}{\text{g}}\right)^{-\frac{1}{10}} \alpha^{-\frac{4}{5}} \left(a_{\text{rad}} c m_{\text{p}} K^{-\frac{7}{2}}\right)^{\frac{1}{10}} \left(\frac{m_{\text{p}}}{k_{\text{B}}}\right)^{\frac{3}{4}} \dot{M}^{\frac{7}{10}} G^{\frac{1}{4}} M^{\frac{1}{4}} R^{-\frac{3}{4}} \quad (2.28)$$

$$v_R = \left(\frac{99}{25500\pi^3} \frac{\text{cm}^4}{\text{g}}\right)^{\frac{1}{10}} \alpha^{\frac{4}{5}} \left(a_{\text{rad}} c m_{\text{p}} K^5\right)^{\frac{1}{10}} \left(\frac{m_{\text{p}}}{k_{\text{B}}}\right)^{\frac{1}{10}} \dot{M}^{\frac{3}{10}} G^{-\frac{1}{4}} M^{-\frac{1}{4}} R^{-\frac{1}{4}} \quad (2.29)$$

$$h = \left(\frac{99}{25600\pi^3} \frac{\text{cm}^4}{\text{g}}\right)^{\frac{1}{20}} \alpha^{-\frac{1}{10}} \left(a_{\text{rad}} c m_{\text{p}} K^{-\frac{7}{2}}\right)^{-\frac{1}{20}} \left(\frac{m_{\text{p}}}{k_{\text{B}}}\right)^{-\frac{3}{8}} \dot{M}^{\frac{3}{20}} G^{-\frac{3}{8}} M^{-\frac{3}{8}} R^{\frac{9}{8}} \quad (2.30)$$

2.1.3. More rigorous proof in other papers

Balbus and Papaloizou (1999) describes the dynamical foundations for α disks. It investigates to what extent the α formalism is applicable considering theoretical models available at the time the paper was written. Detailedly, Balbus and Papaloizou (1999) relates Magneto Hydrodynamics (MHD) turbulence to the α disk prescription resulting in an equation describing the energy dissipation rate. Local MHD disturb-

ances force local magnetic field dissipation into a turbulent flow. Concretely, Balbus and Papaloizou (1999) gives the analogy to vorticity dynamics in an unmagnetised shear layer. The paper states, however, that this is not the case for self-gravitating disks even if they are turbulent. Flow dynamics in these disks is much more complicated and specifically cannot be described using a “simple restrictive form” for both the mean momentum and energy fluxes which especially cannot depend on any other transport properties apart from the viscous stress tensor element $\sigma_{R\phi}$ and the density averaged radial speed $\langle v_R \rangle_\rho$. There are anomalous flux terms allowing self-gravitating disturbances propagating non-locally in the disk via the perturbed gravitational potential. While the angular momentum is strictly conserved in such a disk and has the same canonical form as a non-self-gravitating disk ($\propto \sigma_{R\phi}$), the energy flux is fundamentally different. Summed up, non-local transport cannot be captured by α disks. Under special circumstances, however, one can re-establish local α behaviour. Thus, Balbus and Papaloizou (1999) confirms that α -Disks are a reasonable descriptions for non-self-gravitating, MHD turbulence driven disks.

2.2. Fluid dynamics description

2.2.1. Time evolution equations

The Navier-Stokes equations are assumed to describe the gaseous disk in this thesis. This is based on three assumptions, following Shakura and Sunyaev (1973) and other presented cited papers:

- The requirements for a fluid dynamical description are satisfied.
- The distance from the central black hole is large enough to be able to use Newtonian physics.
- The formalism of α -Disks (e.g. Shakura and Sunyaev (1973) and Section 2.1) is valid; magnetic fields can thus be incorporated in the viscosity formalism, but neglected outside of it; This is valid as $B^2 \ll E_{\text{tot}}$ at our radial range

We are dealing with a non-relativistic, viscous fluid being subjected to gravity along with self-gravity. We assume the fluid to be a monoatomic ideal gas with added viscosity. Viscosity is assumed to be given by the α viscosity which is reformulated to fit the shear and bulk viscosity formalism. The formalism tells us that bulk viscosity is unimportant and can thus be set to zero and only shear viscosity can be considered (for details see Subsection 2.2.2 and Subsubsection 2.2.2.1 and Subsubsection 2.3.9). We thus consider a variant of the Navier-Stokes equations. This exact form is the one given in Toro (2009) in the chapter “Equations of Fluid dynamics”. Equation (1),(1)-(1.5) shows the Euler equations, equations (1.86)-(1.88) showcase the Navier-Stokes including the central gravity term. Note that heat conduction is excluded here i.e. $Q = 0$ and that the additional source-term for the self-gravity as a potential was added. The detailed form for this can be found in the PLUTO userguide (Code used later for simulations) which can be obtained at <http://plutocode.ph.unito.it>. These have the form

$$\frac{\partial \rho}{\partial t} + \nabla \cdot (\rho \mathbf{v}) = 0 \quad (2.31)$$

$$\frac{\partial \mathbf{m}}{\partial t} + \nabla (\mathbf{m} \cdot \mathbf{v}) + \nabla p = \rho \mathbf{g} - \rho \nabla \Phi_{\text{Gas}} + \nabla \sigma \quad (2.32)$$

$$\frac{\partial E}{\partial t} + \nabla (E \mathbf{v}) + \nabla (p \mathbf{v}) + \rho \Phi_{\text{Gas}} \mathbf{v} = \mathbf{m} \cdot \mathbf{g} + \nabla \cdot (\sigma \cdot \mathbf{v}). \quad (2.33)$$

In these equations ρ is the density, \mathbf{v} is the velocity vector, E is the total energy density, p is the pressure, \mathbf{g} is the acceleration vector of the central Super Massive Black Hole (SMBH) gravity, Φ_{Gas} is the potential of the self-gravity, c_s is the soundspeed, σ is the viscous stress tensor and $\mathbf{m} = \rho \mathbf{v}$ is the momentum density.

2.2.2. Viscosity

The viscosity components of this tensor σ are to be determined and the parameters set such that they correspond to the α formalism described in Shakura and Sunyaev (1973). In order to distinguish abstract differential geometric component notation and absolute physical components we denote the abstract components with braces as (i) (inspired by Mihalas and Weibel-Mihalas (1999)).

In Mihalas and Weibel-Mihalas (1999) we find the form

$$(\sigma)_{(ij)} = \mu \left(v_{(i);(j)} + v_{(j);(i)} - \frac{2}{3} \nabla v_{(k);(k)} \delta_{(ij)} \right) + \xi v_{(k);(k)} \delta_{(ij)}, \quad (2.34)$$

where $v_{(i);(j)}$ is the covariant derivative, μ is the ordinary coefficient of viscosity, ξ is the coefficient of bulk viscosity, \mathbf{v} is the velocity,

$$v_{(i);(j)} = \frac{\partial v_{(i)}}{\partial x_{(j)}}. \quad (2.35)$$

$$v_{(i);(i)} = \frac{\partial v_{(i)}}{\partial x_{(i)}} \quad (2.36)$$

and $\delta_{(ij)}$ is the Kronecker delta. Beginning from this, we can derive the tensor in cylindrical polars by using the Christoffel symbol formalism. It should be noted that the relations $g_{(ij)} v^i = v_{(j)}$ and $g^{(ij)} v_{(i)} = v^{(j)}$ are valid for the metric tensor $g_{(ij)}$ and that the covariant derivative can be expressed as $v^{(i)}_{;(j)} = v^{(i)}_{,(j)} + \Gamma^{(i)}_{(mj)} v^{(m)}$ and $v_{(i);(j)} = v_{(i),(j)} - \Gamma^{(m)}_{(ij)} v_{(m)}$ for the contravariant and covariant vector, respectively. More detailed information on this formalism can e.g. be found in Schutz (2009). Starting from equation (2.34) we obtain

$$\sigma_{(ij)} = \mu \left(v_{(i);(j)} + v_{(j);(i)} \right) + \left(\xi - \frac{2}{3} \mu \right) \delta_{(ij)} v^{(k)}_{;(k)} \quad (2.37)$$

$$\begin{aligned} &= \mu \left(v_{(i),j} - \Gamma^{(m)}_{(ij)} v_{(m)} + v_{(j),i} - \Gamma^{(m)}_{(ji)} v_{(m)} \right) \\ &\quad + \left(\xi - \frac{2}{3} \mu \right) \delta_{(ij)} \left(v^{(k)}_{,k} + \Gamma^{(k)}_{(mk)} v^{(m)} \right) \end{aligned} \quad (2.38)$$

Use that $\Gamma^{(m)}_{(ij)} = \Gamma^{(m)}_{(ji)}$ to conclude

$$= \mu \left(v_{(i),j} + v_{(j),i} - 2\Gamma^{(m)}_{(ji)} v_{(m)} \right) + \left(\xi - \frac{2}{3} \mu \right) \delta_{(ij)} \left(v^{(k)}_{,k} + \Gamma^{(k)}_{(mk)} v^{(m)} \right) \quad (2.39)$$

2. Physics of Accretion Disks

Now, we use special properties of the cylindrical polar coordinates. The covariant metric tensor for cylindrical polars is

$$\{g_{(ij)}\} = \begin{pmatrix} 1 & 0 & 0 \\ 0 & R^2 & 0 \\ 0 & 0 & 1 \end{pmatrix}, \quad (2.40)$$

whereas the contravariant form is

$$\{g^{(ij)}\} = \begin{pmatrix} 1 & 0 & 0 \\ 0 & \frac{1}{R^2} & 0 \\ 0 & 0 & 1 \end{pmatrix}. \quad (2.41)$$

The metric tensor is obviously diagonal, i.e.

$$g^{(ij)} = \begin{cases} \neq 0 & \text{if } i = j \\ 0 & \text{else.} \end{cases} \quad (2.42)$$

Thus, we can conclude, that

$$g_{(mi)}v^{(m)} = g_{(ii)}v^{(i)} \quad (2.43)$$

which is also true for the derivatives of metric or vector in this term. These properties simplify the tensor to take the form

$$\sigma_{(ij)} = \mu \left(v_{(i),j} + v_{(j),i} - 2\Gamma^{(m)}_{(ji)}v_{(m)} \right) + \left(\xi - \frac{2}{3}\mu \right) g_{(ij)} \left(v^{(k)},_k + \Gamma^{(k)}_{(mk)}v^{(m)} \right). \quad (2.44)$$

Because of the metric terms we know that

$$g^{(ii),j} = \begin{cases} 2R & \text{for } i = R \text{ and } j = \varphi \\ 0 & \text{else} \end{cases} \quad (2.45)$$

From the Christoffel symbols we can clearly see that

$$\Gamma^{(k)}_{(mk)}v^{(m)} = \Gamma^{(\varphi)}_{(R\varphi)}v^{(R)} = \frac{1}{R}v^{(R)} \quad (2.46)$$

as all other possible components vanish. This implies another simplification

$$\sigma_{(ij)} = \mu \left(v_{(i),j} + v_{(j),i} - 2\Gamma^{(m)}_{(ji)}v_{(m)} \right) + \left(\xi - \frac{2}{3} \right) g_{(ij)} \left(v^{(k)},_k + \frac{1}{R}v^{(R)} \right). \quad (2.47)$$

For the other combinations of indices one gets

$$\Gamma^{(m)}_{(ij)v(m)} = \begin{cases} \Gamma^{(R)}_{(\varphi\varphi)v(R)} = & \text{for } i = j = \varphi \\ \Gamma^{(\varphi)}_{(R\varphi)v(\varphi)} = \frac{v(\varphi)}{R} & \text{for } (i, j) \in \{(R\varphi), (\varphi R)\} \\ 0 & \text{else} \end{cases} \quad (2.48)$$

$$= \begin{cases} -Rv(R) & \text{for } i = j = \varphi \\ \frac{v(\varphi)}{R} & \text{for } (i, j) \in \{(R\varphi), (\varphi R)\} \\ 0 & \text{else} \end{cases}. \quad (2.49)$$

For $j = i$ we can infer that $g_{(ii),j} = 0$ as no suitable combination of indices exist which contributes. For convenience we define the notation

$$w := \left(\xi - \frac{2}{3}\mu \right). \quad (2.50)$$

Summed up we arrive at:

$$\sigma_{(ij)} = \begin{pmatrix} 2\mu v_{(R),R} + w \left(v^{(k)},_k + \frac{v^{(R)}}{R} \right) & \mu \left(v_{(R),\varphi} + v_{(\varphi),R} - 2\frac{v(\varphi)}{R} \right) \\ \mu \left(v_{(R),\varphi} + v_{(\varphi),R} - 2\frac{v(\varphi)}{R} \right) & 2\mu \left(2v_{\varphi,(\varphi)} + Rv_{(R)} \right) + w \left(v^{(k)},_k + \frac{v^{(R)}}{R} \right) \\ \mu \left(v_{(R),z} + v_{(z),R} \right) & \mu \left(v_{(\varphi),z} + v_{(z),\varphi} \right) \\ \mu \left(v^{(R)},_z + v^{(z)},_R \right) & \\ \mu \left(v_{(\varphi),z} + v_{(z),\varphi} \right) & \\ 2\mu v_{(z),z} + w \left(v^{(k)},_k + \frac{v^{(R)}}{R} \right) & \end{pmatrix}. \quad (2.51)$$

2.2.2.1. Viscosity in α disks

As mentioned by e.g. Shakura and Sunyaev (1973) of the tensor σ , as derived in equation (2.51), merely the $R\varphi$ component matters. This can also be seen in our result when assuming

$$v_R = 0 \quad v_z = 0 \quad \frac{\partial v_\varphi}{\partial \varphi} = \frac{\partial v_\varphi}{\partial z} = 0. \quad (2.52)$$

As we will see later our initial conditions will fulfil these assumptions exactly. This is the case when assuming a circular shearing flow as mentioned in Lodato (2008). As stated in Mihalas and Weibel-Mihalas (1999), Toro (2009) as well as the PLUTO (code later used for simulation) userguide the bulk viscosity always vanishes for an ideal, monoatomic gases as used here. More details can be found in “§32” in Mihalas

2. Physics of Accretion Disks

and Weibel-Mihalas (1999). Thus, the only relevant term is

$$\sigma_{(R\varphi)} = \mu \left(\frac{\partial v_{(R)}}{\partial \varphi} + \frac{\partial v_{(\varphi)}}{\partial R} - 2 \frac{v_{(\varphi)}}{R} \right). \quad (2.53)$$

Following Mihalas and Weibel-Mihalas (1999), we describe how we transform this tensor element to represent physical components instead of abstract coordinates. Initially, following equation (A.340) in Mihalas and Weibel-Mihalas (1999), we remind ourselves that the line element ds^2 in a three-dimensional coordinate system with a diagonal metric tensor can be written as

$$ds^2 = (h_{(1)}dx^{(1)})^2 + (h_{(2)}dx^{(2)})^2 + (h_{(3)}dx^{(3)})^2, \quad (2.54)$$

where $h_{(i)} = (g_{(i)(i)})^{\frac{1}{2}}$ and (i) describes the i -th component of the metric' coordinate variables. If looking at the increment path length, Mihalas and Weibel-Mihalas (1999) mentions that the ‘‘increment of path length associated with a coordinate increment dx^i is not dx^i itself, but $ds^{(i)} = h_{(i)}dx^{(i)}$.’’ (Mihalas and Weibel-Mihalas 1999). We now look at equation (2.55), dubbed equation (A.337) in Mihalas and Weibel-Mihalas (1999),

$$|\mathbf{a}| = (a_{(i)}a^{(i)})^{\frac{1}{2}} = (g_{(ij)}a^{(i)}a^{(j)})^{\frac{1}{2}}, \quad (2.55)$$

where $|\mathbf{a}| = a$ is the absolute physical length of vector \mathbf{a} . Following this one can infer that the vector length is equal to

$$a^2 = (h_{(1)}a^{(1)})^2 + (h_{(2)}a^{(2)})^2 + (h_{(3)}a^{(3)})^2. \quad (2.56)$$

As indicated in equation (A3.41) in Mihalas and Weibel-Mihalas (1999) demanding consistency with the Pythagorean theorem leads to the connection

$$a_i = h_{(i)}a^{(i)} \quad (2.57)$$

for the contravariant vector components and

$$a_i = \frac{a^{(i)}}{h_{(i)}} \quad (2.58)$$

for the covariant vector components. Furthermore, more elaborations in Mihalas and Weibel-Mihalas (1999) lead to their equation (A3.45)

$$T_{ij} = \frac{T_{(ij)}}{h_i h_j}, \quad (2.59)$$

where T_{ij} is a rank 2 tensor. For cylindrical coordinates we can easily calculate

$$h_{(R)} = 1, \quad h_{(\varphi)} = R \quad \text{and} \quad h_{(z)} = 1 \quad (2.60)$$

and thus

$$a_R = a^{(R)} = a_{(R)} \quad , \quad a_\varphi = \frac{a^{(\varphi)}}{R} = Ra_{(\varphi)} \quad \text{and} \quad a_z = a^{(z)} = a_{(z)}. \quad (2.61)$$

Using those, we convert the vector components in equation (2.53) resulting in

$$\sigma_{(R\varphi)} = \mu \left(\frac{\partial v_R}{\partial \varphi} + \frac{\partial Rv_\varphi}{\partial R} - 2Rv_\varphi \right) \quad (2.62)$$

$$= \mu \left(\frac{\partial v_R}{\partial \varphi} + v_\varphi + R \frac{\partial v_\varphi}{\partial R} - 2v_\varphi \right) \quad (2.63)$$

$$= \mu \left(\frac{\partial v_R}{\partial \varphi} + R \frac{\partial v_\varphi}{\partial R} - v_\varphi \right). \quad (2.64)$$

Now, equation (2.59) is used in order to determine the physical components of the viscosity tensor as

$$\sigma_{R\varphi} = \mu \left(\frac{1}{R} \frac{\partial v_R}{\partial \varphi} + \frac{\partial v_\varphi}{\partial R} - \frac{v_\varphi}{R} \right). \quad (2.65)$$

2.2.3. Radiation hydrodynamics

In order to compare results to observations as well as to fully include the radiation, a model of radiation transport is required. This is especially the case for Active Galactic Nucleus (AGN) systems as they are primarily observed using electromagnetic radiation and they reach high temperatures. Thus, we need to specifically model emission, absorption, heating, cooling, re-emission and re-absorption along with the radiative pressure carried by the photons. However, in this thesis we do mostly not take radiation into account and focus on the dynamics. But for future work and because the radiation transport module developed by Rolf Kuiper (see e.g. Kuiper et al. (2018, submitted)) is later used for simulations we include a description of the formalism used for that for completeness. The ‘‘Makemake’’ module (Subsection 3.2.6.1) employed later uses the Flux Limited Diffusion (FLD) approximation as outlined in Kuiper et al. (2018, submitted). This subsection mainly follows Kuiper et al. (2018, submitted). We give a short summary of the method here, while more detailed information can be found in Kuiper et al. (2018, submitted). Assuming the radiative transfer equation (equation (1) in Kuiper et al. (2018, submitted), consistent with Castor (2004))

$$\left(\frac{1}{c} \partial_t + \boldsymbol{\Omega} \cdot \nabla + \chi_{\text{ext}} \right) I_{\text{rad}} = \frac{c}{4\pi} (\chi_{\text{abs}} B_{\text{rad}} + \chi_{\text{scat}} E_{\text{rad}}), \quad (2.66)$$

where c is the speed of light, $\boldsymbol{\Omega}$ is the direction of the radiative flux, I_{rad} is the radiation intensity, χ_{ext} is the intensity extinction due to absorption and scattering, E_{rad} is the radiation energy density, B_{rad} is the integral of the black-body Planck spectrum, χ_{abs} is the extinction due to absorption, $\chi_{\text{abs}} B_{\text{rad}}$ is the emission source term, χ_{scat} is the extinction due to scattering, and $\chi_{\text{scat}} E_{\text{rad}}$ is the scattering source term. Moreover,

2. Physics of Accretion Disks

$\chi_{\text{ext}} = \chi_{\text{abs}} + \chi_{\text{scat}}$. The possible irradiation is skipped here as this will not be part of our model in the foreseeable future. It could only be used for a more advanced model that includes the hard radiation from the central engine of the AGN. Kuiper et al. (2018, submitted) first performs an integration over all solid angles on equation (2.66) and moreover employs the definitions

$$E_{\text{rad}} = \int_{4\pi} I_{\text{rad}} d\Omega \quad (2.67)$$

$$\mathbf{F}_{\text{rad}} = \int_{4\pi} I_{\text{rad}} \mathbf{\Omega} d\Omega, \quad (2.68)$$

where F_{rad} is the radiation energy flux density \mathbf{F}_{rad} and Ω is the solid angle. The result of that is

$$\frac{\partial E_{\text{rad}}}{\partial t} + \nabla \cdot \mathbf{F}_{\text{rad}} = c\chi_{\text{abs}} (B_{\text{rad}} - E_{\text{rad}}). \quad (2.69)$$

It should be noted that everything is presented in Grey approximation (frequency independent). It is possible to have frequency-dependent FLD, but this is not used or discussed in this work. The interested reader can refer to the references in Kuiper et al. (2018, submitted). Using the radiation pressure tensor \mathbf{P}_{rad} and the radiation diffusion tensor \mathbf{D}_{rad} one can write equation (2.69) as

$$\mathbf{F}_{\text{rad}} = -\nabla \cdot \mathbf{D}_{\text{rad}} E_{\text{rad}}. \quad (2.70)$$

The first simplification introduced is that the tensor \mathbf{D}_{rad} is approximated by a scalar diffusion coefficient

$$D_{\text{rad}} = \frac{\lambda c}{\chi_{\text{R}}}, \quad (2.71)$$

where λ is a dimension-less flux-limiter function and χ_{R} is the reciprocal of the mean absorption length in the medium. Consequently, one has

$$\mathbf{F}_{\text{rad}} = -\frac{\lambda c}{\chi_{\text{R}}} \nabla E_{\text{rad}}. \quad (2.72)$$

Using this, we can rewrite equation (2.69) leading to

$$\frac{\partial E_{\text{rad}}}{\partial t} - \nabla \cdot (D_{\text{rad}} \nabla E_{\text{rad}}) = c\chi_{\text{abs}} (B_{\text{rad}} - E_{\text{rad}}), \quad (2.73)$$

where B_{rad} is the bolometric energy density. In order to solve this equation fully one would need to solve for both E_{rad} as well as the local medium temperature T , as $B_{\text{rad}} = a_{\text{rad}} T^4$, where

$$a_{\text{rad}} = \frac{4\sigma_{\text{SB}}}{c} \quad (2.74)$$

is the radiation constant and σ_{SB} is the Stefan-Boltzmann constant. Furthermore, T is coupled via heating and cooling processes. This would require us to solve the

time-evolution of the local internal energy E_{int} using

$$\frac{\partial E_{\text{int}}}{\partial t} = -c\chi_{\text{abs}}(B_{\text{rad}} - E_{\text{rad}}). \quad (2.75)$$

The code, which we apply, already takes non-thermodynamic changes of E_{int} , such as advection, compression and expansion, into account in its hydrodynamic or magnetohydrodynamic calculations. Therefore, these can be neglected here and in the following. While solving for E_{int} and E_{rad} is a valid approach, tremendous simplifications are possible when assuming that the local radiation field is in equilibrium with the temperature of the medium. This results in E_{int} , B_{rad} and E_{rad} referring to the same temperature. We can thus sum up equation (2.73) and equation (2.75) with the simplification $E_{\text{rad}} = B_{\text{rad}}$. Thus one arrives at

$$\frac{\partial (E_{\text{rad}} + E_{\text{int}})}{\partial t} - \nabla \cdot (D_{\text{rad}} \nabla E_{\text{rad}}) = 0. \quad (2.76)$$

Using the relation

$$E_{\text{int}} = c_V \rho T, \quad (2.77)$$

where c_V is the heat capacity at constant volume and ρ is the volume gas density, one can, along with

$$E_{\text{rad}} = a_{\text{rad}} T^4, \quad (2.78)$$

derive

$$\frac{\partial E_{\text{int}}}{\partial t} = \frac{c_V \rho}{4a_{\text{rad}} T^3} \frac{\partial E_{\text{rad}}}{\partial t}. \quad (2.79)$$

When defining the energy ratio

$$f_c = \left(\frac{c_V \rho}{4a_{\text{rad}} T^3} + 1 \right)^{-1} \quad (2.80)$$

along with equation (2.79) we can rewrite equation (2.76) as a modified diffusion equation

$$\frac{\partial E_{\text{rad}}}{\partial t} - f_c \nabla \cdot (D_{\text{rad}} \nabla E_{\text{rad}}) = 0. \quad (2.81)$$

This now finally allows for a direct solution of this diffusion equation. As stated in Kuiper et al. (2018, submitted) both this approximation as well as the full solution of the coupled equation (2.73) and equation (2.75). Along with this radiation transport, the radiation-matter interaction will, because of the momentum conservation, lead to radiative forces otherwise known as radiation pressure. Again, the details of this are given in Kuiper et al. (2018, submitted). Generally, the acceleration due radiation pressure a_{rad} is given by

$$a_{\text{rad}} = \frac{\kappa}{c} \mathbf{F}_{\text{rad}}, \quad (2.82)$$

2. Physics of Accretion Disks

where $\kappa = \frac{\chi_{\text{R}}}{\rho}$ is the opacity of the medium. Combining this with equation (2.72) we arrive at

$$\mathbf{a}_{\text{rad}} = -\frac{\lambda}{\rho} \nabla E_{\text{rad}}. \quad (2.83)$$

As an alternative to this scheme the Eddington approximation (see e.g. 11.3 in Castor (2004)) can be used which states that

$$p_{\text{rad}} = \frac{E_{\text{rad}}}{3}. \quad (2.84)$$

This can then be used to determine the radiation acceleration. When combining these elaborations with the hydrodynamic equations, equation (2.31), equation (2.32) and equation (2.33), and assuming the equilibrium temperature we obtain

$$\frac{\partial \rho}{\partial t} + \nabla \cdot (\rho \mathbf{v}) = 0 \quad (2.85)$$

$$\frac{\partial \mathbf{m}}{\partial t} + \nabla (\mathbf{m} \cdot \mathbf{v}) + \nabla p - \nabla \sigma = \rho \mathbf{g} - \rho \nabla \Phi_{\text{Gas}} + \rho \frac{\kappa}{c} \mathbf{F} \quad (2.86)$$

$$\frac{\partial E}{\partial t} + \nabla (E \mathbf{v}) + \nabla (p \mathbf{v}) - \nabla \cdot (\sigma \mathbf{v}) + \nabla (\rho \Phi_{\text{Gas}} \mathbf{v}) = \mathbf{m} \cdot \mathbf{g} + \rho \frac{\kappa}{c} \mathbf{v} \cdot \mathbf{F} \quad (2.87)$$

$$\frac{\partial E_{\text{rad}}}{\partial t} = \nabla \cdot (D_{\text{rad}} \nabla E_{\text{rad}}) \quad (2.88)$$

as the system of equations. If we absorb the radiation pressure terms as a part of the total pressure p_{tot} gradients the set of equations reduces to

$$\frac{\partial \rho}{\partial t} + \nabla \cdot (\rho \mathbf{v}) = 0 \quad (2.89)$$

$$\frac{\partial \mathbf{m}}{\partial t} + \nabla (\mathbf{m} \cdot \mathbf{v}) + \nabla p_{\text{tot}} - \nabla \sigma = \rho \mathbf{g} - \rho \nabla \Phi_{\text{Gas}} \quad (2.90)$$

$$\frac{\partial E}{\partial t} + \nabla (E \mathbf{v}) + \nabla (p_{\text{tot}} \mathbf{v}) - \nabla \cdot (\sigma \mathbf{v}) = \mathbf{m} \cdot \mathbf{g} \quad (2.91)$$

$$\frac{\partial E_{\text{rad}}}{\partial t} = \nabla \cdot (D_{\text{rad}} \nabla E_{\text{rad}}). \quad (2.92)$$

This allows us to perform calculations without including the radiation pressure while still considering radiation transport. This is sufficient as we are primarily interested in the dynamics of the disk and not its temperatures and spectra. The latter are reserved for future work. In order to close the system we employ the caloric equation of state for an ideal gas

$$e = \frac{p_{\text{tot}}}{\rho(\gamma - 1)}, \quad (2.93)$$

where e is the specific internal energy of the gas.

2.2.4. Spherical coordinates

As we will employ spherical coordinates for the simulations we shortly introduce the choice of coordinates. The Cartesian coordinate variables x, y, z are given by

$$x = r \sin \theta \cos \varphi \quad (2.94)$$

$$y = r \sin \theta \sin \varphi \quad (2.95)$$

$$z = r \cos \theta, \quad (2.96)$$

where

$$r = \sqrt{x^2 + y^2 + z^2} \quad (2.97)$$

$$\theta = \arccos\left(\frac{z}{r}\right) \quad (2.98)$$

$$\varphi = \arctan\frac{y}{x}. \quad (2.99)$$

It should be noted that, especially for the arctan one has to choose the correct intervals. The ranges of the spherical coordinate variables are

$$r \in (0, \infty) \quad \text{In the later simulation the upper boundary will be limited} \quad (2.100)$$

$$\theta \in [0, \pi] \quad (2.101)$$

$$\varphi \in [0, 2\pi] \quad (2.102)$$

and the conversion of cylindrical variables R, φ, z is given by (hint φ is the same for spherical and cylindrical coordinates)

$$r = \sqrt{R^2 + z^2} \quad (2.103)$$

$$R = r \sin \theta \quad (2.104)$$

$$\theta = \arccos\left(\frac{z}{r}\right) \quad (2.105)$$

$$z = r \cos \theta. \quad (2.106)$$

2.2.5. Gravitational forces

In the AGN system, there are two components of gravity. First, there is the gravity of the central SMBH and secondly there is the self-gravity created by the Accretion Disk (AD) itself. Now let us first explore the gravity of the SMBH

2.2.5.1. Gravity of the central black hole

The gravity forces of the central SMBH will be represented by an acceleration vector. As we are using cylindrical or spherical coordinates for reasons of simplicity we need

2. Physics of Accretion Disks

to calculate the acceleration vector in those two coordinates. Generally,

$$\Phi_{\text{BH}} = -G \frac{M_{\text{BH}}}{r}, \quad \nabla_{\text{Cylindrical}} = \left(\frac{\partial}{\partial R}, \frac{1}{R} \frac{\partial}{\partial \varphi} \right), \quad \nabla_{\text{Spherical}} = \left(\frac{\partial}{\partial r}, \frac{1}{r} \frac{\partial}{\partial \theta}, \frac{1}{r \sin \theta} \frac{\partial}{\partial \varphi} \right), \quad (2.107)$$

where M_{BH} is the mass of the central SMBH, G is the gravitational constant, r is the spherical radius and R is cylindrical radius. Thus, we arrive at

$$\mathbf{g}_{\text{BH, cyl}} = -\nabla_{\text{Cylindrical}} \Phi_{\text{BH}} = -\frac{GM_{\text{BH}}}{r^3} \begin{pmatrix} R \\ 0 \\ z \end{pmatrix} \quad (2.108)$$

for the cylindrical gravitational acceleration and

$$\mathbf{g}_{\text{BH, spher}} = -\nabla_{\text{Spherical}} \Phi_{\text{BH}} = -\frac{GM_{\text{BH}}}{r^2} \begin{pmatrix} 1 \\ 0 \\ 0 \end{pmatrix} \quad (2.109)$$

for the spherical gravitational acceleration.

2.2.6. Self-gravity

Self-gravity is included as a potential Φ derived from the mass distribution. The latter is inferred from the density distribution of the AD via the Poisson equation (see e.g. Kuiper et al. (2010a))

$$\Delta \Phi_{\text{Gas}} = 4\pi \rho G. \quad (2.110)$$

2.3. Equilibrium initial conditions

Firstly, we need to derive initial conditions which start the disk off in force equilibrium.

2.3.1. Assumptions

We assume that the soundspeed c_S is vertically constant i.e. $\frac{\partial c_S}{\partial z} = 0$. In the ideal gas case, the relation for the speed of sound

$$c_S^2 = \frac{\partial p}{\partial \rho} \quad (2.111)$$

is valid and can be rearranged as

$$\partial p = c_S^2 \partial \rho + \rho \partial c_S^2. \quad (2.112)$$

Additionally, we assume the radial distribution of the density ρ , i.e.

$$\rho(R, z = 0) = \rho_0 R^\beta, \quad (2.113)$$

to be following a power-law as shown in e.g. Shakura and Sunyaev (1973). Moreover, we strive to have an system in equilibrium. Thus, we infer that there is no change in momentum in the R , φ and z directions, i.e.

$$\frac{\partial m_R}{\partial t} = \frac{\partial m_\varphi}{\partial t} = \frac{\partial m_z}{\partial t} = 0. \quad (2.114)$$

Furthermore, there is only a Keplerian rotation, meaning it is restricted to the φ coordinate. The change in momentum is governed by equation (2.90). Because we assume $v_R \ll v_{K,0} \approx v_\varphi$ and $v_z \ll v_{K,0}$ the term $\nabla(\mathbf{m} \cdot \mathbf{v})$ is zero. Additionally, it is assumed that the changes due to self-gravity term $\rho \nabla \Phi_{\text{Gas}}$ and the viscosity term $\nabla \sigma$ are only smaller corrections and the system will equilibrate itself quickly after the start of the simulation. This is because the system will be quite close to the equilibrium.

2.3.2. Derivations from vertical force-balance

The vertical force-balance is calculated from the z component of equation (2.90), which when neglecting the terms described above and requiring force equilibrium reduces to

$$\frac{\partial p_{\text{tot}}}{\partial z} \stackrel{!}{=} \rho \mathbf{g}_z. \quad (2.115)$$

2. Physics of Accretion Disks

Using equation (2.112) and keeping in mind that R is the cylindrical radius and $r = \sqrt{R^2 + z^2}$ is the spherical radius, we consequently obtain

$$\frac{c_S^2}{\rho} \frac{\partial \rho}{\partial z} = -z \frac{GM_{\text{BH}}}{r^3} \quad (2.116)$$

$$\Leftrightarrow \int_0^z \frac{d \ln \rho}{dz'} dz' = \int_0^z -\frac{GM_{\text{BH}}}{c_S^2} z \left(R^2 + z'^2\right)^{-\frac{3}{2}} dz' \quad (2.117)$$

$$\Leftrightarrow \ln \rho_z = \ln \rho_0 - \frac{1}{c_S^2} \frac{GM_{\text{BH}}}{R} \left(\frac{1}{-\sqrt{R^2 + z^2}} + \frac{1}{R} \right) \quad (2.118)$$

$$\Leftrightarrow \ln \rho_z = \ln \rho_0 - \frac{1}{c_S^2} \frac{GM_{\text{BH}}}{R} \left(1 - \frac{1}{\sqrt{1 + \frac{z^2}{R^2}}} \right) \quad (2.119)$$

$$\Leftrightarrow \rho_z = \rho_0 \exp \left(-\frac{v_{\text{K},0}^2}{c_S^2} \left(1 - \frac{1}{\sqrt{1 + \frac{z^2}{R^2}}} \right) \right) \quad (2.120)$$

$$= \rho_0 \exp \left(\frac{v_{\text{K},0}^2}{c_S^2} \left(\frac{R}{r} - 1 \right) \right). \quad (2.121)$$

In these equations ρ_0 is the density in the equatorial plane ($z = 0$), ρ_z is then density for a given z and

$$v_{\text{K},0}^2 = \frac{GM_{\text{BH}}}{R}. \quad (2.122)$$

If we now perform a Taylor expansion for small z up to 2nd order in the exponent we can infer

$$\rho_z = \rho_0 \exp \left(-\frac{v_{\text{K},0}^2}{c_S^2} \frac{z^2}{2R^2} \right) + \mathcal{O}(\exp(z^4)) . \quad (2.123)$$

With this we can define the the scale-height, analogous to equation (2.15),

$$h = \frac{c_S R}{v_{\text{K},0}(R)}. \quad (2.124)$$

When comparing this to equation (1) in Kennedy et al. (2016) we find that the exponential factor in the vertical density dependence is the same. Moreover, the relation is equivalent to equation (25) in Lodato (2008) and equation (2.5) in Shakura and Sunyaev (1973). Hence, we can conclude that it makes sense to assume z to be small for the whole simulation as it is then akin to Kennedy et al. (2016) concerning vertical dependence.

2.3.3. Determination of pressure profile

If we assume h to be a given quantity as in Kennedy et al. (2016) or Lodato (2008) we can use equation (2.124) along with the equation

$$p = \rho c_S^2 \quad (2.125)$$

for an ideal gas to arrive at

$$p = \rho \frac{h^2 v_{K,0}^2(R)}{R^2}. \quad (2.126)$$

2.3.4. Derivation of v_φ from radial force balance

In the following we derive the initial condition for the velocity in the φ direction via the radial force balance under the before mentioned power-law assumption for the radial density distribution as described in equation (2.113). We moreover introduce a reference radius R_d which poses as the radial limit for the disk. Summed up this gives, along with equation (2.123),

$$\rho_0(R) = \rho_{Rd} \left(\frac{R}{R_d} \right)^\beta, \quad (2.127)$$

where ρ_{Rd} is $\rho(R_d)$. This time, we use a stationary version of equation (2.90)'s radial component and again use all previously mentioned assumptions along with the fact that we have another centrifugal component in radial balance

$$\frac{\partial p}{\partial R} = \rho \mathbf{g}_R + \rho \frac{v_\varphi^2}{R}. \quad (2.128)$$

If we hypothetically knew the exact v_φ we could derive $\frac{\partial p}{\partial R}$. Additionally, we can derive the initial v_φ by

$$v_\varphi = \left(\frac{\partial p}{\partial R} \frac{R}{\rho} - R \mathbf{g}_R \right)^{\frac{1}{2}}. \quad (2.129)$$

Using the pressure profile given in equation (2.126), equation (2.124) and using a linear h with a prefactor H (later determined akin to Kennedy et al. (2016)) i.e.

$$\frac{h}{R} = H = \text{const}, \quad (2.130)$$

2. Physics of Accretion Disks

we can calculate

$$v_\varphi = \left[\frac{h^2 R}{R^2 \rho} \left(\frac{\partial \rho}{\partial R} v_{K,0}^2 + \rho \frac{\partial v_{K,0}^2}{\partial R} \right) + v_{K,0}^2 \right]^{\frac{1}{2}} \quad (2.131)$$

$$= \left[\frac{h^2 R}{R^2 \rho} \left(\frac{\beta}{R} + \frac{z^2}{h^2 R} - \frac{1}{R} \right) \rho v_{K,0}^2 + v_{K,0}^2 \right]^{\frac{1}{2}} \quad (2.132)$$

$$= v_{K,0} \left[(\beta - 1) \frac{h^2}{R^2} + \frac{z^2}{R^2} + 1 \right]^{\frac{1}{2}}. \quad (2.133)$$

Summed up, this gives us a initial condition for v_φ , which is the slightly modified Keplerian velocity. Because we only consider small z (i.e. z is close to 0) this reduces to

$$v_\varphi = v_{K,0} \left[(\beta - 1) \frac{h^2}{R^2} + 1 \right]^{\frac{1}{2}} \quad (2.134)$$

2.3.5. Normalisation constant for ρ

We want that the total mass enclosed in the three-dimensional space in which the total diskmass M_d is contained. Thus, we want to determine the constant ρ_0 such that this condition is fulfilled. In order to have a finite radial interval we use the already introduced reference radius R_d i.e. our radial interval is limited to $R \in [0, R_d]$. Consequently, we demand

$$\int_0^{R_d} \int_0^{2\pi} \int_{-\infty}^{\infty} R \rho(R, \varphi, z) dR d\varphi dz \stackrel{!}{=} M_d. \quad (2.135)$$

Using our knowledge gathered so far and the Gaussian integral we conclude:

$$\int_0^{R_d} \int_0^{2\pi} \int_{-\infty}^{\infty} R \rho_{R_d} \left(\frac{R}{R_d} \right)^\beta \exp\left(-\frac{z^2}{2h^2}\right) dR d\varphi dz = \int_0^{R_d} 2\pi \sqrt{2\pi} \rho_{R_d} h R^{\beta+1} R_d^{-\beta} dR \quad (2.136)$$

$$= \frac{2\pi \sqrt{2\pi} h R_d^2}{(\beta + 2)} \rho_{R_d} = M_d. \quad (2.137)$$

Accordingly, the normalisation constant ρ_0 is given by

$$\rho_{R_d} = \frac{\beta + 2}{2\pi \sqrt{2\pi} R_d^2 h} M_d, \quad (2.138)$$

which is equivalent to the one given in Kennedy et al. (2016).

2.3.6. Self-gravity

When self-gravity is included and is acting as a dominant gravitational force, we can only apply the Φ_{Gas} terms in equation (2.90) and thus base the calculations solely on the self-gravitating terms. The hydrostatic equilibrium (see Lodato (2008) and the references therein) results in the vertical density profile

$$\rho(z) = \rho_0 \frac{1}{\cosh^2\left(\frac{z}{2H_{\text{SG}}}\right)}, \quad (2.139)$$

where $H_{\text{SG}} = \frac{c_s^2}{2\pi G\Sigma}$ is the self-gravity scale-height and Σ is the surface density. Despite of this we retain our earlier derived initial conditions also in the radial region where the self-gravity is dominating. This approach is similar in spirit to Kennedy et al. (2016) with the difference that we will employ a linearly-growing scale-height over the entire radial domain. We should thus see a change to a constant scale height. The next subsection covers the scale-height in more detail.

2.3.7. On the scale-height

Shakura and Sunyaev (1973) (in which h is named z_0) supplies equations to determine the scale-height. While constant in the region dubbed “a”, it is proportional to $R^{\frac{21}{20}}$ and $R^{\frac{9}{8}}$ in regions b) and c), respectively. Thus, it is close to a linear dependence in “b)” and “c)” which has inspired Kennedy et al. (2016) to assume a linear R dependence for the scale height until a critical radius R_{SG} is reached. This radius, after which the scale-height becomes constant, marks the break-even point for the central Super Massive Black Hole (SMBH) gravity and self-gravity. As we are also interested in the influence of self-gravity on the scale height we initially prescribe the linearly growing scale-height everywhere. This is opposed to it being constant after R_{SG} as in Kennedy et al. (2016). The constant scale height is chosen such that it fits a radially isothermal profile as described in Just et al. (2012) at R_{SG} . The linear constant is such that the scale-height grows to this value at R_{SG} . Thus,

$$\frac{h}{R} = \frac{h_z R_d}{R_{\text{SG}}}, \quad (2.140)$$

where h_z is a constant prefactor (no unit) and R_{SG} is the radius where the vertical gravitational force at $z = h_z R_d$ generated by the black hole is equivalent the the vertical component of the gravitational force generated by the self gravity, i.e.

$$\frac{GM_{\text{BH}} h_z R_d}{R_{\text{SG}}^3} = 2\pi G u(R_{\text{SG}}). \quad (2.141)$$

2. Physics of Accretion Disks

In this equation $u(R_{\text{SG}})$ is the surface density at the self-gravity radius. The surface density can be determined by calculating $\int_{-\infty}^{\infty} R\rho(R, z)dz$. Consequently,

$$R_{\text{SG}} = \left(\frac{1}{2 + \beta} \frac{M_{\text{BH}}}{M_{\text{d}}} h_z R_{\text{d}} R_{\text{d}}^{2+\beta} \right)^{\frac{1}{3+\beta}} \quad (2.142)$$

$$= \left(\frac{1}{2 + \beta} \frac{M_{\text{BH}}}{M_{\text{d}}} h_z \right)^{\frac{1}{3+\beta}} R_{\text{d}}. \quad (2.143)$$

2.3.8. Resulting initial conditions

Summing this all up we conclude:

$$\rho = \frac{2 + \beta}{2\pi\sqrt{2\pi}R_{\text{d}}^2h} M_{\text{d}} \left(\frac{R}{R_{\text{d}}} \right)^{\beta} \exp\left(-\frac{z^2}{2h^2}\right) \quad (2.144)$$

$$p = \rho \frac{h^2 v_{\text{K},0}(R)}{R^2} \quad (2.145)$$

$$v_R = 0 \quad (2.146)$$

$$v_{\varphi} = v_{\text{K},0}(R) \left((\beta - 1) \frac{h^2}{R^2} + 1 \right)^{\frac{1}{2}} \quad (2.147)$$

$$v_z = 0. \quad (2.148)$$

Note: Obviously, these results can easily be transferred to spherical coordinates, i.e.

$$v_r = 0 \text{ and } v_{\theta} = 0. \quad (2.149)$$

The changes to the other quantities merely change by replacing

$$R = r \sin \theta, \quad z = r \cos \theta \quad (2.150)$$

in equation (2.144), equation (2.145) and equation (2.147).

2.3.9. Viscosity corresponding to the initial conditions

Now we can calculate the $R\varphi$ element, as derived in equation (2.65), of the viscosity tensor σ using these initial conditions and the assumption

$$\frac{\partial v_R}{\partial \varphi} = 0 \quad (2.151)$$

as the initial conditions are axis-symmetric. Additionally, we switch from the kinematic viscosity formulation to the shear viscosity i.e.

$$\mu = \rho \nu_{\text{shear}}. \quad (2.152)$$

Consequently, the viscosity tensor element is given by

$$\sigma_{R\varphi} = \rho\nu_{\text{shear}} \left(0 - \frac{1}{2} \frac{v_\varphi}{R} - \frac{v_\varphi}{R} \right) \quad (2.153)$$

$$= -\frac{3}{2} \rho\nu_{\text{shear}} \frac{v_\varphi}{R}, \quad (2.154)$$

which is consistent to Lodato (2008). Shakura and Sunyaev (1973) derives its equation (1.2)

$$\sigma_{R\varphi} = -\alpha\rho c_s^2, \quad (2.155)$$

where c_s is the sound speed and α is the already introduced parameter from Shakura and Sunyaev (1973). Along with the α disk property

$$\frac{h}{R} = \frac{c_s}{v_\varphi} \quad (2.156)$$

one obtains

$$\sigma_{R\varphi} = -\alpha\rho h^2 \frac{v_\varphi^2}{R^2}. \quad (2.157)$$

Comparing this to equation (2.154) we can conclude that

$$\nu_{\text{shear}} = \frac{2}{3} \alpha h^2 \frac{v_\varphi}{R}. \quad (2.158)$$

When looking at equation (13) in Kuiper et al. (2010a) we realise that this is only consistent if

$$\alpha_{\text{K10}} = \frac{2}{3} \alpha, \quad (2.159)$$

where α_{K10} is an alternative α definition used in Kuiper et al. (2010a).

2.3.10. Toomre Q

As described in e.g. Toomre (1964), the stability of disk-like equilibrium systems is described by the Q_{Toomre} parameter which is given by

$$Q_{\text{Toomre}} = \frac{c_s \kappa}{\pi G u}. \quad (2.160)$$

In this expression κ is the epicyclic frequency and u is the surface density. For a Keplerian disk, as assumed here,

$$\kappa = \frac{v_{\text{K}, z=0}(R)}{R}. \quad (2.161)$$

2. Physics of Accretion Disks

When comparing equation (2.160) with the criterion for R_{SG} in equation (2.141) and insert

$$h = \frac{c_s R}{v_{\text{K}, z=0}}, \quad (2.162)$$

$h = h_z R_d$ at R_{SG} we find

$$\frac{GM_{\text{BH}} h}{R_{\text{SG}}^3} = 2\pi G \Sigma(R_{\text{SG}}) \quad (2.163)$$

$$\Leftrightarrow \frac{v_{\text{K},0}^2 c_s R_{\text{SG}}}{R_{\text{SG}}^2 \pi G \Sigma(R_{\text{SG}}) v_{\text{K},0}^2} = 2 \quad (2.164)$$

$$\Leftrightarrow \frac{\kappa c_s}{\pi G \Sigma(R_{\text{SG}})} = 2 \quad (2.165)$$

$$\Leftrightarrow Q_{\text{Toomre}}(R_{\text{SG}}) = 2. \quad (2.166)$$

Hence, the $Q_{\text{Toomre}} = 2$ at the self-gravity radius, which is close to the stability criterion stating that the disk is stable if

$$Q_{\text{Toomre}} > 1. \quad (2.167)$$

The proximity of the two radii emphasises the connection between Q_{Toomre} and the vertical force balance as the source of the instability is the vertical force imbalance between the central gravity and self-gravity. To determine which radius is the boundary for the stability criterion, using the beforementioned initial conditions, we first calculate

$$u = \int_{-\infty}^{\infty} \rho(R, z) dz = \rho_0 R^\beta \sqrt{2\pi} h = \frac{2 + \beta}{2\pi} R_d^{-(2+\beta)} M_d R^\beta. \quad (2.168)$$

Combined with the density profile, given in equation (2.144), as well as $\frac{h}{R} = \frac{c_s}{v_{\text{K},0}}$ derived above we can continue the calculation as

$$Q_{\text{Toomre}} = \sqrt{\frac{h^2 v_{\text{K},0}^2}{R^2} \frac{v_{\text{K},0}}{G\pi R} \frac{R_d^{2+\beta} R^{-\beta} 2\pi}{(2 + \beta) M_d}} \quad (2.169)$$

$$= h \frac{v_{\text{K},0}^2}{GM_d} \frac{2R_d^{2+\beta}}{2 + \beta} R^{-(\beta+2)} \quad (2.170)$$

$$= h \frac{GM_{\text{BH}}}{RM_d G} \frac{2R_d^{2+\beta}}{2 + \beta} R^{-(2+\beta)} \quad (2.171)$$

$$\Leftrightarrow R^{3+\beta} = h \frac{M_{\text{BH}}}{M_d} \frac{2R_d^{2+\beta}}{2 + \beta} \frac{1}{Q_{\text{Toomre}}} \quad (2.172)$$

$$\Leftrightarrow R = \left(h \frac{M_{\text{BH}}}{M_d} \frac{2R_d^{2+\beta}}{2 + \beta} \frac{1}{Q_{\text{Toomre}}} \right)^{\frac{1}{3+\beta}} \quad (2.173)$$

If we set $h = h_z R_d$, as in Kennedy et al. (2016), and compare it to R_{SG} we arrive at

$$R = \left(\frac{2}{Q_{\text{Toomre}}} \right)^{\frac{1}{3+\beta}} \left(h_z \frac{M_{\text{BH}}}{M_d} \frac{1}{2+\beta} \frac{1}{Q_{\text{Toomre}}} \right)^{\frac{1}{3+\beta}} R_d = \left(\frac{2}{Q_{\text{Toomre}}} \right)^{\frac{1}{3+\beta}} R_{\text{SG}}. \quad (2.174)$$

So the unstable region ($Q_{\text{Toomre}} \leq 1$) always begins slightly after the vertical self-gravity starts dominating (i.e. $R > R_{\text{SG}}$) if $\beta + 3 > 0$. As we are not using the constant scale-height after R_{SG} as in Kennedy et al. (2016), but are linear all the way ($h = \frac{h_z R_d R}{R_{\text{SG}}}$) the result changes to

$$R = \left(\frac{2}{Q_{\text{Toomre}}} \right)^{\frac{1}{2+\beta}} R_{\text{SG}}^{-\frac{1}{2+\beta}} \left(h_z \frac{M_{\text{BH}}}{M_d} \frac{1}{2+\beta} \right)^{\frac{1}{2+\beta}} R_d^{\frac{3+\beta}{2+\beta}} \quad (2.175)$$

$$= \left(\frac{2}{Q_{\text{Toomre}}} \right)^{\frac{1}{2+\beta}} R_{\text{SG}}^{-\frac{1}{2+\beta}} R_{\text{SG}}^{\frac{3+\beta}{2+\beta}} \quad (2.176)$$

$$= \left(\frac{2}{Q_{\text{Toomre}}} \right)^{\frac{1}{2+\beta}} R_{\text{SG}}. \quad (2.177)$$

Hence, the general property is preserved, but is slightly shifted and $2 + \beta > 0$ is the required parameter condition securing that the radius at which $Q_{\text{Toomre}} = 1$ is larger than R_{SG} .

2.4. The drag force as the force the stars feel from the Accretion Disk (AD) for N-body simulations

The stars in the Nuclear Star Cluster (NSC) are orbiting the central Super Massive Black Hole (SMBH) and some of them will at some point cross the AD. Direct N-body simulations are used to investigate the evolution of these stars. To incorporate the AD we need to consider its interactions with single stars. Just et al. (2012), Kennedy et al. (2016) both discuss the force and the resulting acceleration the disk will exhibit on stars crossing it. This section is mainly based on those papers. The main effects contributing, according to Just et al. (2012), Kennedy et al. (2016), is the ram pressure due to the bow shock. The drag force \mathbf{F}_{drag} acting on a single star is given by

$$\mathbf{F}_{\text{drag}} = Q_{\text{d}}\pi r_*^2 \rho |\mathbf{v}_{\text{rel}}| \mathbf{v}_{\text{rel}}, \quad (2.178)$$

where Q_{d} is the drag coefficient, r_* is the radius of the star, ρ is the AD's mass density of the current location of the star and \mathbf{v}_{rel} is the relative velocity of the star relative to the AD. Kennedy et al. (2016) states that Q_{d} is an uncertain factor, but that its estimation is possible from the shock-conditions detailed in the references within Kennedy et al. (2016). Thus, the value used henceforth is

$$Q_{\text{d}} = 5. \quad (2.179)$$

Furthermore, it needs to be considered that all currently possible N-body simulations are unable to recreate a sufficient number of particles. Consequently, we need to make one particle in the simulation represent multiple stars which in turn also means the real drag coefficient needs to be rescaled following the formula

$$Q_{\text{tot}}(N) = Q_{\text{d}}N \left(\frac{r_*}{R_{\text{d}}} \right)^2, \quad (2.180)$$

where N is the real number of stars in the NSC and R_{d} is the influence radius as discussed before. Thus, one can combine this to

$$\mathbf{F}_{\text{drag}} = Q_{\text{tot}}(N) \frac{R_{\text{d}}^2}{N} \pi \rho |\mathbf{v}_{\text{rel}}| \mathbf{v}_{\text{rel}}. \quad (2.181)$$

The dynamical timescale

$$t_{\text{dyn}} = \left(\frac{r_{\text{h}}}{GM_{\text{Cl}}} \right)^{\frac{1}{2}}, \quad (2.182)$$

where r_{h} is the half-mass radius of the cluster, G is the gravitational constant and M_{Cl} is the total cluster mass, for the NSC stays the same no matter the particle number. However we face the problem that the relaxation time

$$t_{\text{rx}}(N) = \frac{0.14N}{\ln 0.4N} t_{\text{dyn}}, \quad (2.183)$$

2.4. The drag force as the force the stars feel from the AD for N -body simulations

where N is an arbitrary particle number, changes depending on the number of particles used. Thus, we want the drag force to be effective at the correct timescale. This can be reached by defining

$$Q_{\text{tot}}(N_{\text{sim}}) = \frac{t_{\text{rx}}(N_{\text{real}})}{t_{\text{rx}}(N_{\text{sim}})} Q_{\text{tot}}(N_{\text{real}}) = Q_{\text{d}} \frac{N_{\text{real}}^2 \ln 0.4 N_{\text{sim}}}{N_{\text{sim}} \ln 0.4 N_{\text{real}}} \left(\frac{r_*}{R_{\text{d}}} \right)^{\frac{1}{2}}, \quad (2.184)$$

where N_{sim} is the number of particles used in the simulation and N_{real} is the real number of stars in the NSC. Using $R_{\text{d}} = 10$ pc, 2.0×10^9 sun-like stars and 4000 simulated stars we arrive at

$$Q_{\text{tot}}(4000) = 0.01. \quad (2.185)$$

This number is now used and is rescaled to the proper number of simulated particles via

$$Q_{\text{tot}}(N_{\text{real}}) = \frac{\ln(0.4 \cdot 4000)}{4000} \frac{N_{\text{real}}}{\ln 0.14 N_{\text{real}}} Q_{\text{tot}}(4000). \quad (2.186)$$

As the code is using in the acceleration corresponding to the drag force we just divide equation (2.181) by the mass of the individual star (m_*) to arrive at the drag acceleration

$$\mathbf{a}_{\text{drag}} = Q_{\text{tot}}(N_{\text{sim}}) \frac{R_{\text{d}}^2}{N_{\text{sim}} m_*} \pi \rho |\mathbf{v}_{\text{rel}}| \mathbf{v}_{\text{rel}}. \quad (2.187)$$

3. Numerical simulations using the PLUTO code and NBODY6++GPU

3.1. Astrophysical system

The astrophysical system considered is an Active Galactic Nucleus (AGN) composed of an accretion disk, a Super Massive Black Hole (SMBH) and the surrounding Nuclear Star Cluster (NSC). While we do not consider the NSC in the hydrodynamical simulations, it will be the main focus in the simulations using NBODY6++GPU.

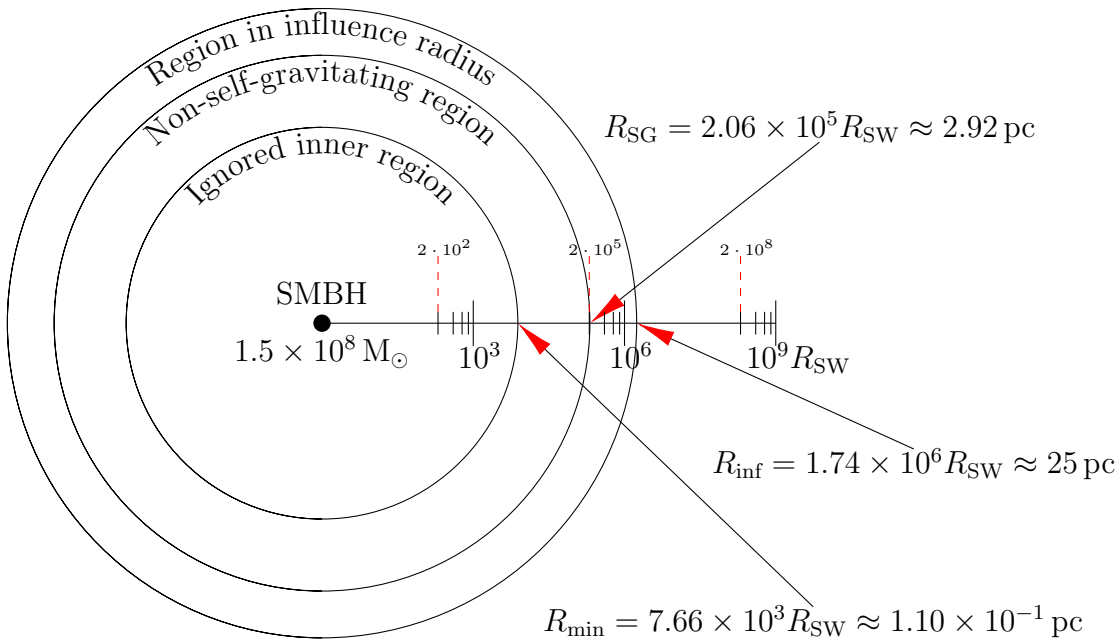


Figure 3.1.: Detailed figure of the radial structure of the physical system used in the simulation. In the very centre one can see the SMBH. The radial scaling is done in a logarithmic scaling using base 1.0×10^3 in units of the Schwarzschild radius. The boundaries of the computational domain at both radial ends and the region where self-gravity starts to dominate the vertical gravity force are marked. The distance to the SMBH is always large enough such that Newtonian physics can be applied.

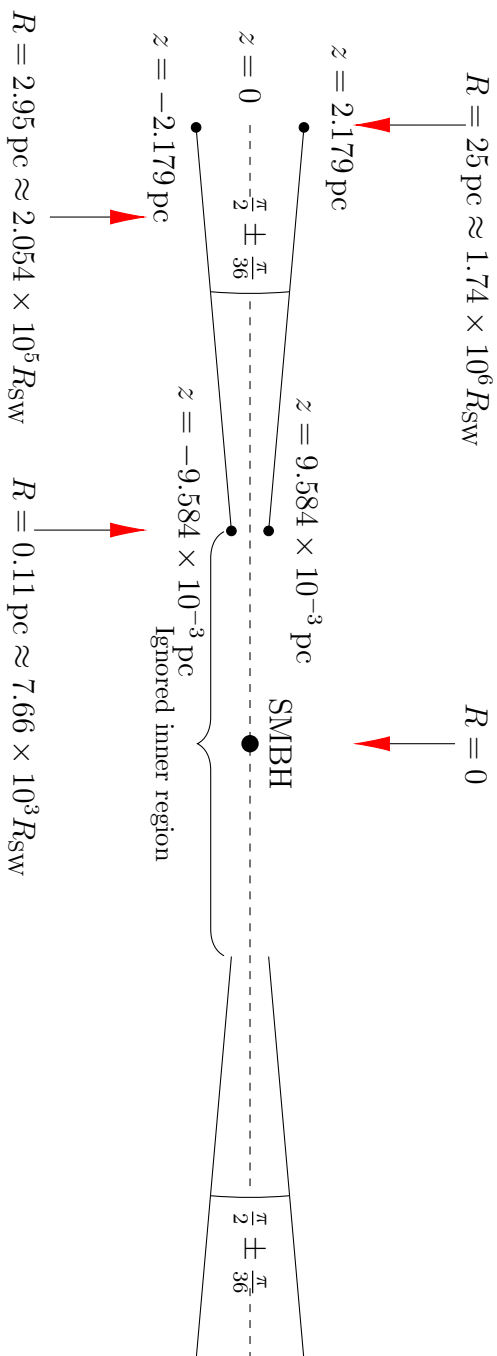


Figure 3.2.: Figure illustrating the vertical set-up of the system of the SMBH. In the centre the SMBH is displayed along with the region that is not considered in the simulations. Then, the vertical and radial extension is illustrated. The radial structure is the same as in Fig. 3.1, i.e. $r \in [0.11 \text{ pc}, 25.0 \text{ pc}]$ as illustrated by the arrows. As $\theta \in [\frac{\pi}{2} - \frac{\pi}{36}, \frac{\pi}{2} + \frac{\pi}{36}]$ we end up with a radius-dependent, i.e. $z_{\text{max/min}} = \pm z_{\text{max}}(r)$, domain coverage in height.

3.2. The PLUTO Code

This section is an extended and adapted version of Section 3.3 “PLUTO” from my master thesis Klein (2014). Each paragraph was adapted language-wise and partly updated or extended. The general structure and content was kept untouched apart from adding the last two subsections.

The PLUTO code is a freely-distributed code jointly developed by the Dipartimento di Fisica, Torino University, INAF, Osservatorio Astronomico di Torino and the SCAI Department of CINECA. This subsection primarily follows Mignone et al. (2007). In it, the PLUTO code is presented as a code designed to be able to treat a wide range of astrophysical flows in the presence of great discontinuities especially for hypersonic flows. In order to achieve this, the code uses high-resolution shock-capturing. For dealing with larger system the code uses parallelisation by MPI. The four physics modules available treat Newtonian fluid dynamics, Magneto Hydrodynamics (MHD) in Newtonian physics, fluid dynamics in Special Theory of Relativity (STR) and MHD in the regime of STR, respectively. Thus, PLUTO possesses a framework for integrating systems of conservation laws. PLUTO is able to solve the Euler equations along with the induction equation for MHD including source terms for e.g. gravity or other body forces. Additionally, viscosity, the processes of thermal conduction, resistivity and optically thin cooling can be included inducing parabolic terms into the equations. The code is written in a very modular way. In order to achieve this, the different solvers and physics modules are separate entities in the code. The very core of the solver has been built on Godunov-type finite volume techniques i.e. “a piecewise polynomial reconstruction followed by the solution of a Riemann problem at zone interfaces and a final evolution stage.” (Mignone et al. 2007).

3.2.1. Basic discretisation scheme

All conservation equations involved in fluid dynamics have the form

$$\frac{\partial \mathbf{U}}{\partial t} = -\nabla \cdot \mathbf{T}(\mathbf{U}) + \mathbf{S}(\mathbf{U}), \quad (3.1)$$

where $\mathbf{T}(\mathbf{U})$ is a tensor of rank two describing the fluxes associated with every component of the conservative quantity \mathbf{U} and $\mathbf{S}(\mathbf{U})$ defines the source/sink terms of the equation. It should be noted that additional source terms might emerge from the gradient of the fluxes. In order to perform the calculations, one also needs a set of primitive variables \mathbf{V} along with methods to convert between them and the conservative quantities. The set of conservative quantities consists of the density ρ , the momentum density \mathbf{m} , the total energy density E and optionally the magnetic field \mathbf{B} . In contrast, the set of primitive variables consists of the density ρ , the velocity \mathbf{v} , the gas pressure p and the magnetic field \mathbf{B} . These converters are also known to enforce physical constraints like pressure positivity for all cases and subluminal motion in the case of relativistic flows. To this end, so called mapper-functions are used. As usual, finite volume schemes use shock-capturing techniques by using a time evol-

3. Numerical simulations using the PLUTO code and NBODY6++GPU

ution of volume averages. Generally speaking, this consists of six steps as illustrated below.

- (1) Averaging:
Create the cell averages from the polynomial approximations in the cells.
- (2) Convert:
In this step the primitive variables are recovered from the conservative variables (e.g. by using the equation of state).
- (3) States:
For each zone in a finite volume cell, two states (left and right) are created with a discontinuity between them.
- (4) Riemann:
A Riemann solver solves the Riemann problem constructed in the previous step for all zones in each finite volume cell.
- (5) Update:
Advance the cell averages in time using a time discretisation
- (6) Reconstruction:
Use interpolation routines to recover the polynomial approximations from the cell averages.

One needs, consequently, several building blocks in order to implement this scheme. Following the modular philosophy of PLUTO, all building blocks should be created such that one can always switch each building block for another one of the same type. Generally, we need a cell-average calculator, including one for staggered grid quantities in the case of vectorial quantities like the magnetic field, a conversion function from conservative to primitive variables, a Riemann solver, a suitable time discretisation and an applicable interpolation procedure. Of course one also needs functions providing the correct fluxes and the source functions, if they exist.

3.2.2. Available grids

What went unmentioned before is the theatre, where all the calculations play in: The grid. PLUTO is able to create and process Cartesian, polar and spherical grids in up to three dimensions. For this purpose PLUTO uses logically rectangular grids of orthogonal curvilinear coordinates. The domain decomposition technique is used in order to enable parallel computations with the PLUTO code using the MPI standard (Forum 2018). As hinted upon in Mignone et al. (2007) and officially finished and published in Mignone and Zanni (2012), the PLUTO code is now able to make use of adaptive mesh refinement using the CHOMBO library (Colella et al. 2003).

3.2.3. Riemann solver

As the name suggests this class of solvers is applied to Riemann problems. This refers to initial value problems that have two states separated by a discontinuity as initial conditions, i.e.

$$\mathbf{U}(x, t_0) = \begin{cases} U_{+,L} & \text{if } x < x_+ \\ U_{+,R} & \text{if } x > x_+ \end{cases}. \quad (3.2)$$

Also required is a one-dimensional evolution equation for \mathbf{U} governing the evolution. In case of one dimension, one can theoretically solve a Riemann problem analytically. As the analytical solution requires the decay of non-linear waves, it can be quite complicated and computationally expensive. Hence, numerical Riemann solvers, which are based on different approximation levels, are generally used in upwind type schemes. Because we make use of the *hll* solver, a short introduction to it is given in the following. The basic idea is to approximate the solution by a limited number of N waves for which $\lambda_{k+1} > \lambda_k$ or $k \in [1, N - 1]$, where λ_k is the k -th waves' wavelength. Moreover, we require that these waves should be separated by $N + 1$ states. The flux function is calculated as

$$\mathbf{F} = \begin{cases} \mathbf{f}_L & \text{if } \lambda_1 > 0 \\ \mathbf{f}_k & \text{if } \lambda_k \lambda_{k+1} < 0, \\ \mathbf{f}_R & \text{if } \lambda_N > 0 \end{cases}, \quad (3.3)$$

where the \mathbf{f}_k are calculated by suitably parametrising the Rankine-Hugoniot jump conditions across each wave. These conditions are given by

$$\lambda_k(\mathbf{U}_{k+1} - \mathbf{U}_k) = \mathbf{f}_{k+1} - \mathbf{f}_k. \quad (3.4)$$

The *hll* solver is the case corresponding to $N = 2$. More details can be found in the book Toro (2009).

3.2.4. Time discretisation schemes

The PLUTO code offers several explicit time discretisation schemes. ‘‘Explicit’’ refers to the fact that only the current and previously known state of the system is used to arrive at the solution advanced in time i.e.

$$S(t_{n+1}) = f(S(t_n), S(t_{n-1}), \dots, S(t_{n-N})), \quad (3.5)$$

where $S(t_{n+1})$ is the state of the system in the next time-step, $S(t_n)$ is the current state of the system, $S(t_{n-m})$ are consequently other former states and f is a function mapping from a number of N previous states to the next time-step. Usually, stability constraints apply for explicit time stepping. In most cases there is a condition imposed on the time step that involves parameters from the equation(s) and the mesh. For our flow-type problems with explicit time-discretisation, this is primarily given by the

CFL condition first described in Courant et al. (1928), which is given by

$$C = \Delta t \left(\frac{|\lambda_{\max}|}{\Delta x_{\min}} \right), \quad (3.6)$$

where λ_{\max} denotes the largest signal velocity and Δx_{\min} describes the minimum cell length. This obviously limits the time step size and is one of the major limitations of explicit schemes. While most problems considered here allow for $C \leq 1$, some schemes also permit a smaller or larger CFL number as a maximum or minimum. There are many explicit time discretisations of varying order. Depending on the latter and their calculation steps, a varying number of Riemann solvers calls are needed for every time-step in every cell, also depending on the spatial dimension of the grid. The Runge-Kutta schemes employed in the later calculations are well known time discretisation and will not be discussed in more detail here. For more details the interested reader is again referred to Toro (2009).

3.2.5. Interpolation schemes

The interpolation schemes are used in the reconstruction step, where one recovers the piecewise polynomial approximation to \mathbf{V} in each cell from the corresponding cell averages. Using the notation of Mignone et al. (2007), this means that we start from

$$\mathbf{V}_{\pm,S} = \mathcal{I}(\mathbf{P}, \mathbf{V}), \quad (3.7)$$

where $\mathbf{P}(\mathbf{x})$ represents the polynomial interpolation of \mathbf{V} in each cell and S describes the right or left hand zone side. Moreover, \mathcal{I} denotes the interpolation routine giving the values interpolated at the edges in every cell such that

$$\mathbf{V}_{l,+} = \lim_{\mathbf{x} \rightarrow \mathbf{x}_+} \mathcal{P}(\mathbf{x}) \quad (3.8)$$

or

$$\mathbf{V}_{l,-} = \lim_{\mathbf{x} \rightarrow \mathbf{x}_-} \mathcal{P}(\mathbf{x}), \quad (3.9)$$

respectively. In the notation of Mignone et al. (2007) L and R denote the left or right-hand side cell interface. As stated in Mignone et al. (2007) and Toro (2009), reconstruction methods are required to fulfil monotonicity constraints in pursuance of preventing spurious oscillations in the vicinity of discontinuities and steep gradients.

$$\mathbf{V}_{\pm,S} = \mathbf{V} \pm \frac{\Delta \tilde{\mathbf{V}}}{2} \quad (3.10)$$

exemplifies the procedure for a 2nd order linear interpolant. The slope $\tilde{\mathbf{V}}$ is calculated by a limit procedure as

$$\Delta \tilde{\mathbf{V}} = \sum_k \Delta \tilde{w}_k \mathbf{r}_k, \quad (3.11)$$

where $\Delta\tilde{w}_k = \lim(\Delta\tilde{w}_{k,+}, \Delta\tilde{w}_{k,-})$ and \mathbf{r}_k denotes the set of left eigenvectors of the primitive equations and k is labelling the k -th characteristic field. Additionally, \lim represents a slope limiter. In equation (3.11) the set of right eigenvectors of the primitive equations are denoted by \mathbf{r}_k , whereas the forward (+) and backward (-) derivatives are given by

$$\Delta w_{k,\pm} = \pm \mathbf{l}_l \cdot (\mathbf{V}_{i\pm 1} - \mathbf{V}_i). \quad (3.12)$$

The so-called slope limiters possess distinct characteristic steepening properties and can be applied to both the primitive variables as well as a characteristic fields. Furthermore, this can be done independently of one another. As stated in Mignone et al. (2007) the available interpolation schemes are:

- FLAT: 1st order
- LINEAR 2nd order
- CONVEX ENO: 3rd order convex, see Zanna et al. (2002)
- PARABOLIC: 3rd order in smooth regions, for details see Mignone et al. (2005)
- WENO: Finite difference scheme, 5th order (only hydrodynamics), see Jiang and Shu (1996)

3.2.5.1. Physical module used

We employ the so called HD module which in PLUTO itself consists of the set of equations

$$\frac{\partial}{\partial t} \begin{pmatrix} \rho \\ \mathbf{m} \\ E \end{pmatrix} + \nabla \cdot \begin{pmatrix} \rho \mathbf{m} \\ \mathbf{m} \cdot \mathbf{v} + p \mathbf{I} \\ (E + p) \mathbf{v} \end{pmatrix}^T, \quad (3.13)$$

where ρ is the mass density, \mathbf{v} is the velocity vector, $\mathbf{m} = \rho \mathbf{v}$ is the momentum density, p is the gas pressure, \mathbf{I} is the unit 3x3 tensor, T refers to the transposed matrix and E is the total energy calculated via

$$E = \frac{p}{\gamma - 1} + \frac{|\mathbf{m}|^2}{2\rho}. \quad (3.14)$$

Finally, γ is the adiabatic index. The before-mentioned set of primitive variables is thus given by

$$\mathbf{V} = (\rho, \mathbf{v}, p)^T. \quad (3.15)$$

There are several Riemann solvers offered for this module. Among them the hll scheme which will be employed later. For details see the references in Mignone et al. (2007). It should be noted that certain curvilinear coordinates may introduce additional source terms to some of the equations, which are integrated explicitly during the advection step by adding their contribution to the right hand side of the equations. Furthermore, parabolic terms e.g. emerging from the viscosity or the magnetic field in other physical

3. Numerical simulations using the PLUTO code and NBODY6++GPU

modules can also introduce more source terms. These terms introduce second order spatial derivatives. Thus, the solution of diffusion equations included in the original conversation law picks up the an additional time-step constraint. This is given by

$$\Delta t = \min(\Delta t^{\text{ad}}, \Delta t^{\text{par}}), \quad (3.16)$$

where Δt^{ad} is the advection time-step determined by the CFL condition (see equation (3.6)) and

$$\Delta t^{\text{par}} < 0.5 \min_{d=1,2,3} \left[\frac{(\Delta x^d)^2}{\max(\sigma)} \right], \quad (3.17)$$

where $d = 1, 2, 3$ is the dimension, $0.5 \min_{d=1,2,3}$ is the minimum all the dimensions. Moreover, Δx^d is the lowest cell-size in dimension d and σ is a characteristic velocity squared of the parabolic quantity in question.

3.2.5.2. Body forces

As described in its userguide, PLUTO allows the addition of body forces either via an acceleration vector \mathbf{g} or a potential Φ . These terms are added as source terms i.e.

$$S_{\text{gravity}} = \begin{pmatrix} 0 \\ -\rho \nabla \Phi_{\text{Gas}} + \rho \mathbf{g} \\ -\nabla \cdot (\rho \Phi) \mathbf{v} + \mathbf{m} \cdot \mathbf{g} \end{pmatrix}. \quad (3.18)$$

While arbitrary forces can be put into these, this is constructed such that Newtonian gravity can be easily added to the code.

3.2.5.3. Viscosity

The non-ideal effect of viscosity results in solving the Navier-Stokes equations instead of the Euler equations. The involved viscous stress tensor given by

$$(\Pi)_{ij} = 2 \frac{\nu_1}{h_i h_j} \left(\frac{v_{i;j} + v_{j;i}}{2} \right) + \left(\nu_2 - \frac{2}{3} \nu_1 \right) \nabla \cdot \mathbf{v} \delta_{ij}, \quad (3.19)$$

where ν_1 is the shear viscosity, ν_2 is the bulk viscosity, h_i is the ‘‘geometrical element’’ of the respective direction, $v_{i;j}$ denotes the covariant derivative of the v_i component by the j -th coordinate, $v_{j;j}$ is the covariant 4-divergence of v . The covariant derivatives are needed for the non-Cartesian coordinates as described in the PLUTO user guide. This tensor adds $\nabla \cdot \Pi$ to the left hand side of the momentum equation and a $\nabla \cdot (\mathbf{v} \cdot \Pi)$ to the left hand side of the energy equation. Comparing equation (3.19) with equation (2.34) we see a very close resemblance apart form the h terms. These, however, are only important for the grids used in PLUTO. Thus, we could infer by equation (2.158) that

$$\nu_2 = \frac{2}{3} \alpha h^2 \frac{v_\varphi}{R}. \quad (3.20)$$

However, Kuiper et al. (2010a) uses a different definition of α as visible in equation (9) that absorbs the factor $\frac{2}{3}$. As the equation (7) therein reveals that the same tensor is used as in our calculation. Consequently, we always assign

$$\nu_2 = \alpha h^2 \frac{v_\varphi}{R}. \quad (3.21)$$

Thus, we have to take this into account when comparing it to Shakura and Sunyaev (1973) and Kennedy et al. (2016). Moreover, $\nu_2 = 0$ is set, because it vanishes according to molecular theory for mono-atomic gases as mentioned in Toro (2009).

3.2.6. Modules by Rolf Kuiper

Rolf Kuiper has written additional modules for PLUTO that are adding additional physics via source terms. A good overview can be obtained from Kuiper et al. (2018, submitted). Fig. 3.3 illustrates the interoperation and sequence of the modules, which is indicated by the dotted arrows. The starting point is the self-gravity module “Haumea” (to which external initial conditions are fed). The connected red boxed represent the output quantities (if they are fed to another module). The yellow arrows graphically represent which quantities are send as input parameters. Moreover, the green arrows represent dependent quantities that are updated. One can easily see that PLUTO is the central part for all the modules. The simulations in this thesis only use the “Stellar Gravity” module, the self-gravity module “Haumea” and the radiation transport module “Makemake”. “Stellar Gravity” is not a real module, but a two function calls allowing one to conveniently add external forces in PLUTO as described in Subsubsection 3.2.5.2. Thus, only these are covered in more detail in close reference to Kuiper et al. (2018, submitted) and previous papers about the modules. On top of that irradiation and dust temperatures are not considered in the “Makemake” module for this thesis for now.

3.2.6.1. “Makemake” (Flux Limited Diffusion (FLD))

The “Makemake” module deals mainly with radiation transport and radiation pressure in the FLD approximation as described in Subsection 2.2.3. If we again take a look at Fig. 3.3 we see that “Makemake” is fed the gas density ρ . In the following, it determines the radiative flux along with the radiative forces (not depicted) and the new gas temperature. These are then fed back to PLUTO and used as source terms and for the determination of the new gas pressure. Note that all quantities related to unused modules stay unmentioned here. Let us now take a look how the module actually determines these quantities using the formalism explained in Subsection 2.2.3. While Kuiper et al. (2018, submitted) does not give many implementation details, Kuiper et al. (2010b) provides more information on that. In Fig. 3.4, taken from this paper, we can see the main loop of “Makemake”. First the FLD equations are solved using an implicit solver which will provide the new radiation energy density. This will then be used in order to update the temperature profile using an iterative Newton-Update.

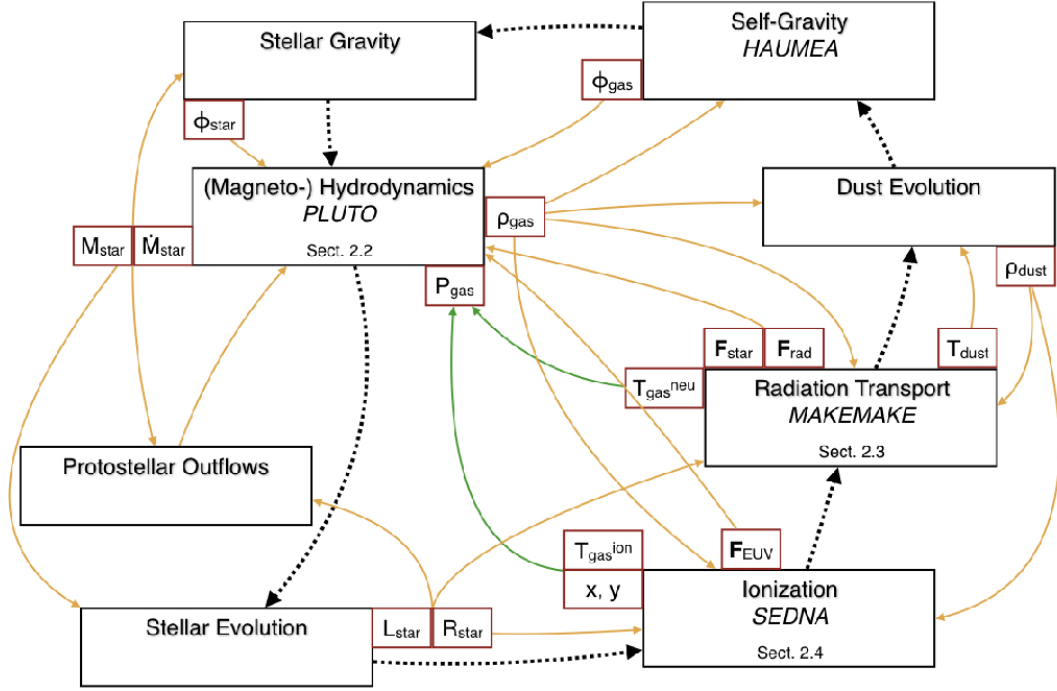


Figure 3.3.: “Flow chart of the overall multi-physics numerical framework for astrophysical fluid dynamics. Black boxes represent module for a specific physical task. Connected red boxes to the modules represent their output quantities; output quantities of a module are only shown, if they denote an input for another module. Black dotted arrows represent the call sequence of the different modules; the main loop starts from pre-defined initial conditions by calling the self-gravity module. Yellow arrows denote input quantities. Green arrows denote update of a dependent quantity” (Kuiper et al. 2018, submitted), also taken from there; ρ_{gas} is the gas density, p_{gas} is the gas pressure, \mathbf{F}_{rad} is the radiative flux, T_{gas} is the gas temperature and Φ_{Gas} is the potential generated by the self-gravity of the AD

As no irradiation is considered the “Initial Setup” is reduced to just supplying the density distribution. Eq. (16) from Kuiper et al. (2010b) is equivalent to equation (2.73) in this thesis. It should be noted that Kuiper et al. (2010b) just considered the equilibrium temperature case which corresponds to the equation (2.76) and Eq (15) refers to equation (2.78). Moreover, Kuiper et al. (2010b) assumes a temperature dependent opacity, which is why a Newton-Raphson is used in the determination of the new temperature distribution, which is of course unnecessary if the opacity is not temperature dependant. The central point of the module is the implicit solver used for the FLD equation. After converting the relevant equation (here: equation (2.78)) to a linear system this system has to be solved. By default, this is done using the GMRES (Generalised minimum residual) method. As Kuiper et al. (2010b) mentions a general linear equation looks like

$$A\mathbf{x} = \mathbf{b}, \quad (3.22)$$

where A is a matrix, \mathbf{x} is the initial vector and \mathbf{b} is the result vector. In the case of an implicit scheme we assume \mathbf{x} to be vector of the advanced time-step and \mathbf{b} to be the initial values. Thus, we need to find the inverse of matrix A and multiply \mathbf{b} by it. Consequently, the equation

$$\mathbf{x} = A^{-1}\mathbf{b} \quad (3.23)$$

is to be solved. The differential equations considered can all be rearranged to a system like that. As an example, see Hans Petter Langtangen (2017) in Subsection 3.2.1. GMRES uses a Krylov subspace method in order to approximately invert this equation under the assumption that A is large but sparse. The choice for GMRES is justified by claiming that it is better than the conjugate gradient method and “at least as good as (...) improved stabilized Bi-Conjugate Gradient” in Kuiper et al. (2010b). Following Kuiper et al. (2010b), the general idea of the GMRES method will be explained. The i -th Krylov subspace K_i is defined as

$$K_i = \text{span} \{ \mathbf{b}, A\mathbf{b}, A^2\mathbf{b}, \dots, A^{i-1}\mathbf{b} \}. \quad (3.24)$$

In each iteration step the Krylov subspace is incremented by one basis vector

$$A^{i-1}\mathbf{b}, \quad (3.25)$$

which “approximates the solution of the system of linear equations by vector \mathbf{x}_i which minimised the normal of the residual $r = |A\mathbf{x}_i|$ ” (Kuiper et al. 2010b). While this method converges monotonically and is predicted to reach the exact solution after the same number of iterations as the number of columns in A , a relative or absolute change abort criterion is used. I.e. the iterations stops when the relative or absolute difference between the current and last iteration goes below a certain threshold. This allows to reach convergence in a few iterations tailored the problem at hand. The background is that, according to Kuiper et al. (2010b), the computation grows as $\mathcal{O}(i^2)$ and thus the iterations should be limited to as few as possible. It should be noted that in the newer

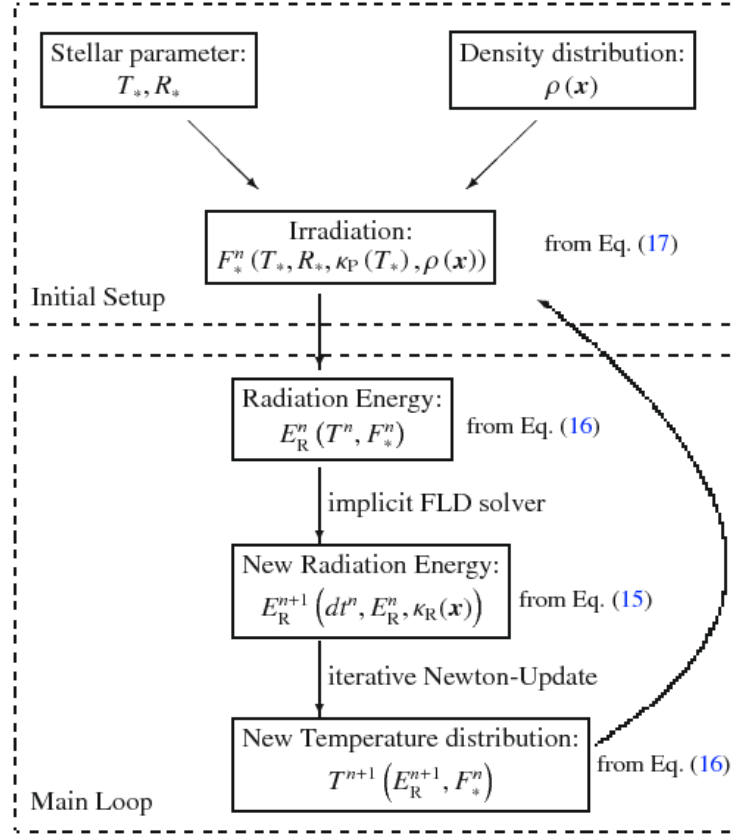


Figure 3.4.: “Schematic flow chart of the radiation module. Exponents declare the iteration (timestep) number n . The actual timestep corresponds to $dt_n = t_n t_{n1}$ ” Kuiper et al. (2010b), also taken from there

versions, in contrast to Kuiper et al. (2010b), the default GMRES solver of PETSC (Balay et al. 2016) is used. Both the solver described in Kuiper et al. (2010b) as well as the current PETSC solver are fully parallelised using MPI and thus can use the already existing MPI framework of PLUTO. For more detailed tests of the module see Kuiper et al. (2010b) and Kuiper et al. (2018, submitted).

3.2.6.2. “Haumea” (self-gravity)

The “Haumea” module is responsible for supplying the value for Φ_{Gas} derived from the density distribution. Kuiper et al. (2010a) describes that a diffusion Ansatz is used in order to solve the Poisson equation. Again, the resulting linear system from the implicit time-discretisation is solved using the GMRES (Generalised minimum residual) method as explained in the “Makemake” subsection. The result is now Φ_{Gas} . The accuracy, “i.e. the abort criterion for the approximate matrix inversion” can be set as a relative or absolute value as in “Makemake”. There are several options for the boundary conditions. Kuiper et al. (2010a) only describes one method, akin

to Black and Bodenheimer (1975), a Taylor expansion of the density distribution to the boundary. From this only the monopole is used, as tests in Kuiper et al. (2010a) revealed that this is sufficient. However, we employ a newer version of the module in this thesis which allows to use other boundary conditions and other solvers and preconditioners. As it is later used, one of the new boundary condition choices is explained here. It is possible to rely on an explicit method that determines the profile at the boundary now. As this is quite computation intensive we calculate these values for the initial conditions and use them throughout the simulation. More information on the boundary conditions can be found in Subsection 3.3.4. As with “Makemake” the newer version also allows a selection of other solvers and preconditioners. More application examples can be found in Kuiper et al. (2011).

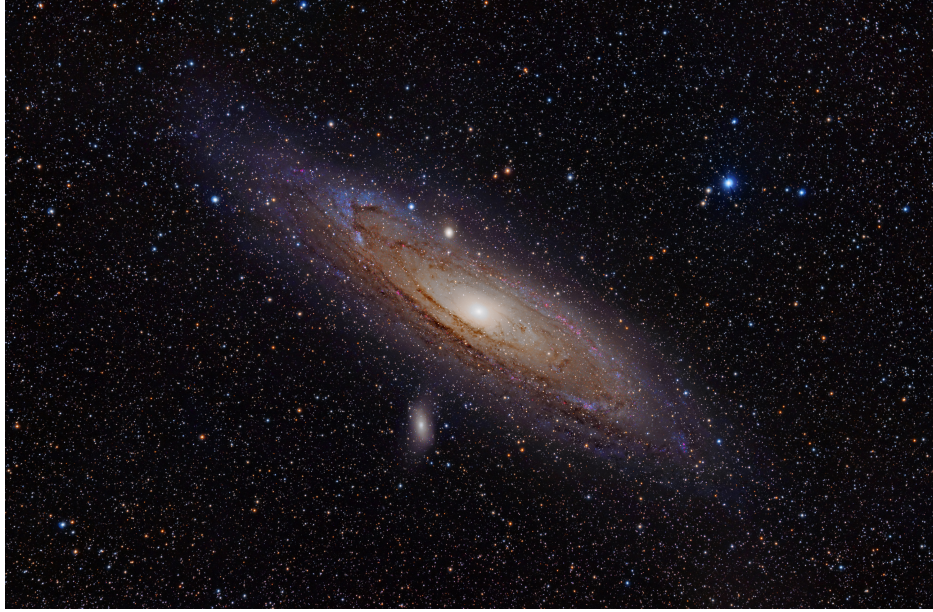


Figure 3.5.: Picture of M31 including H- α . Source: Evans (2010)

3.3. Set-up

3.3.1. Target system

In order to be able to compare the results to the ones from Kennedy et al. (2016), we have chosen M31 as the system we will simulate in this thesis. For a visual representation we give Fig. 3.5). Thus, we choose all parameters for the system as displayed in Kennedy et al. (2016). Consequently, the parameters

$$M_{\text{BH}} = 1.5 \times 10^8 M_{\odot}, \quad r_{\text{inf}} = R_{\text{d}} = 25 \text{ pc} \quad (3.26)$$

are employed. Additionally, we also assume $M_{\text{d}} = 0.1 M_{\text{BH}}$ and $h_z = 1.0 \times 10^{-3}$ as in Just et al. (2012), Kennedy et al. (2016). Furthermore, the calculations in Kennedy et al. (2016) (for more details see Subsubsection 3.4.2.4) arrive at

$$\dot{M}_{\text{BH}}(\text{gas}) = 2.0 \times 10^{-2} M_{\odot} \text{ yrs}^{-1} \quad (3.27)$$

for the accretion rate. Because of the different definitions of α as described in equation (2.159) we calculate the value corresponding to $\alpha_{\text{K10}} = 2.0 \times 10^{-1}$. The result is

$$\dot{M}_{\text{BH}}(\text{gas}, K10) \approx 2.85 \times 10^{-2} M_{\odot} \text{ yrs}^{-1}. \quad (3.28)$$

We can later compare this to the integrated radial mass flow in the simulation.

3.3.2. Parameters resulting from the chosen system

In order to stay as close as possible to Kennedy et al. (2016) we choose $\beta = -\frac{3}{4}$. Following equation (2.143), we can determine

$$R_{\text{SG}} = (0.008)^{\frac{4}{9}} R_{\text{d}} \approx 2.924 \text{ pc} \quad (3.29)$$

along with

$$\frac{h}{R} = (0.008)^{-\frac{4}{9}} h_z R_{\text{d}} \approx 8.46 \times 10^{-3}. \quad (3.30)$$

The radius at which $Q_{\text{Toomre}} = 1$, as shown in equation (2.177), is given by

$$R_{Q_{\text{Toomre}}=1} \approx 5.05 \text{ pc}. \quad (3.31)$$

In order to have a measure for the closeness to the Super Massive Black Hole (SMBH) we calculate the Schwarzschild radius

$$R_{\text{SW}} = \frac{2GM_{\text{BH}}}{c^2} \approx 1.4355 \times 10^{-5} \text{ pc}. \quad (3.32)$$

For the radial range we choose $r \in [0.11 \text{ pc}, 25 \text{ pc}]$ and thus our closest distance to the SMBH is $\approx 7663 R_{\text{SW}}$. This clearly means that we can use Newtonian physics. We also set a lower density threshold, i.e.

$$\rho_{\text{initial}} = \sqrt{\rho^2 + \rho_{\text{min}}^2}. \quad (3.33)$$

We choose $\rho_{\text{min}} = 1 \times 10^{-23} \text{ g cm}^{-3}$ as the very low density regions below this threshold, rather part of the disk's atmosphere, are not expected to contribute much to any physical effects in the system. Moreover, the numerical calculations on computational systems would be error-prone because of the range of different orders of magnitudes involved in calculations with low density. Consequently, the regions where $\rho_{\text{initial}} \leq \rho_{\text{min}}$ are ignored in the numerical calculation. The reason is their little importance as well as the high risk of shocks appearing in very low density regions. We simulate $\pm 5^\circ$ over the equatorial plane in θ and use a lower radial limit 0.11 pc. I.e. the total ranges are

$$r \in [0.11 \text{ pc}, 25.0 \text{ pc}] \quad (3.34)$$

$$\theta \in \left[\frac{\pi}{2} - \frac{\pi}{36}, \frac{\pi}{2} + \frac{\pi}{36} \right] \quad (3.35)$$

$$\varphi \in [0, 2\pi]. \quad (3.36)$$

3.3.3. Units

For the basic units in the computation we choose

$$[l] \quad 1 \text{ pc} \approx 3.085677 \times 10^{18} \text{ cm}$$

3. Numerical simulations using the PLUTO code and NBODY6++GPU

$$[\rho] 1.0 \times 10^{-15} \text{ g cm}^{-3}$$

$$[v] \frac{1 \text{ pcc}}{t_{\text{ly}}} \approx 9.778 \times 10^5 \text{ km s}^{-1}.$$

Using this, we can derive more units for the problem.

$$[t] \frac{[l]}{[v]} \approx 1.471 405 \times 10^{13} \text{ s} \hat{=} 1.001 \text{ yrs}$$

$$[p] 9.561 \times 10^6 \frac{\text{dyn}}{\text{cm}^2}.$$

3.3.4. Boundary conditions

As for any numerical simulation of partial differential conditions, boundary conditions need to be specified in order to be able to determine approximate solutions. In our current case we need boundary conditions for the hydrodynamic quantities used in PLUTO. There are ρ, p, v_r, v_θ and v_φ , the radiation energy density from the “Make-make” module as well as the self-gravity potential Φ “Haumea”. Boundary conditions must be defined for all three coordinate dimensions i.e. r, θ and φ in our case. PLUTO always dubs the three coordinate dimensions as $X1, X2$ and $X3$. In the PLUTO code, two boundary cells are created per dimension. Fig. 3.6 illustrates all of this for a 2-dimensional Cartesian grid, where four inner cells were requested for each dimension. The first number in each cell represent their coordinate index of the first dimension, whereas the second is the same for the second dimension. One can clearly see that the boundary zones have overlapping parts and that, apart from the 16 internal cells, 48 boundary cells are created. In three dimensions as well as for curvilinear coordinates all of this works analogously. The PLUTO code defines $IBEG$ as the last coordinate before the inner boundary for the $X1$ coordinate and $IEND$ as the last index before the outer boundary for the $X1$ coordinate. Similar definitions apply for the $X2$ and $X3$ directions. For these the letter J and K are used, respectively. The numbers $NX1, NX2$ and $NX3$ describe the number of internal grid cells (excluding the boundaries) in the i, j and k direction, respectively. $NX1.TOT$ (similar for the other directions) is defined as the total number of grid points including the boundary cells. In this example $IBEG = 2, IEND = 5, JBEG = 2, JEND = 5, NX1 = 4, NX2 = 4, NX1.TOT = 8$ and $NX2.TOT = 8$.

3.3.4.1. Hydrodynamic quantities

As we have a closed circle in φ , periodic boundary conditions are assigned for all quantities i.e. when taking the $X3$ boundary as an example

$$q_{i,j,k} = \begin{cases} q_{i+NX3,j,k} & \text{if at the inner boundary} \\ q_{i-NX3,j,k} & \text{if at the outer boundary} \end{cases}, \quad (3.37)$$

where i is an index running within the $X1$ boundary zone. This means, $i = IBEG - 1$ or $IBEG - 2$ is valid at the inner boundary, whereas $i = IEND + 1$ or $IEND + 2$

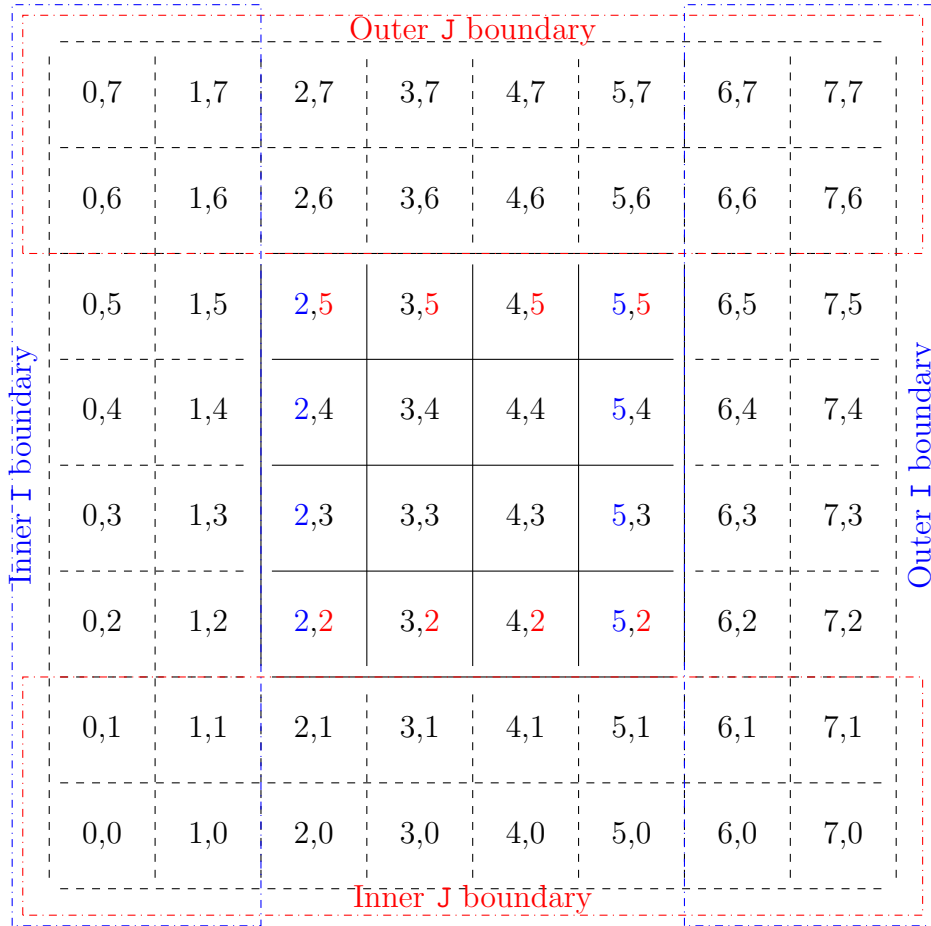


Figure 3.6.: This figure represents a 2-dimensional grid including the boundaries as created by PLUTO when using Cartesian coordinates requesting four inner cells in each direction. The colourcoding (**i boundary**, **j boundary**) shows the last inner cells for the corresponding direction. The coloured boxes show the relevant boundary sections showcasing that they are overlapping to some degree, inspired by Fig. 4.2 in the PLUTO userguide

is valid at the outer boundary. In contrast, j and k are indices running in the entire domain and boundaries of the other directions ($X2, X3$). Lastly, q is one of the quantities $\rho, p, v_r, v_\theta, v_\varphi, \Phi, E_{\text{rad}}$. In the r direction we enforce a zero gradient for the pressure p

$$\frac{\partial p}{\partial n_r} = 0. \quad (3.38)$$

Opposed to this, a conditional boundary condition is employed for ρ and v_r

$$\rho: \begin{cases} \frac{\partial \rho}{\partial n r} = 0 & \text{if } v_r \leq 0 \\ \rho(r_i, \theta, \varphi) = \rho(r_{2I-i\pm 1}, \theta, \varphi) & \text{else} \end{cases}, \quad (3.39)$$

$$v_r: \begin{cases} \frac{\partial v_r}{\partial n r} = 0 & \text{if } v_r \leq 0 \\ v_r(r_I, \theta, \varphi) = -v_r(r_{2I-i\pm 1}, \theta, \varphi) & \text{else} \end{cases}. \quad (3.40)$$

Finally, we ensure a Keplerian gradient toward the computational domain for v_φ

$$v_\varphi(r_i, \theta, \varphi) = \min \left\{ v_K(r_i, \theta), v_{\varphi, \text{old}}(r_i, \theta, \varphi) \sqrt{\frac{r_I}{r_i}} \right\}. \quad (3.41)$$

In these equations, n is the boundary plane direction normal, I is the index of the first cell of the upper or lower boundary (i.e. $IBEG - 1/IEEND + 1$), \pm is $+$ for the lower boundary and $-$ for the upper boundary respectively, i is index of the current boundary cell in the boundary, $v_{\varphi, \text{old}}$ is the v_φ velocity prior to the boundary assignment, $v_K^2(r_i, \theta) = \frac{GM_{\text{BH}}}{r_i \cos \theta}$ and $\min\{\}$ is the minimum of its two arguments. One can see that the pressure is always assigned a zero gradient boundary condition, whereas ρ is only assigned that if the v_r velocity is non-negative. Otherwise, a reflective boundary condition is assigned for ρ . The same condition is applied to the velocity v_r . The underlying reason is that one needs to prevent an inflow back into the computational domain. On top of that, v_φ is changed such that a gradient towards the computational domain is created. The same mechanism is applied to the θ -boundary $X2$, expect that instead of v_r , v_θ is considered

$$\frac{\partial p}{\partial n \theta} = 0 \quad (3.42)$$

$$\rho: \begin{cases} \frac{\partial \rho}{\partial n \theta} = 0 & \text{if } v_\theta \leq 0 \\ \rho(r, \theta_j, \varphi) = \rho(r, \theta_{2J-j\pm 1}, \varphi) & \text{else} \end{cases} \quad (3.43)$$

$$v_\theta: \begin{cases} \frac{\partial v_\theta}{\partial n \theta} = 0 & \text{if } v_\theta \leq 0 \\ v_\theta(r, \theta_j, \varphi) = -v_\theta(r_{2J-j\pm 1}, \theta, \varphi) & \text{else} \end{cases} \quad (3.44)$$

$$v_\varphi(r, \theta_j, \varphi) = \text{Min} \left\{ v_K(r, \theta_j), v_{\varphi, \text{old}}(r, \theta_j, \varphi) \sqrt{\frac{\theta_J}{\theta_j}} \right\}. \quad (3.45)$$

In these expressions, J is the first cell the upper or lower θ boundary (i.e. $JBEG - 1/JEND + 1$), j is the current index within the θ boundary.

3.3.4.2. E_{rad}

For E_{rad} we assign a zero gradient boundary condition (No radiative flux over boundary interface) for the lower r boundary. For the upper r boundary as well as both θ boundaries we assign the temperature values prescribed via the initial conditions in

the corresponding cell as

$$E_{\text{rad}} = a_{\text{rad}} T_{\text{initial}}^4, \quad (3.46)$$

where $T_{\text{initial}}^4 = p_{\text{initial}} \frac{\mu m_{\text{H}}}{k_{\text{B}} \rho_{\text{initial}}}$, $\mu = 0.7$, k_{B} is Boltzmann's constant and m_{H} is the hydrogen atom mass. In the φ -direction periodic boundary conditions are prescribed once more.

3.3.4.3. Self-gravity potential Φ

As the last point, the boundary conditions for the self-gravity potential Φ are discussed. For the radial boundaries we prescribe a zero-gradient condition again. Also, periodic boundary conditions are again assigned to φ . For the θ boundaries we assign the explicitly calculated values from the initial condition, i.e. the explicit solution for the Poisson equation

$$\Delta \Phi_{\text{Gas}} = -4\pi G \rho_{\text{initial}} \quad (3.47)$$

at the boundary derived from the initial density profile.

3.4. Numerical simulations without self-gravity

As first tests we performed simulations that do not include self-gravity. Thus, these simulations get a smaller radial range which stops at the radius R_{SG} , describing the break even point between central Super Massive Black Hole (SMBH) gravity and self-gravity. Both axis-symmetric 2D simulations as well as full-scale 3D simulations were performed.

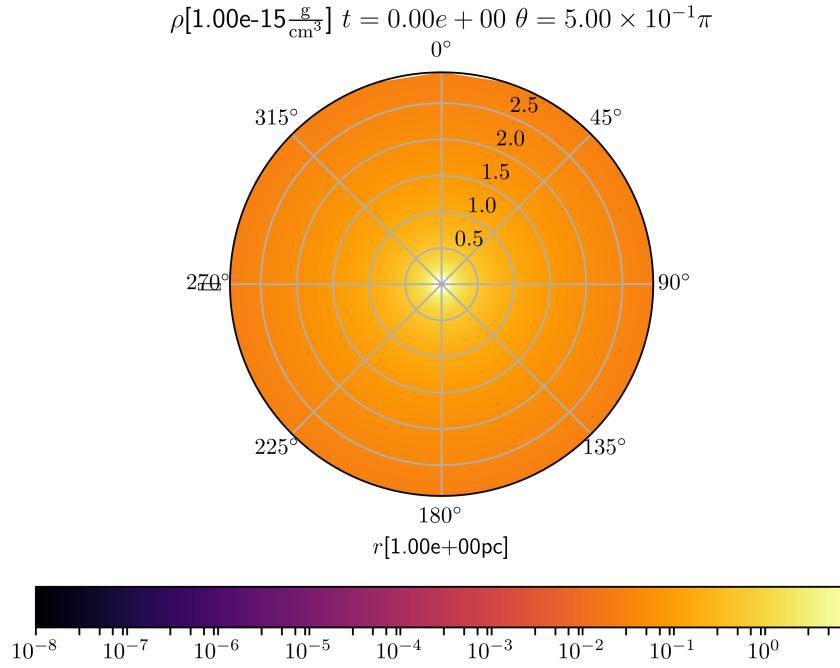
3.4.1. Initial conditions

We prescribe the before mentioned initial conditions. This results in the density, total pressure and φ profiles (Reminder: v_r and v_θ were initialised to 0) as displayed in Fig. 3.7, Fig. 3.8 and Fig. 3.9. These illustrate that the initial conditions are independent of φ and symmetric in $\cos\theta$ and that we are covering five orders of magnitude in ρ and p and two in v_φ . Moreover, the lower density threshold, and its effect on the pressure profile, can be seen in the plots of the density and pressure profile (blue lines in Fig. 3.8 denotating where the minimum density begins, flattening profiles in Fig. 3.9a and Fig. 3.9b).

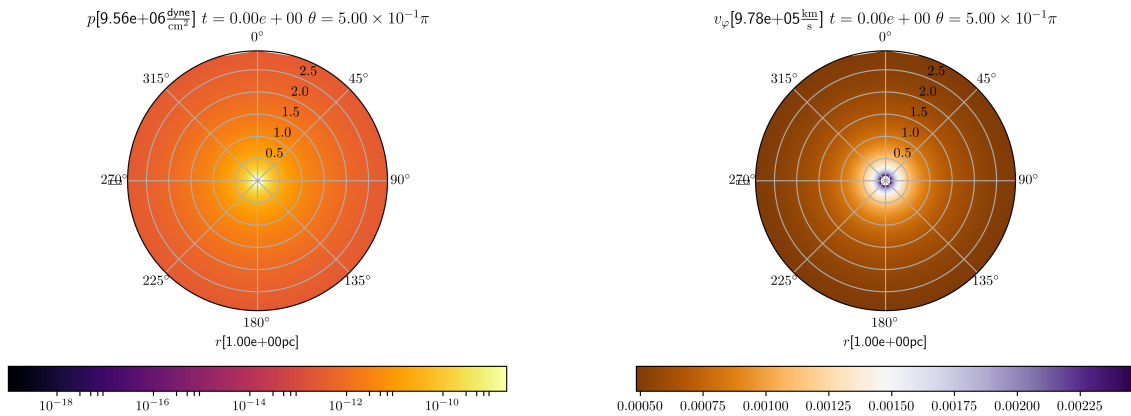
3.4.2. Results in axis-symmetric 2D simulations

Initially, axis-symmetric simulations were performed. The initial conditions are, of course, the same as for a 3D simulation as there is no φ dependence. The pressure mostly follows the density (as visible in the initial conditions) and there is no significant change in v_φ as to be seen in Fig. 3.10 (Dashed line: initial conditions overlap with current values). Consequently, these quantities are not discussed in the following. In the Fig. 3.11a and Fig. 3.12a show that there are small oscillations in the density representing waves passing through the system that are dissipating over time. Fig. 3.12a specifically shows that the oscillations are bigger further away from the equatorial plane. This behaviour is mirrored in the radial velocity v_r as visible in Fig. 3.11b and Fig. 3.12b which are displaying the same wave patterns. Below $r = 3 \times 10^{-1}$ pc no oscillations are present proven best by Fig. 3.12b. Additionally, v_r is almost zero in the equatorial plane and only shows oscillations. Moreover, there is a spike to zero close to the inner boundary which is most probably a boundary condition effect, which is not physical. For the θ values much above/below the equatorial plane one can see we see the same jump near the inner boundary and oscillations. However, they clearly have negative values with a downward slope up to the jump. All of this can be a sign that the system is equilibrating. As can be seen in Fig. 3.11c and Fig. 3.12c the v_θ velocity is almost zero in the inner high density parts of the disk and only have a non-zero value in the regions above and below that region. A shock behaviour can be observed there which creates material falling onto the disk from both vertical directions. This seems to be already a quite constant state.

3.4. Numerical simulations without self-gravity



(a) ρ

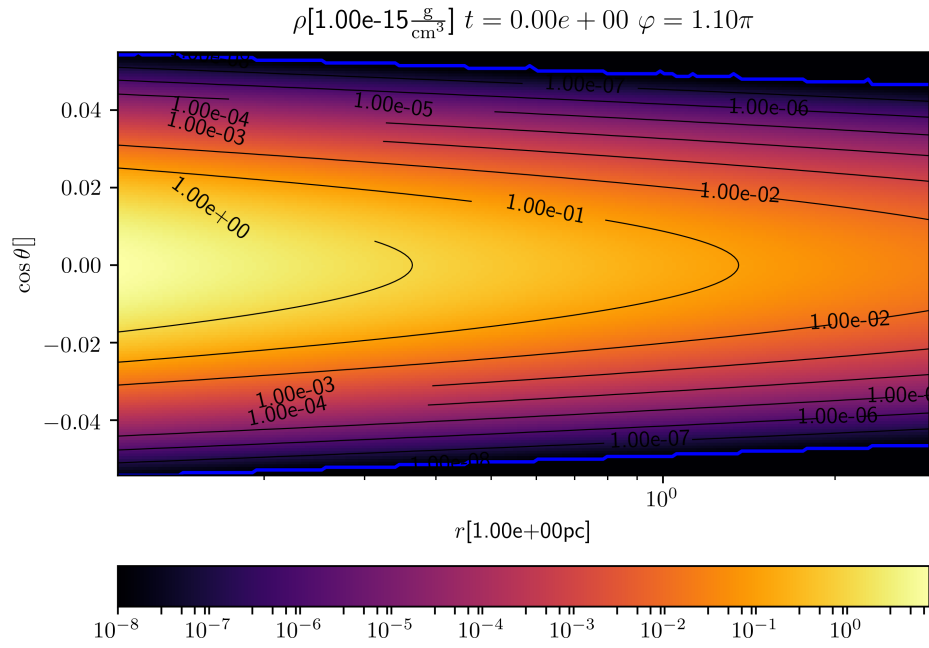


(b) p_{tot}

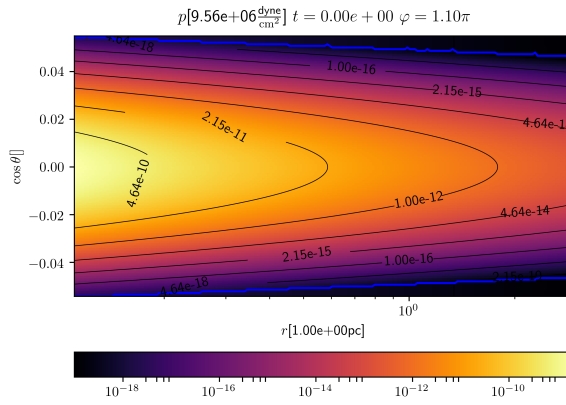
(c) v_φ

Figure 3.7.: Initial conditions without self-gravity showing the equatorial plane (i.e. cut in θ) emphasising the axis-symmetry of the initial conditions

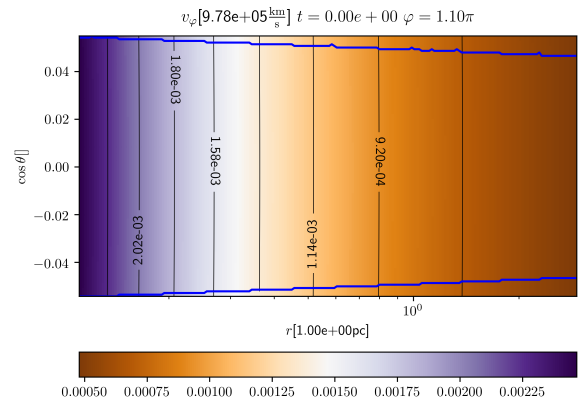
3. Numerical simulations using the PLUTO code and NBODY6++GPU



(a) ρ



(b) p_{tot}



(c) v_φ

Figure 3.8.: Initial conditions without self-gravity showing a cut in θ and φ

3.4. Numerical simulations without self-gravity

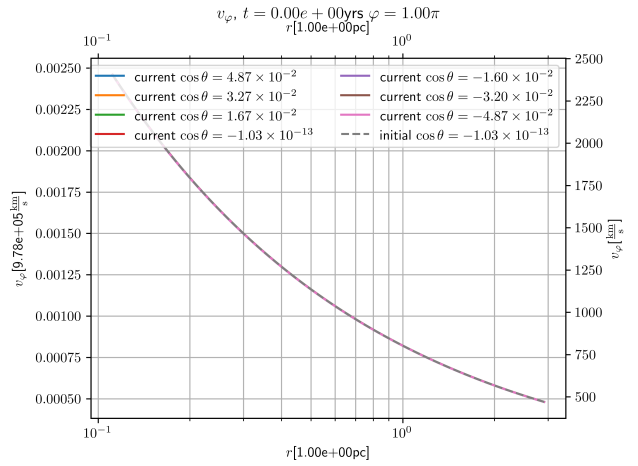
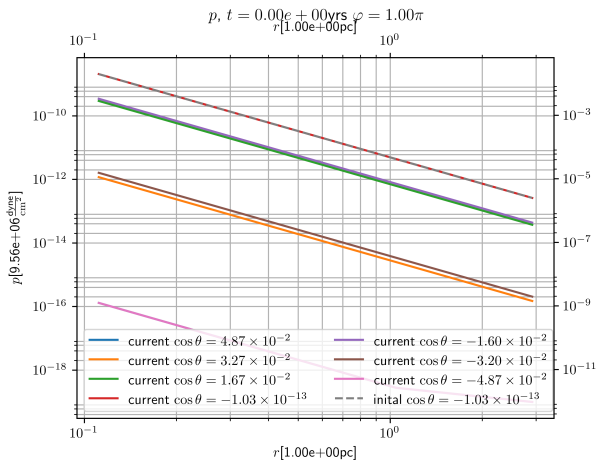
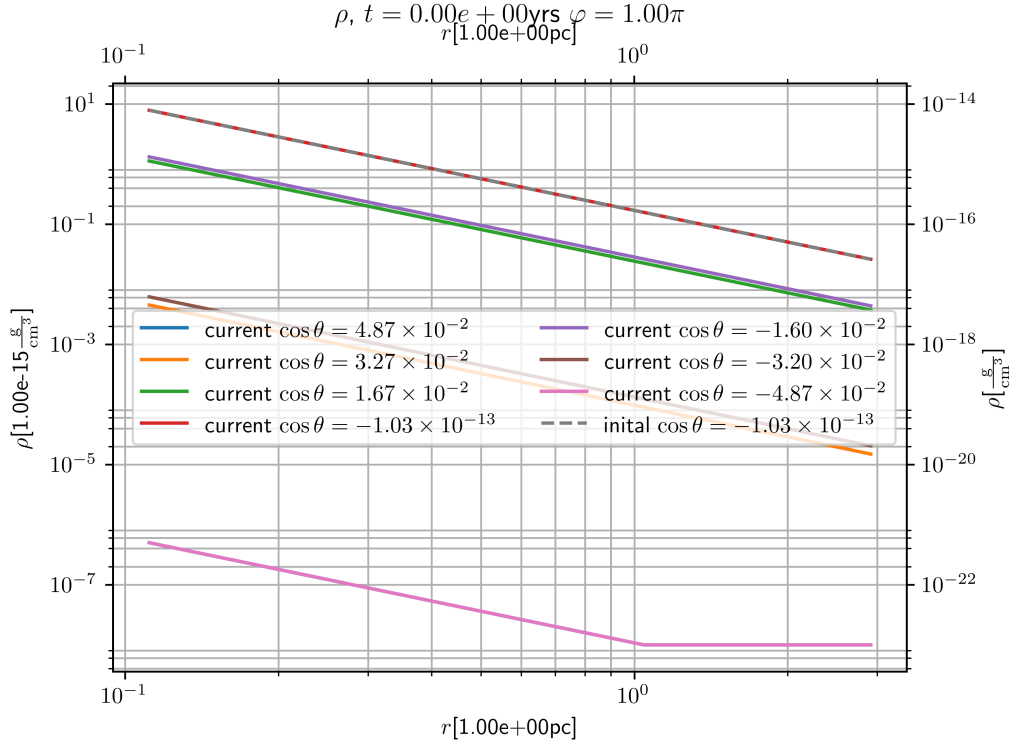


Figure 3.9.: Initial conditions without self-gravity showing showing 1D plots showcasing r dependence with several θ values

3.4.2.1. Equilibrated state

After $\approx 8.0 \times 10^4$ yrs the system is equilibrated and the simulation was continued until 1.0×10^7 yrs. The plots can be seen in Fig. 3.13 and Fig. 3.14. All oscillations have disappeared, we only see a slight decrease in the density near the inner boundary (see Fig. 3.14a) which is also a boundary condition effect. The radial velocity (see Fig. 3.14b) is also oscillation free and only shows jumps at the inner and outer boundary. v_θ (see Fig. 3.14c) also shows no more oscillations and is still essentially zero except for cells much above the equatorial plane.

3.4.2.2. Analysis of the scale-height

In order to determine potential changes in the constant $\frac{h}{R}$ (as described in Subsection 2.3.7) we fit the function

$$\rho(r, z) = \rho_0(r) \exp\left(-\frac{z^2}{2h^2}\right) \quad (3.48)$$

at every radius r , where $\rho_0(r)$ is the density of the equatorial plane which can be obtained as the density of each of the cells of the equatorial plane and $z = r \cos \theta$ is the Cartesian height coordinate. From this we can obtain $h(R)$ (as $r = R$ in the equatorial plane) and $\frac{h}{R}$. The result can be seen in Fig. 3.15 which shows that the factor has stayed constant, but dropped from its initial value $\frac{h}{R_{i0}} \approx 8.46 \times 10^{-3}$ to

$$\frac{h}{R} \approx 6.60 \times 10^{-3}. \quad (3.49)$$

This means the disk's aspect ratio $\frac{h}{R}$ has dropped by $\approx 21\%$ i.e. the disk has become thinner in the equilibration process. However, it has done so in the same way over the whole r range emphasising that a linear growing scale-height is the correct equilibrated state. The slightly different value might be related to the fact that the initially prescribed value for $\frac{h}{R}$ is derived from an approximation.

3.4.2.3. Analysis of the radial velocity

Furthermore, we can take a closer look on the radial velocity v_r . Shakura and Sunyaev (1973) predict a power law for the radial velocity

$$v_r = aR^l, \quad (3.50)$$

where a is a constant (that also depends on more parameters of the system such as α) and l is a real number. Following Kennedy et al. (2016) we look at the region c) in Shakura and Sunyaev (1973) which has $l = -\frac{1}{4}$. When fitting the power law to the data (i.e. to each $v_r(r)$ for each θ) we obtain the results displayed in Fig. 3.16. It should be noted that both values were set to zero if no convergence of the fit could not converge. As Fig. 3.16a reveals we generally see 0 on the boundaries (part of the

3.4. Numerical simulations without self-gravity

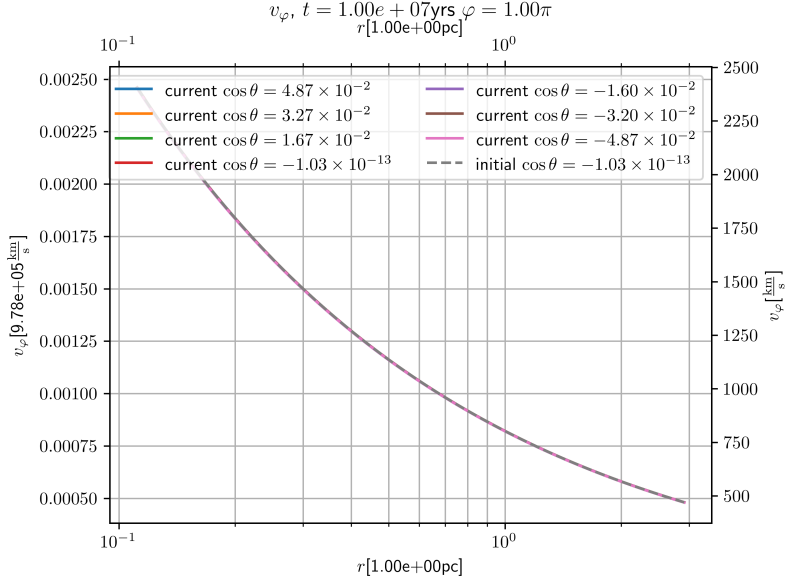
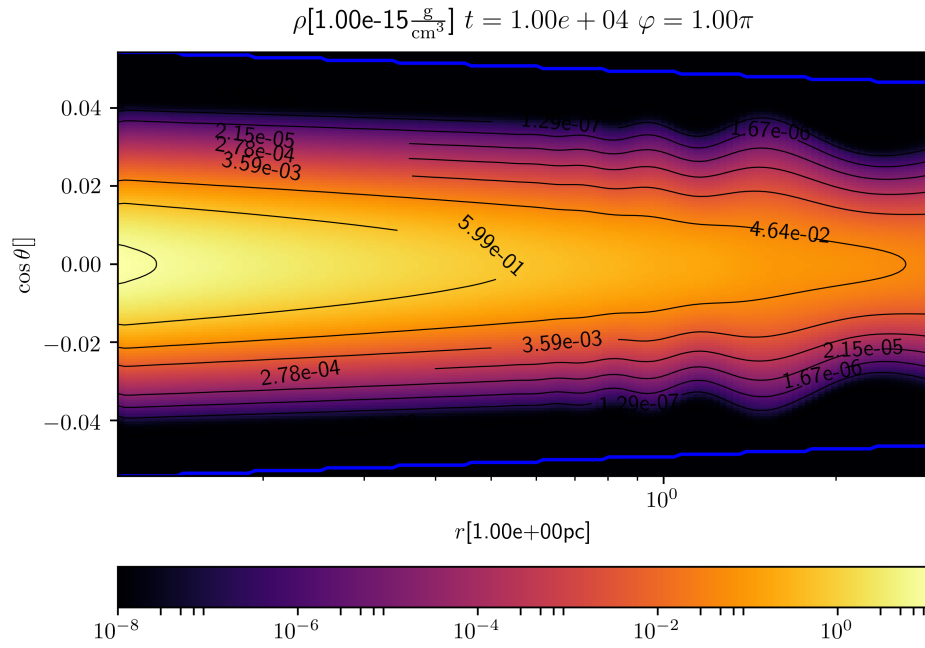


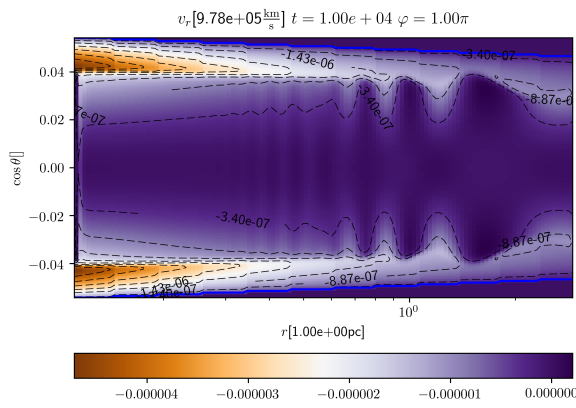
Figure 3.10.: v_ϕ after 1.0×10^7 yrs from a 2D simulation with $\alpha_{K10} = 2.0 \times 10^{-1}$, the dashed line are the initial conditions

not integrated domain) and no clear conclusion in the equatorial plane. There is a pronounced global minimum a bit before $\cos \theta = -0.05$. We unfortunately only partly observe the predicted clear dependence of the constant a on the α parameter. One can see, however, see a much more steep decline for $\alpha_{K10} = 4.0 \times 10^{-1}$ and 2.0×10^{-1} as well as lower absolute magnitude of the minimum. A closer look at Fig. 3.16b confirms that there was no convergent result for the equatorial plane as $p = 0$ is valid in it for all α apart from $\alpha_{K10} = 5.0 \times 10^{-2}$. Strangely, there are positive p values in a local maximum for all α . Otherwise we get a negative p which are close to $p = -1$ and are going down to $p = -4$. While the negative sign is expected, this is at least four times higher than the predicted $p = -0.25$. However, the value is closer to the other values of the other subregions from Shakura and Sunyaev (1973) ($-\frac{1}{5}$ and -1.5). Apart from $\alpha_{K10} = 1.0 \times 10^{-2}$ the p values are very similar in their constant regions which should be the case. It is unclear why it is different for one α_{K10} value. When looking at the qualitative plots in Fig. 3.17 we can see that the reason of the strange behaviour of $\alpha_{K10} = 1.0 \times 10^{-2}$ is probably due to the higher oscillations still present in it. Furthermore, one sees that the radial velocity is higher in regions above the equatorial plane and that one can see a larger negative value for v_r for higher α . The lowest oscillations are to be seen for $\alpha_{K10} = 2.0 \times 10^{-1}$ followed closely by $\alpha_{K10} = 5.0 \times 10^{-2}$. While higher viscosity should mean lesser oscillations in general we cannot see this here. The system seems to have specific α values which result in a oscillation free-simulation in v_r after equilibration. It might be that the self-gravity is a factor for this. Thus, we will revisit this again later.

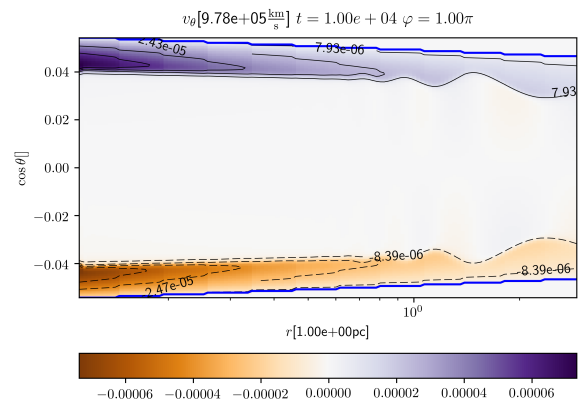
3. Numerical simulations using the PLUTO code and NBODY6++GPU



(a) ρ



(b) v_r



(c) v_θ

Figure 3.11.: 2D Plots of ρ , v_r and v_θ after 1.0×10^4 yrs from a 2D simulation with $\alpha_{K10} = 2.0 \times 10^{-1}$

3.4. Numerical simulations without self-gravity

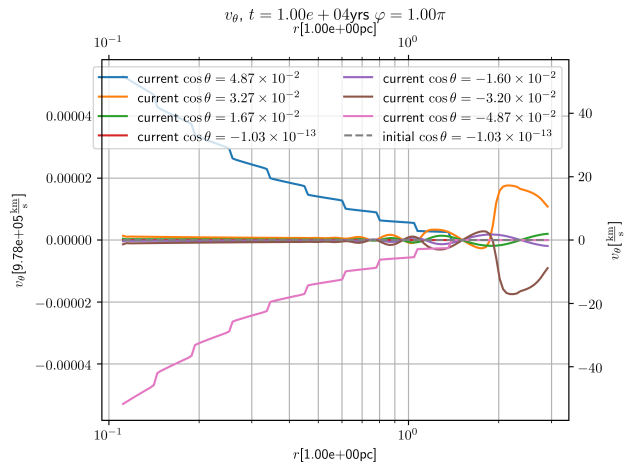
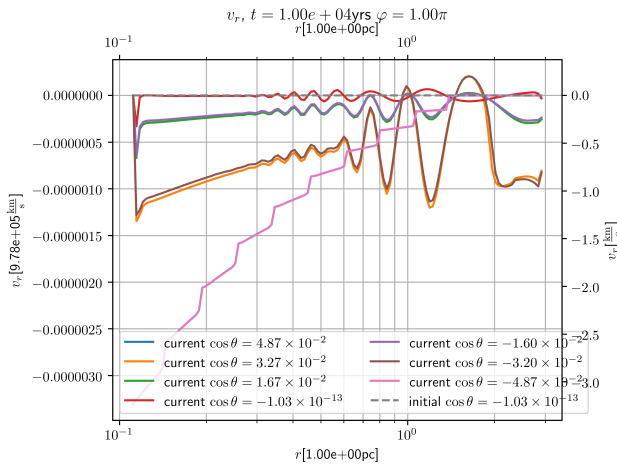
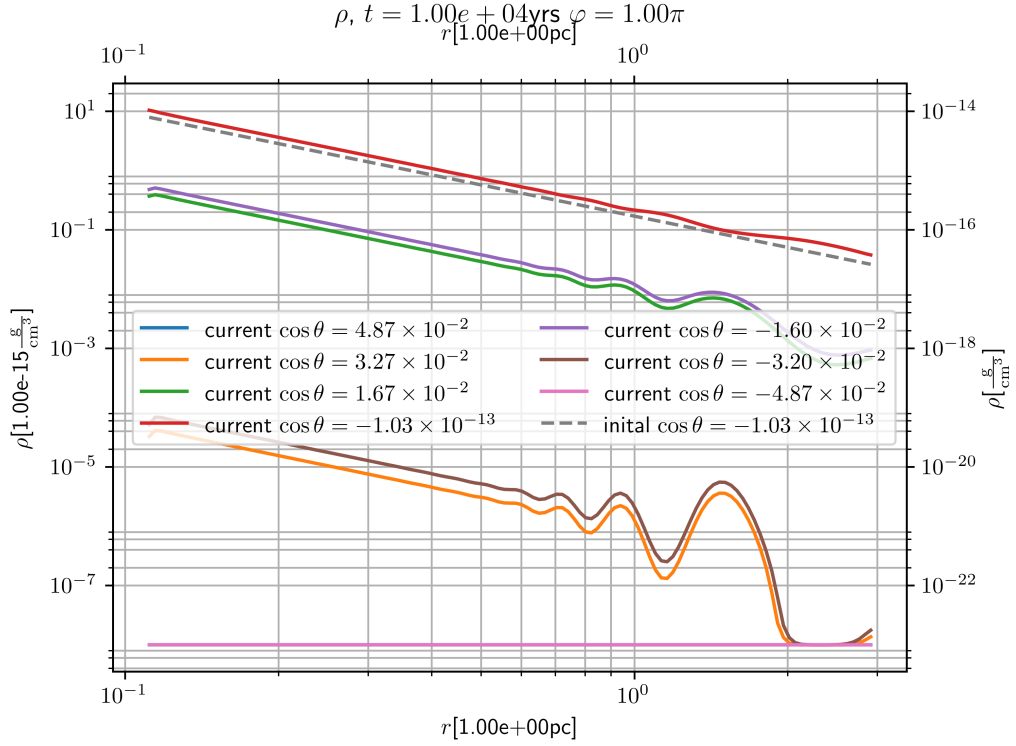


Figure 3.12.: 1D Plots of ρ , v_r and v_θ after 1.0×10^4 yrs from a 2D simulation with $\alpha_{K10} = 2.0 \times 10^{-1}$

3.4. Numerical simulations without self-gravity

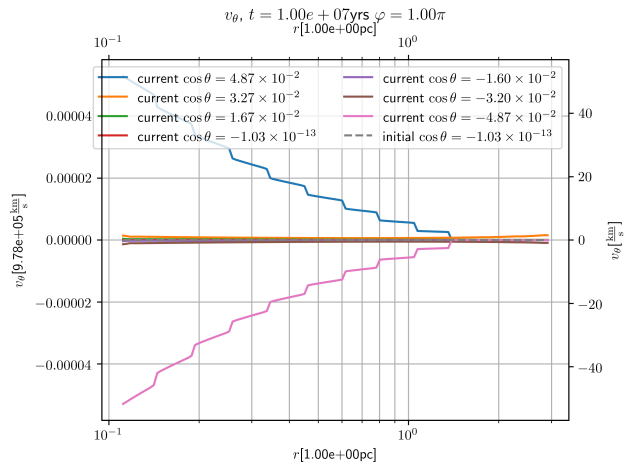
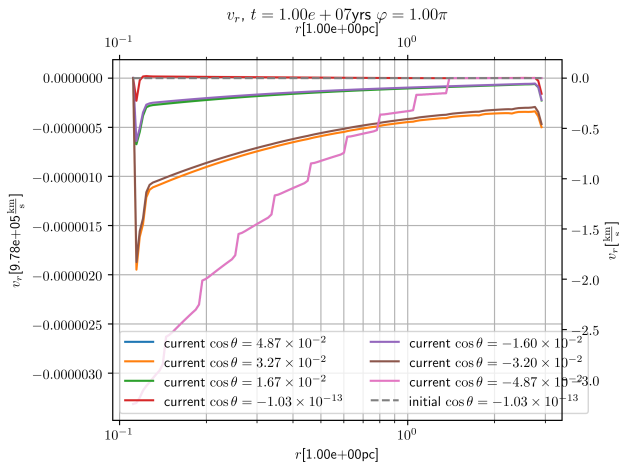
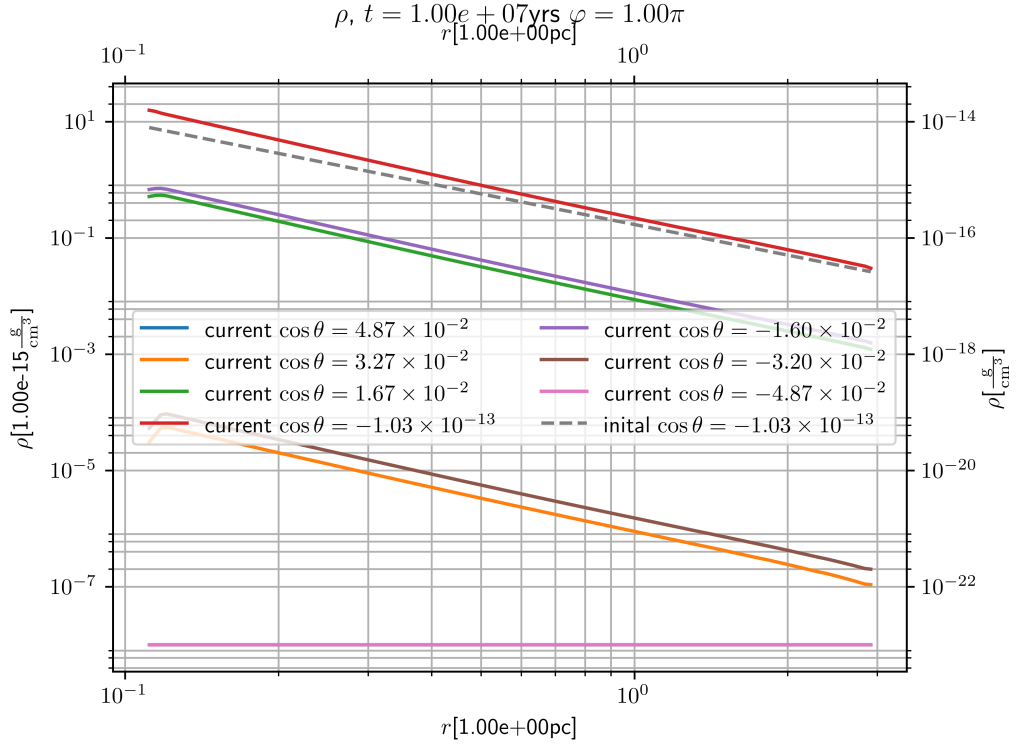


Figure 3.14.: 1D Plots of ρ , v_r and v_θ after 1.0×10^7 yrs from a 2D simulation with $\alpha_{K10} = 2.0 \times 10^{-1}$

3. Numerical simulations using the PLUTO code and NBODY6++GPU

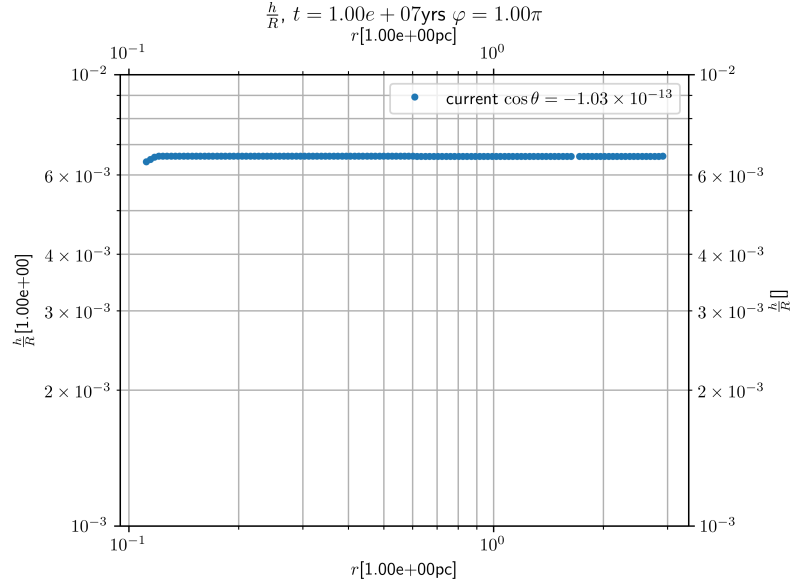


Figure 3.15.: $\frac{h}{R}$ at each radius r after 1.0×10^7 yrs obtained from a 2D simulation with $\alpha_{K10} = 2.0 \times 10^{-1}$

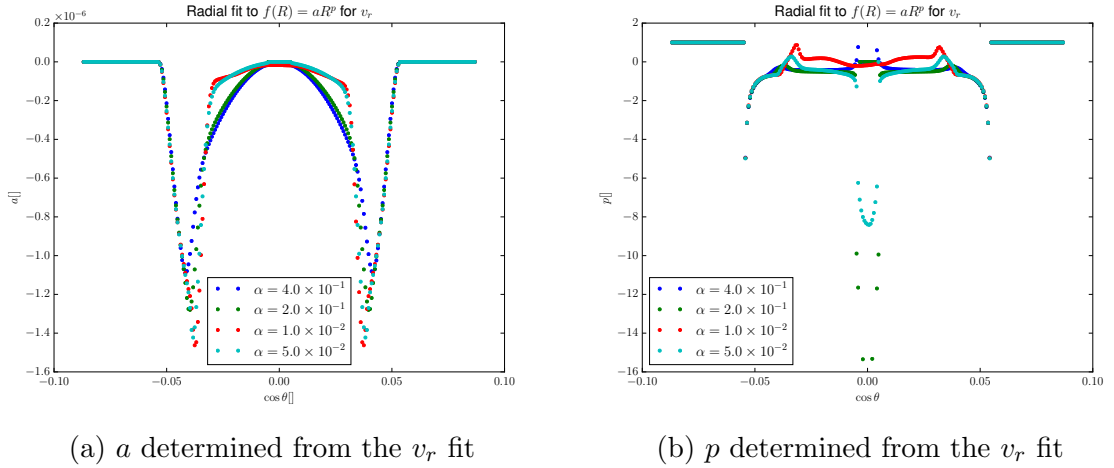


Figure 3.16.: Plots of the power law $f(R) = aR^p$ fitting parameters for v_r for different values of α determined from a 2D simulation without self-gravity, be aware that there is no unit stated for a as it depends on the value of p

3.4. Numerical simulations without self-gravity

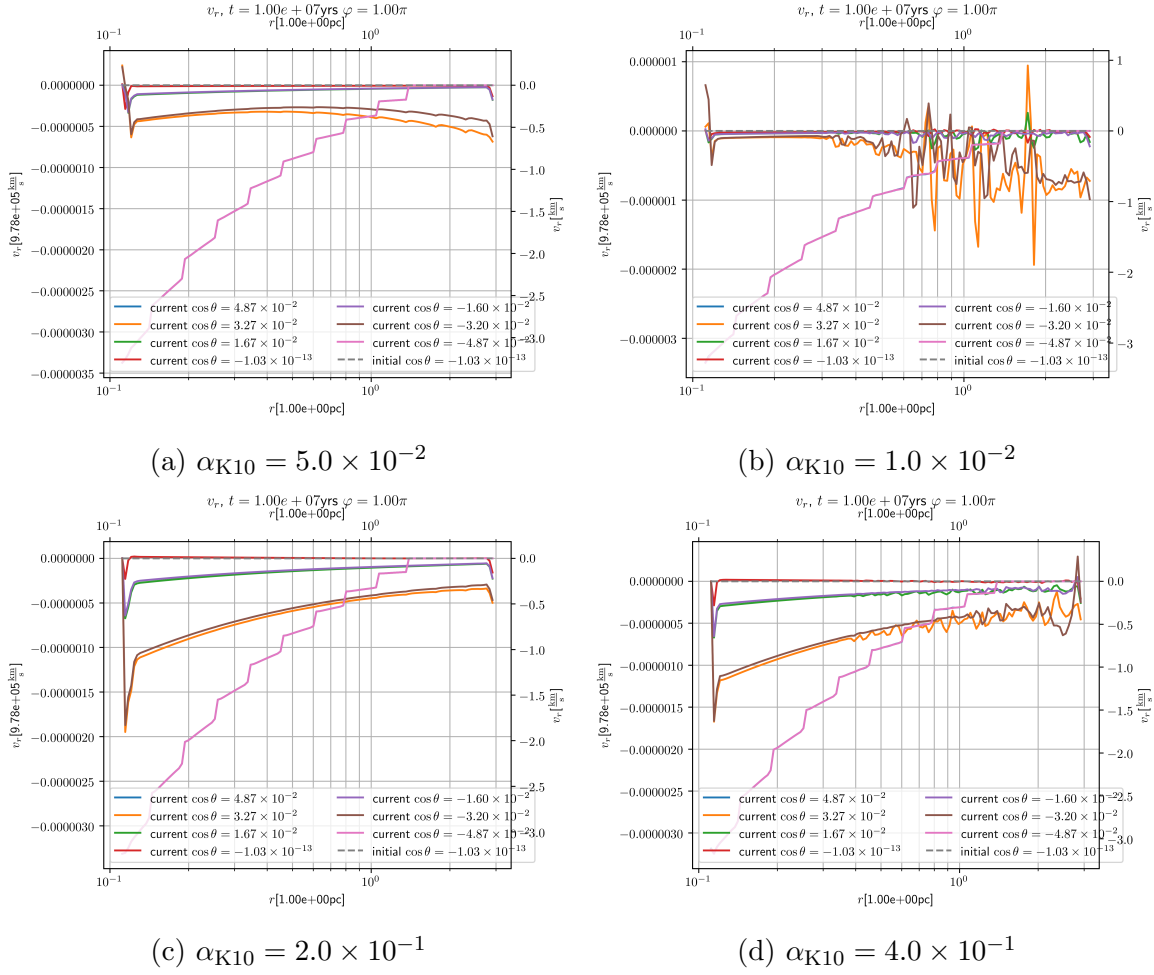


Figure 3.17.: Plots of v_r for a variety of θ values derived from 2D simulation without self-gravity for four different values of α_{K10} after 1.0×10^7 yrs

3.4.2.4. Analysis of the radial mass flow as a precursor for the accretion rate

In the next step we take a look at the integrated radial mass flow as a precursor for the accretion rate i.e. the result of the calculation

$$\dot{m}_r = \int \rho v_r dA \quad (3.51)$$

for each radius r , where A is the spherical surface corresponding to the radius. As already suggested by the notation we are using this as a approximation for the accretion rate which is constant in Shakura and Sunyaev (1973). It can be calculated from the other input parameters and profiles as given in Shakura and Sunyaev (1973). Kennedy et al. (2016) uses equation 2.19 from Shakura and Sunyaev (1973) to arrive at

$$\dot{M} = 1.8 \times 10^{-6} M_{\odot} \text{ yrs}^{-1} \alpha^{\frac{8}{7}} \left(\frac{M_d}{M_{\odot}} \right)^{\frac{10}{7}} \left(\frac{M_{\text{BH}}}{M_{\odot}} \right)^{-\frac{5}{14}} \left(\frac{R_d}{R_{\odot}} \right)^{-\frac{25}{14}} \quad (3.52)$$

which gives, for our choice $M_{\text{BH}} = 1.5 \times 10^8 M_{\odot}$, $M_d = 0.1 M_{\text{BH}}$ and $\alpha = 2.0 \times 10^{-1}$, $\dot{M} \approx 2.0 \times 10^{-2} M_{\odot} \text{ yrs}^{-1}$. As mentioned before the different α definitions means that the simulations should have a value of $\dot{M} \approx 2.85 \times 10^{-2} M_{\odot} \text{ yrs}^{-1}$. When plotting the values obtained from the simulations we obtain the results displayed in Fig. 3.18. At first glance one can see that there are great oscillations for higher radii for $\alpha_{\text{K10}} = 1.0 \times 10^{-2}$ and 4.0×10^{-1} , whereas the curves are really smooth for the other two alpha values. This is clearly related to the oscillations seen in the radial velocity in the subsection before. However, the non-oscillating regions look qualitatively similar to the ones of in the cases without oscillations. The range of values seems to be roughly the same apart from slight slope differences for $\alpha_{\text{K10}} = 5.0 \times 10^{-2}$ and 2.0×10^{-1} . According to Shakura and Sunyaev (1973) one expects a constant accretion rate (which should also mirror in the radial mass flow) throughout the whole disk and a dependence of the constant value on the α parameter. While we cannot see the any clear dependence on α here (the missing self-gravity might play a role) we see a constant plateau for the $\alpha_{\text{K10}} = 2.0 \times 10^{-1}$ case. When looking at the quantitative numbers we see $\approx (4.0 \pm 2.0) \times 10^{-3} M_{\odot} \text{ yrs}^{-1}$ which is roughly five to seven times lower than the predicted value. Again, we have to check if the missing self-gravity plays a role in this case. Furthermore, it should be checked if a full 3D simulation changes the result significantly. But it is already a significant milestone that the value is only one order of magnitude different from the predicted value.

3.4.3. Results in 3D

In the following, we discuss simulations in full 3D with 30 cells in the φ direction. Initially, we look at the plots from the beginning of the simulation after 8.0×10^4 yrs in Fig. 3.19 and Fig. 3.20. At first glance it is striking that there is no break of axis-symmetry in Fig. 3.19 for any of the quantities displayed. We compare the results to the plots of a 2D simulation (as discussed in the section before) at a similar time

3.4. Numerical simulations without self-gravity

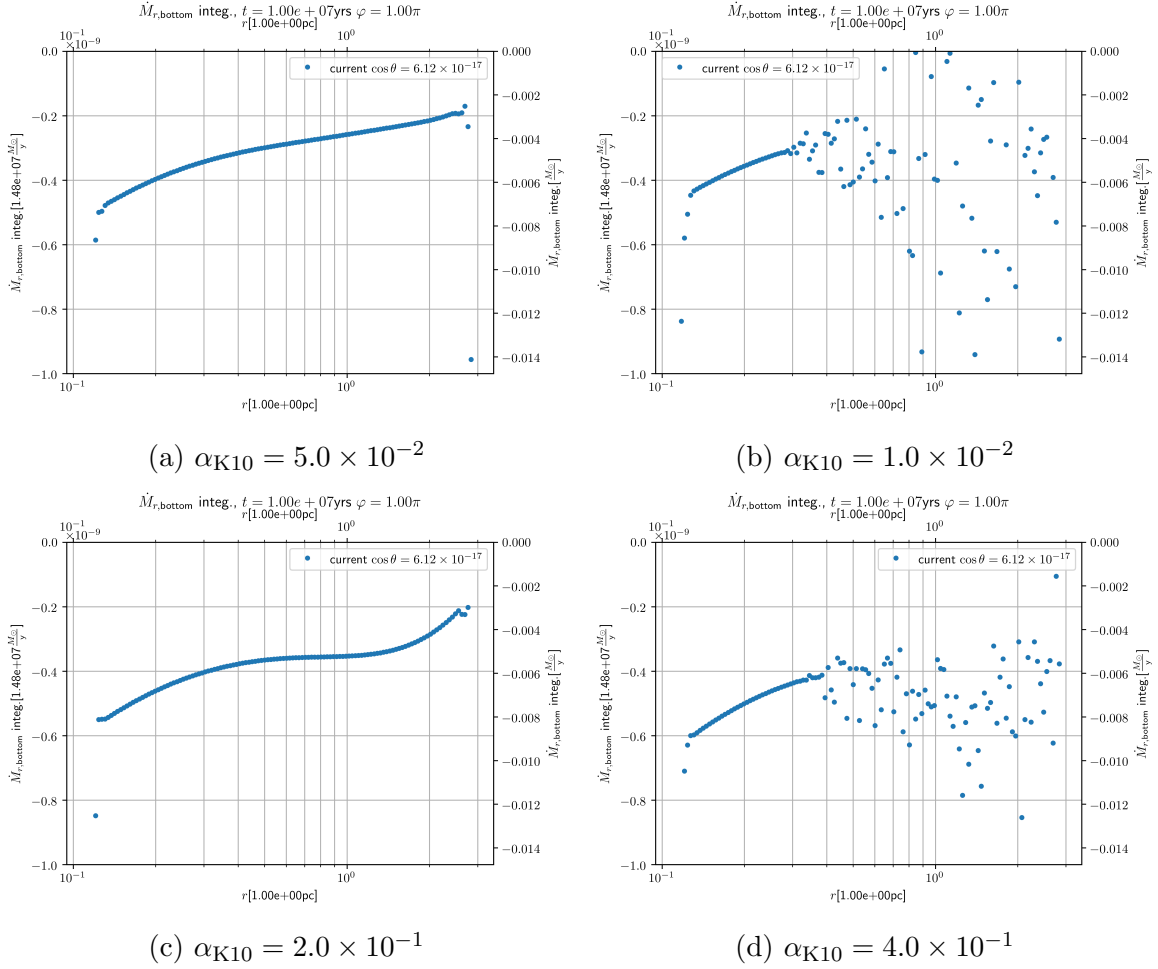


Figure 3.18.: Plots of the integrated radial mass flow from a 2D simulation without self-gravity for four different values of α

as to be seen in Fig. 3.21. When analysing the similarities and differences between these two, it is very noteworthy that there is no visible difference between them in the density plots in Fig. 3.20a and Fig. 3.21a. While the radial and θ velocity look very similar at first glance there are slight differences as indicated by the contour lines in Fig. 3.20b, Fig. 3.20c, Fig. 3.21b and Fig. 3.21c. These differences are, however, quite small. In the following we will again look on the scale-height, the radial velocity as well as the radial mass flow in order to see how different this is to a 2D axis-symmetric simulation.

3.4.3.1. Scale-height

Because of the almost exactly equivalent density profile we expect no change compared to the 2D simulation. This is well-proven by Fig. 3.22 (The cut in φ is not a problem as there are no differences in φ for ρ as shown before). The value for the constant $\frac{h}{R}$ is also equivalent to the one before in the given precision.

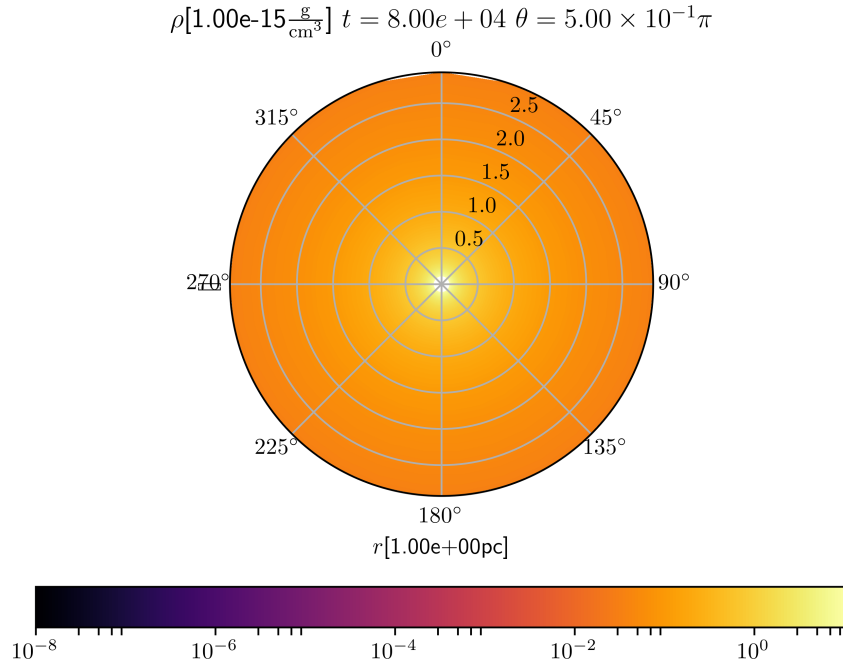
3.4.3.2. Radial mass flow

Again, we take a look at the integrated radial mass flow as a precursor for the accretion rate. A comparative plot for the 2D and 3D case can be seen in Fig. 3.23. While both cases still show oscillations above $r = 1$ pc, there are somewhat less oscillations near the inner boundary for the 3D case as to be seen in Fig. 3.23b. Overall the shape of the curves seems similar, but a closer investigation reveals that the values are shifted to more negative values for the 2D simulation as displayed in Fig. 3.23a which is also preserved up to 1.0×10^7 yrs as displayed in Fig. 3.18c. It is, roughly, $2.0 \times 10^{-2} M_{\odot} \text{ yrs}^{-1}$ lower than for the 3D case. The slight changes in the radial velocity that have been seen before could be the cause of this. In this case, this effect is amplified by the φ integration, as it sums up the velocities lower in magnitude for all φ . Unfortunately, this puts the number a bit further away from the predicted accretion rate value.

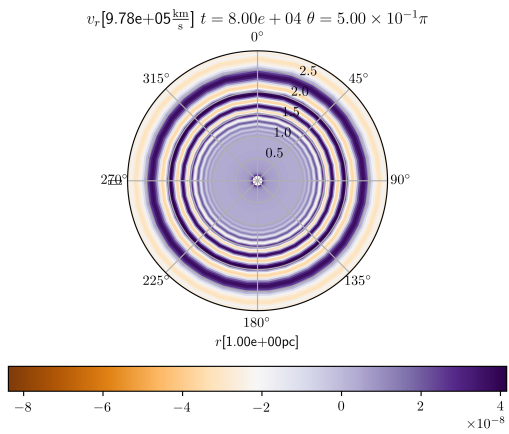
3.4.3.3. Why are there no longer 3D simulations?

Unfortunately, it turned out the 3D simulations are tremendously computationally expensive. Even reaching 5×10^4 yrs took 48h on 800 cores which is close to the limit of cores available on the clusters used for this project (BWfor, MilkyWay). When estimating how many cores are required to reach a decent performance one arrives at ≈ 3000 cores which are not easily obtainable within the given timeframe of this thesis. PLUTO is proven to scale to these core numbers in the PLUTO userguide. Thus, it was decided to focus all the computational power on performing one big 3D simulation with self-gravity and not continue big 3D simulations without self-gravity.

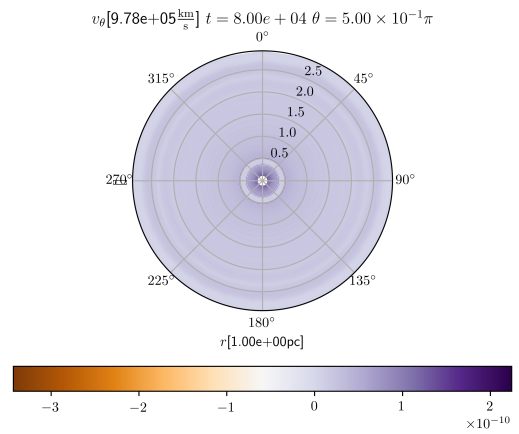
3.4. Numerical simulations without self-gravity



(a) ρ



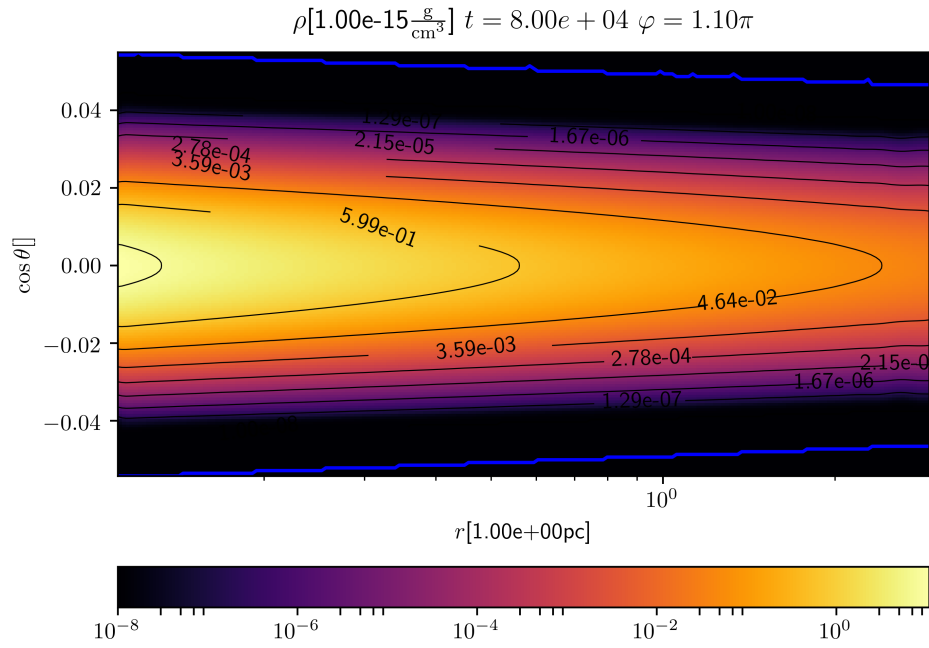
(b) v_r



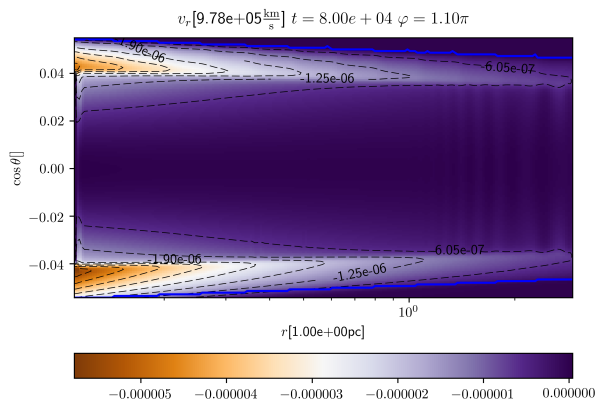
(c) v_θ

Figure 3.19.: Cut through the equatorial plane showing ρ , v_r and v_θ after 8.0×10^4 yrs from a 3D simulation with $\alpha_{K10} = 2.0 \times 10^{-1}$ without self-gravity

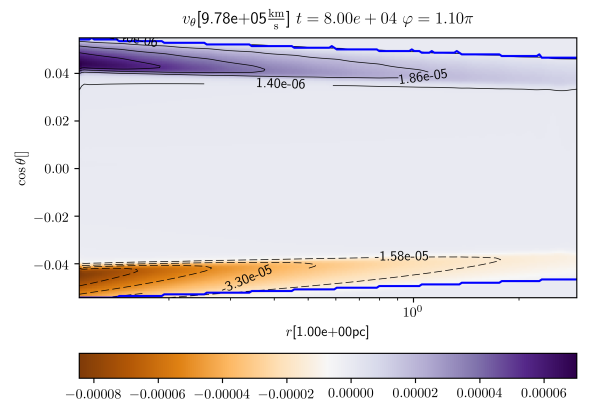
3. Numerical simulations using the PLUTO code and NBODY6++GPU



(a) ρ



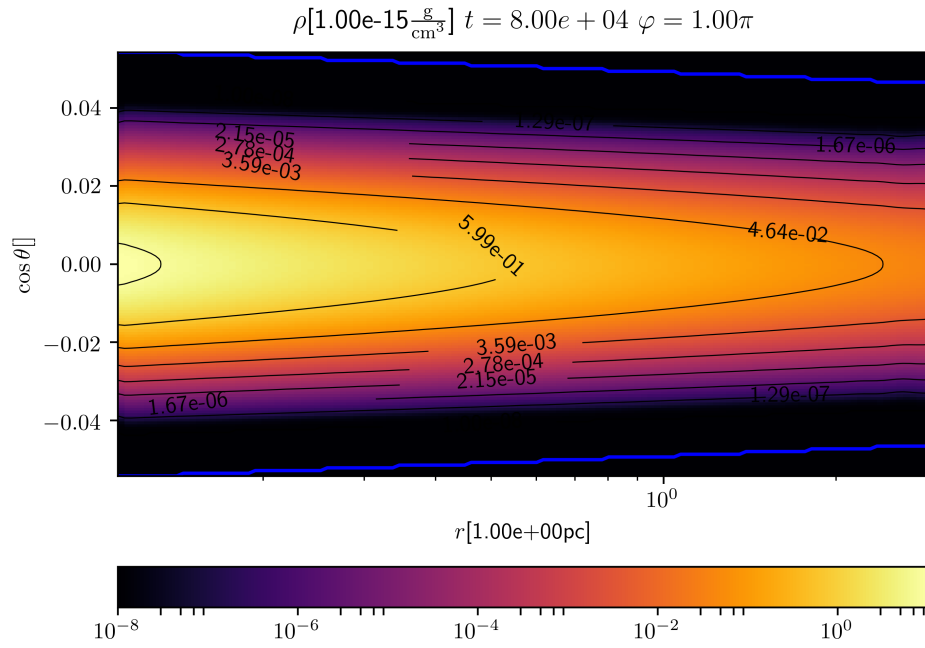
(b) v_r



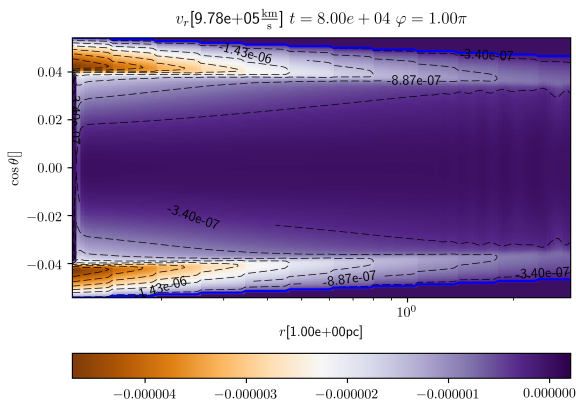
(c) v_θ

Figure 3.20.: Cut in φ showing ρ , v_r and v_θ after 8.0×10^4 yrs from a 3D simulation with $\alpha_{K10} = 2.0 \times 10^{-1}$ without self-gravity

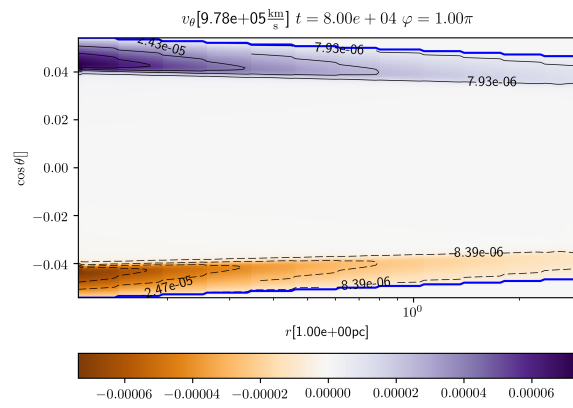
3.4. Numerical simulations without self-gravity



(a) ρ



(b) v_r



(c) v_θ

Figure 3.21.: Plot showing ρ , v_r and v_θ after 8.0×10^4 yrs from a 2D simulation with $\alpha_{K10} = 2.0 \times 10^{-1}$ without self-gravity

3. Numerical simulations using the PLUTO code and NBODY6++GPU

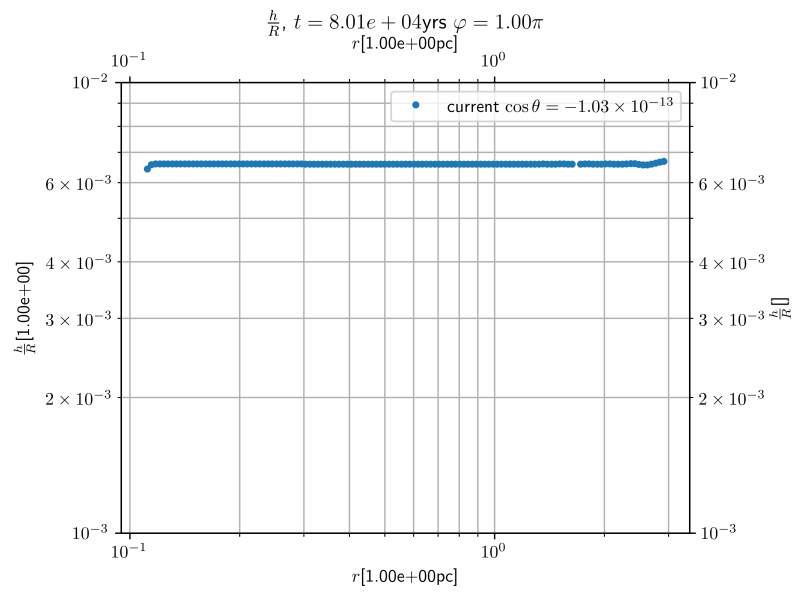
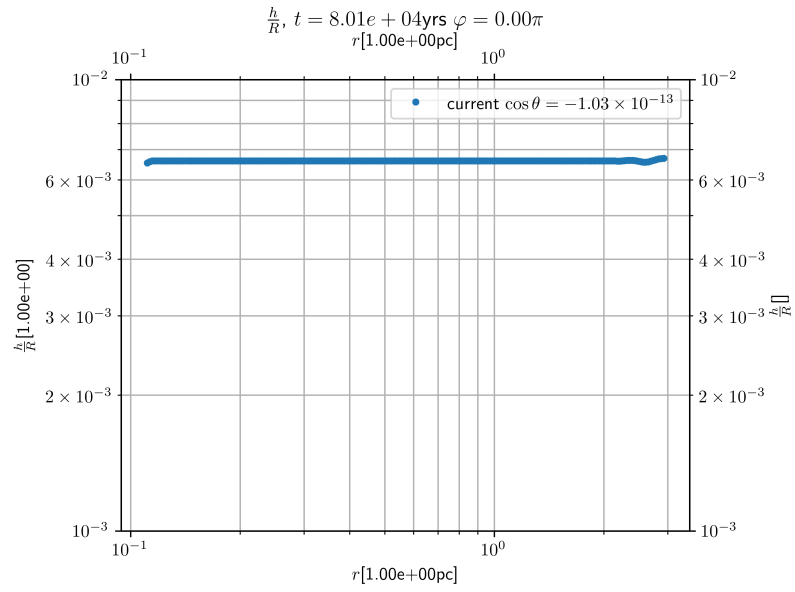


Figure 3.22.: $\frac{h}{R}$ as a cut in φ derived from a 3D simulation without self-gravity with $\alpha_{K10} = 2.0 \times 10^{-1}$

3.4. Numerical simulations without self-gravity

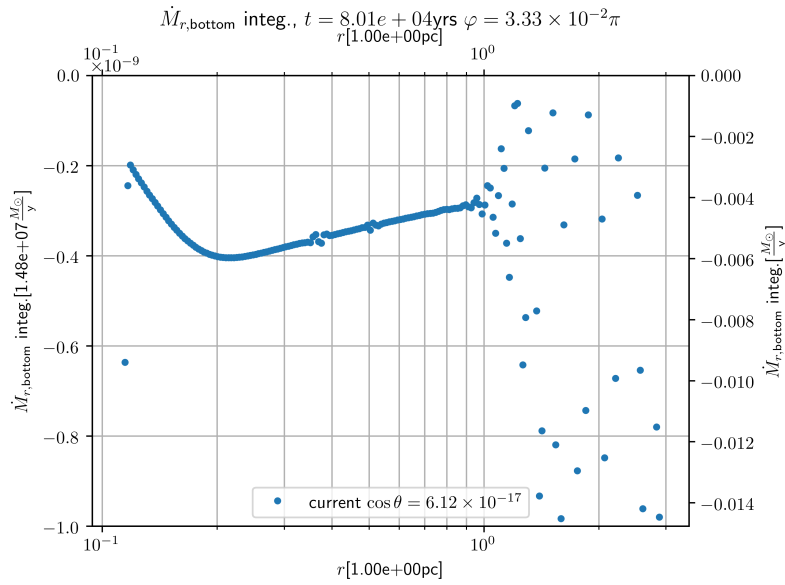
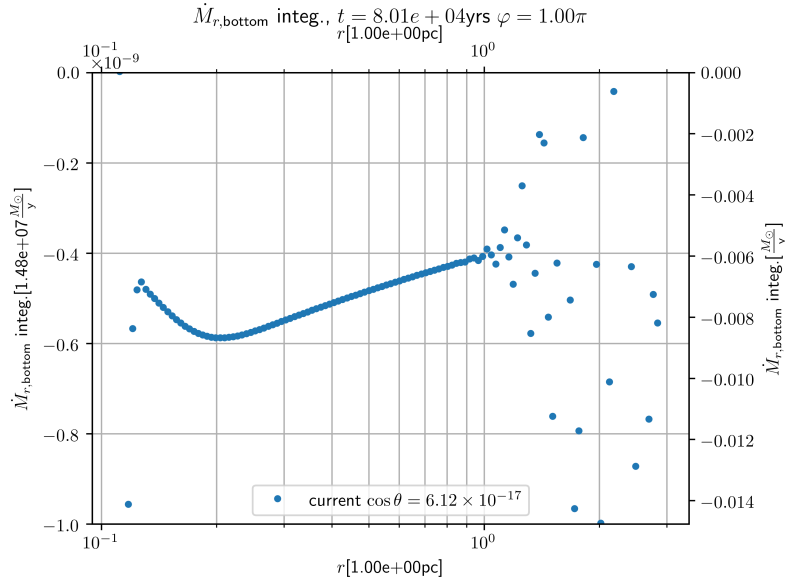


Figure 3.23.: Integrated accretion rate obtained from a 2D and 3D simulation after 8.0×10^4 yrs with $\alpha_{\text{K}10} = 2.0 \times 10^{-1}$

3.5. Numerical simulations with self-gravity

As self-gravity is an important aspect in the comparatively massive Active Galactic Nucleus (AGN) Accretion Disks (ADs) we now turn it on and also simulate the full radial range up to $R_d = 25$ pc. This will also enable us to confirm if a change in scale-height occurs as assumed in Kennedy et al. (2016) along with the question if there is an influence on the radial mass flow. As the presence of self-gravity might lead to instabilities we now include calculations of the Q_{Toomre} as presented in Subsection 2.3.8. As Q_{Toomre} does not depend on θ or φ only a radial analysis is sufficient.

3.5.1. Initial conditions

The initial conditions can be investigated in Fig. 3.24, Fig. 3.25 and Fig. 3.26. They are essentially the same as for the case without self-gravity apart from the radial range extending up to 25 pc. The Q_{Toomre} discussed in Subsection 2.3.10 is plotted in Fig. 3.27 for the range $Q_{\text{Toomre}} \leq 5$. We see that instabilities are expected for the higher r values because Q_{Toomre} is in the order of magnitude of 1 and also ≤ 1 . Additionally, one can rediscover that $Q_{\text{Toomre}} = 1$ for $r \approx 5$ pc as determined in equation (3.31).

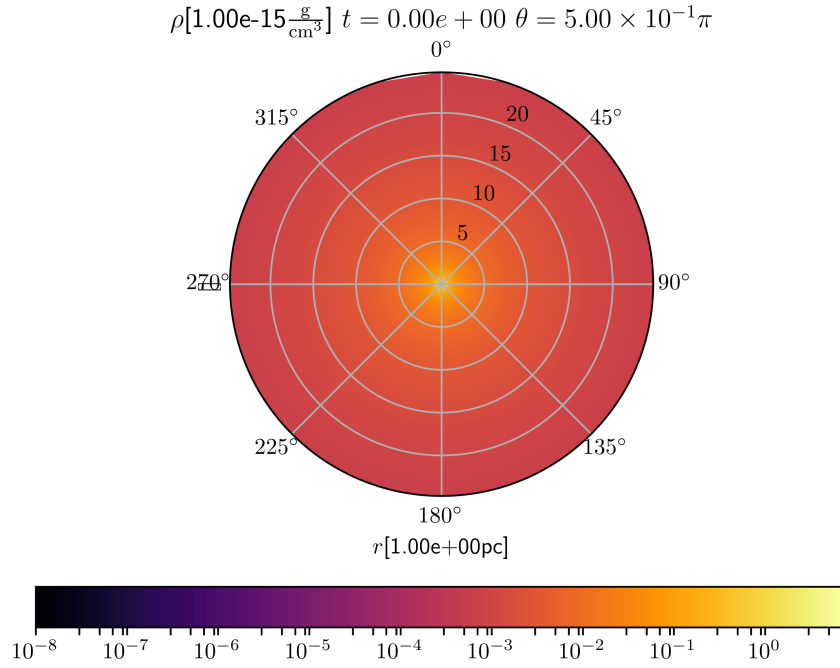
3.5.2. Results in axis-symmetric 2D simulations

As with the non-self gravitating case 2D simulations were performed at first. The plots after 8.0×10^4 yrs can be seen in Fig. 3.28 and Fig. 3.29. Once again small density oscillations, especially in Fig. 3.29a. One can also make them out prominently in the radial velocity in Fig. 3.29b. All features seem somewhat similar to the case without self-gravity. The instabilities predicted by the Q_{Toomre} are not yet visible confined to the predicted region.

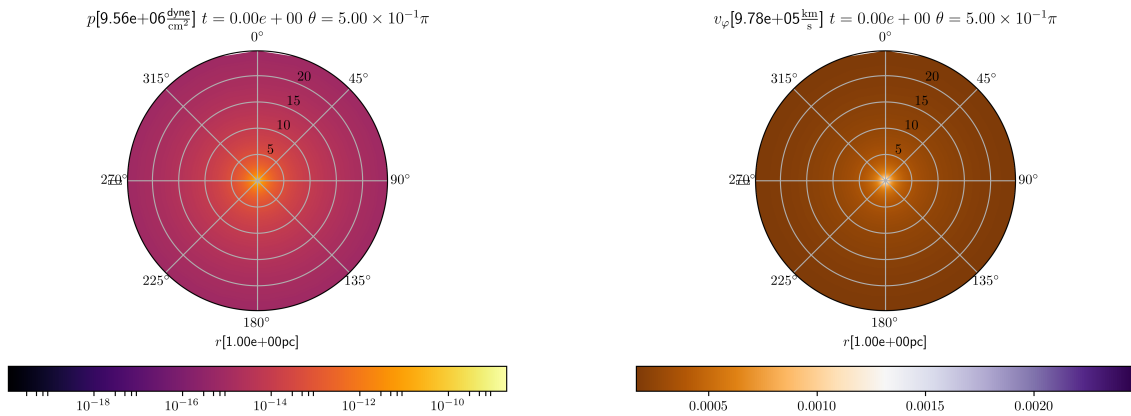
3.5.2.1. Equilibrated state

Now, the state after 1.0×10^7 yrs is displayed in Fig. 3.30 and Fig. 3.31. We see that while a steady state has been reached the oscillations have NOT disappeared like in the none self-gravitating case. This can be seen best in the density (Fig. 3.30a and Fig. 3.31a) and the radial velocity (Fig. 3.30b and Fig. 3.31b), respectively. For $R \geq 10$ pc the disk seems to have mostly disrupted and thinned considerably. Moreover, there is a build-up of density around 20 pc with minimal density behind it. The Fig. 3.31b shows a hard boundary in velocity that has formed at the some position. Furthermore, Fig. 3.31c shows a point where $v_\theta = 0$ before rising again. One suspicion might be that strong oscillations have disrupted the disk. When looking at Fig. 3.27 and equation (2.177) and equation (3.31) one more time one can discover that the oscillations start at the radius that corresponds to $Q_{\text{Toomre}} = 1$ in the initial conditions (≈ 5 pc) and thus agreeing with the expectation of instability in this region very well. Thus, we are not dealing with numerical noise but with a physical effect

3.5. Numerical simulations with self-gravity



(a) ρ

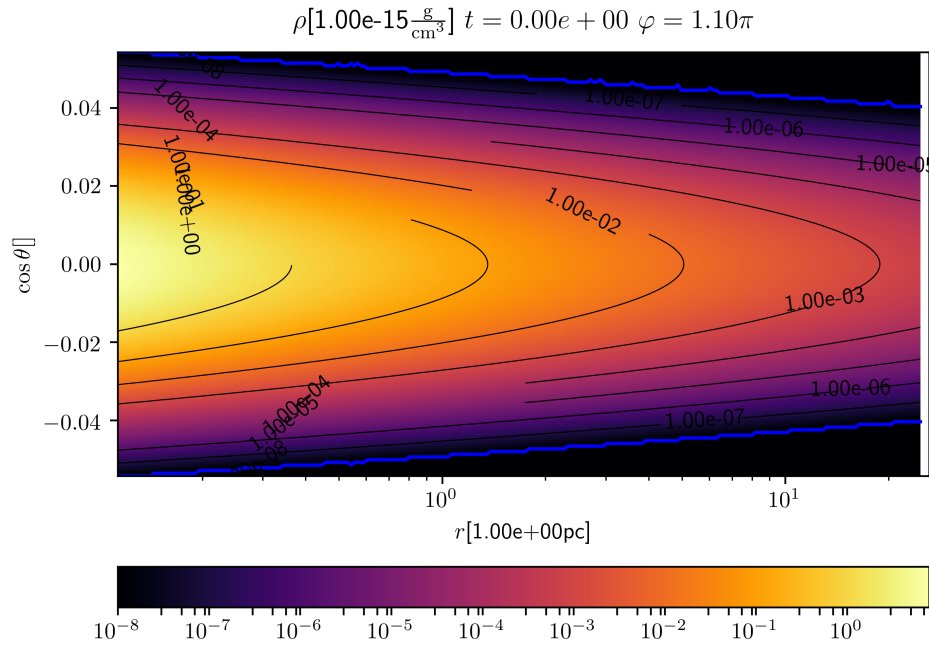


(b) p_{tot}

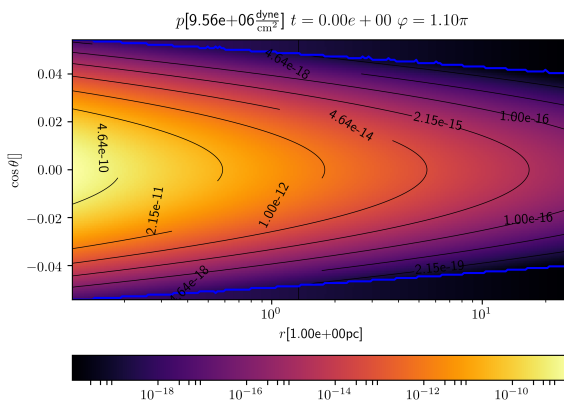
(c) v_φ

Figure 3.24.: Initial conditions with self-gravity showing a cut in θ showing the equatorial plane

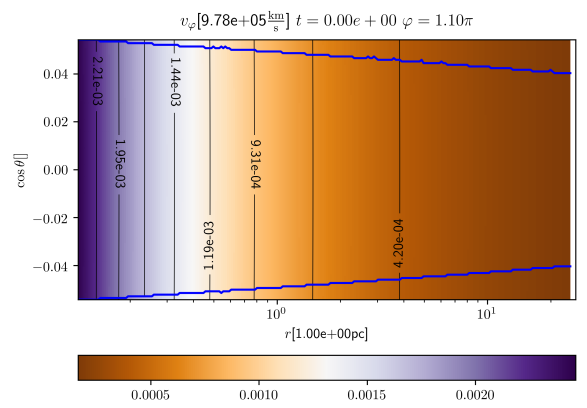
3. Numerical simulations using the PLUTO code and NBODY6++GPU



(a) ρ



(b) p_{tot}



(c) v_{φ}

Figure 3.25.: Initial conditions with self-gravity showing a cut in φ , blue lines represent the initial line of the minimum density

3.5. Numerical simulations with self-gravity

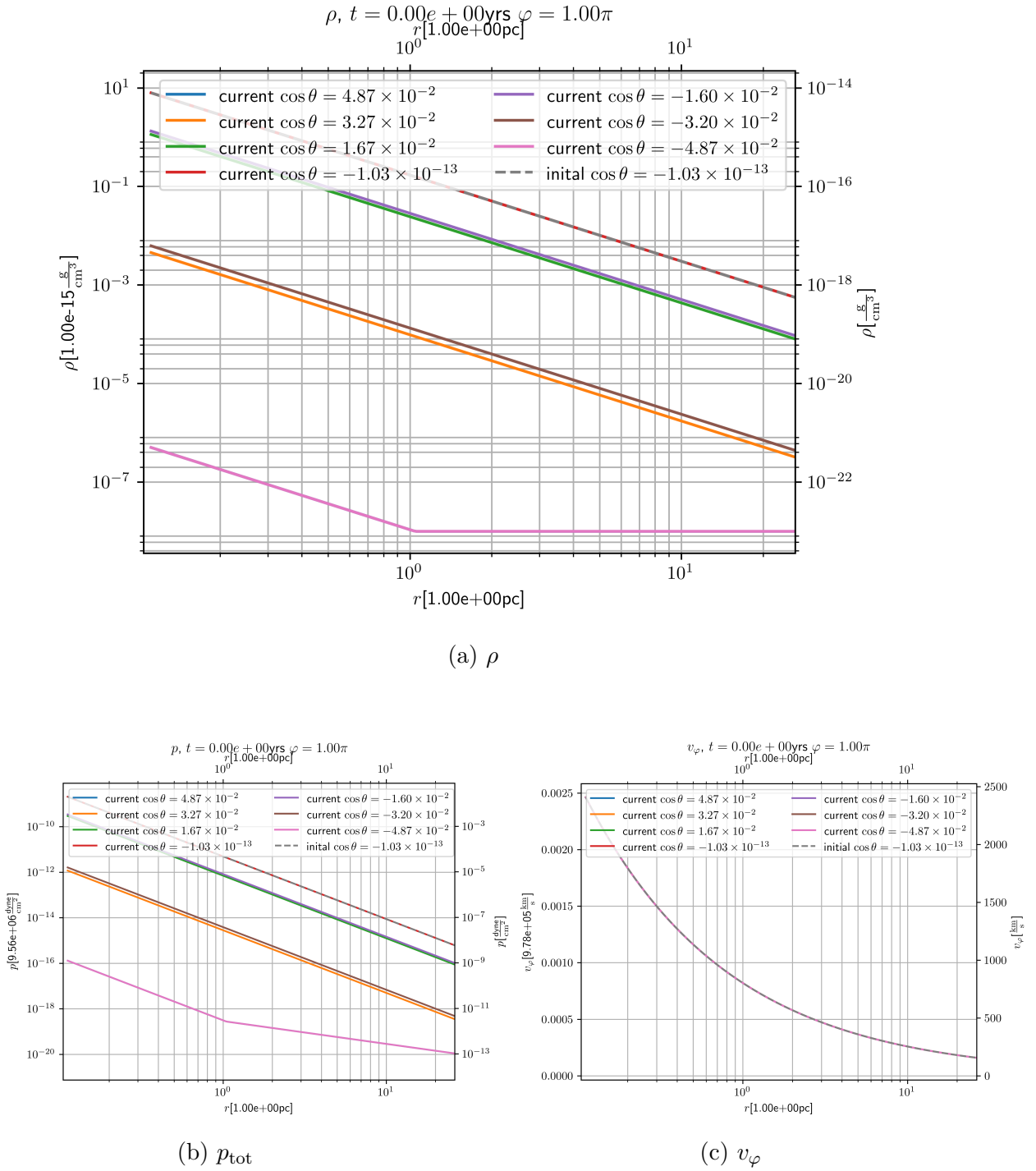


Figure 3.26.: Initial conditions with self-gravity showing a cut in φ and several θ values

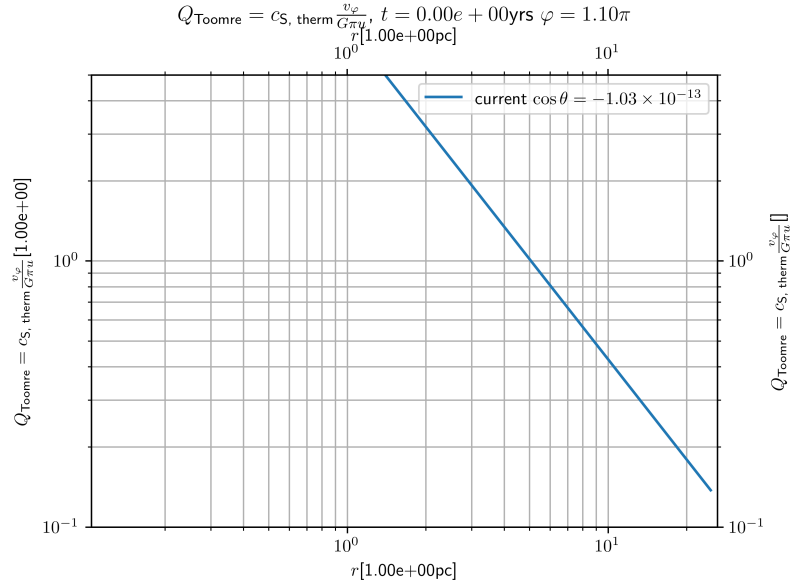


Figure 3.27.: Toomre Q determined from the initial conditions for the standard parameters of a simulation with self-gravity, plotting range limited to $Q_{\text{Toomre}} \leq 5$

here matching the theoretical predictions. Similar to the none-self-gravitating case v_φ is almost unchanged apart from minor oscillations near the outer boundary which are not surprising considering the disturbances in this region as seen in Fig. 3.32.

3.5.2.2. Analysis of the scale-height

Like in the simulations without self-gravity we take a look at the scale-height in a similar manner. First, we plot the fits as can be investigated in Fig. 3.33. One can quickly see that the before-mentioned oscillations disturb the fitted values for $r \geq 5$ pc. Despite of these oscillations we can see a major assumption of Kennedy et al. (2016) realised in the plots. Kennedy et al. (2016) assumes a linear growing scale-height until the approximate radius where the vertical self-gravity dominates over the central Super Massive Black Hole (SMBH) gravity (here ≈ 2.92 pc) after which the scale-height becomes constant. The curve in Fig. 3.33a begins linearly and then slowly changes curvature to become more and more flat. This gradual behaviour is expected as the ratio of the two gravity forces also changes gradually and not at one point. When looking at Fig. 3.33b displaying $\frac{h}{R}$ one can read of that the value of the constant in the linear growing regions is, similarly to the non-self-gravitating case, as

$$\frac{h}{R_{\text{linear}}} \approx 6.3 \times 10^{-3}. \quad (3.53)$$

3. Numerical simulations using the PLUTO code and NBODY6++GPU

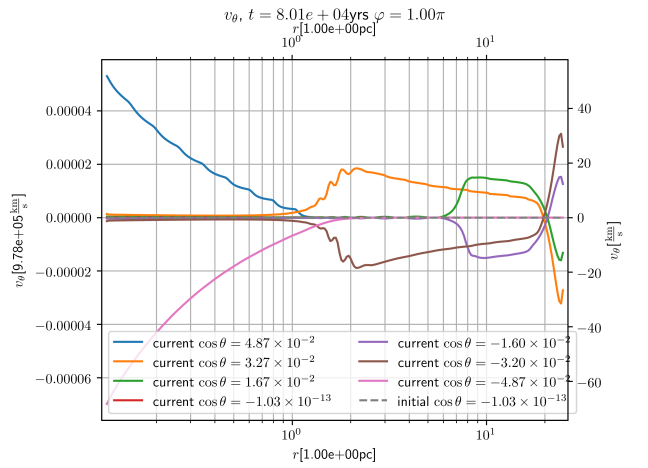
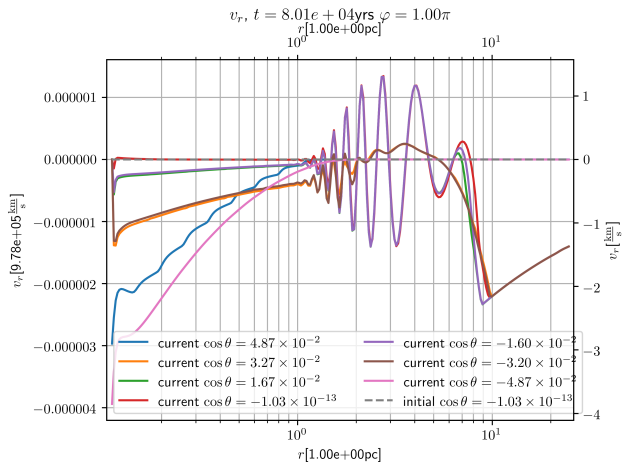
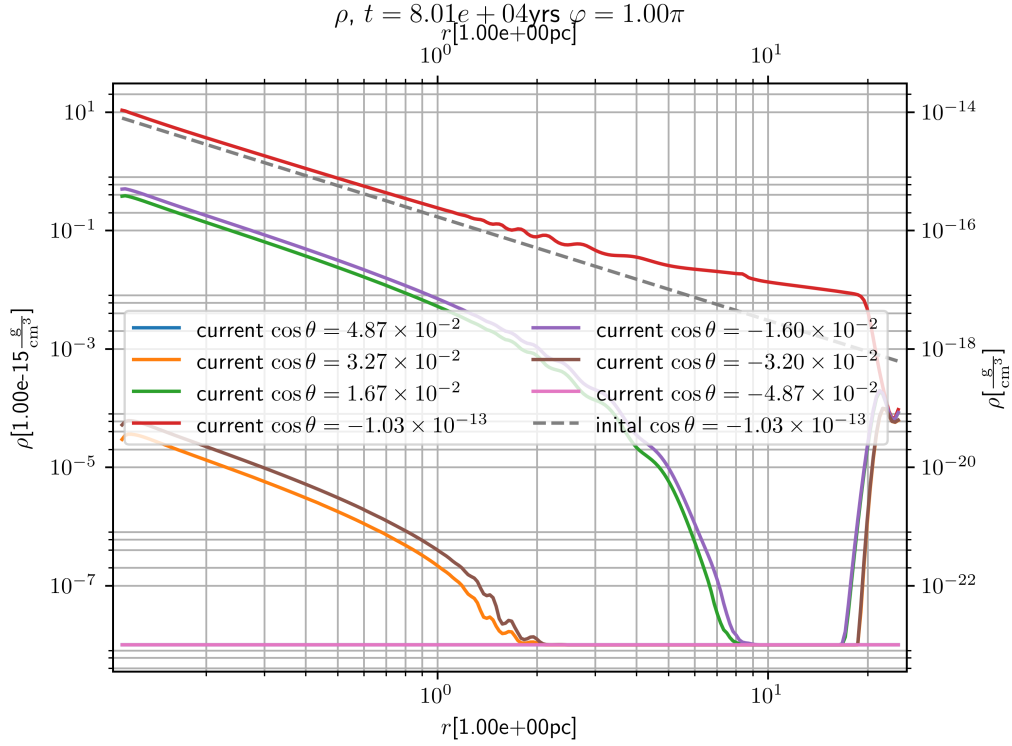


Figure 3.29.: 1D Plots as several cuts in θ of ρ , v_r and v_θ after 8.0×10^4 yrs from a 2D simulation with $\alpha_{K10} = 2.0 \times 10^{-1}$ with self-gravity

3. Numerical simulations using the PLUTO code and NBODY6++GPU

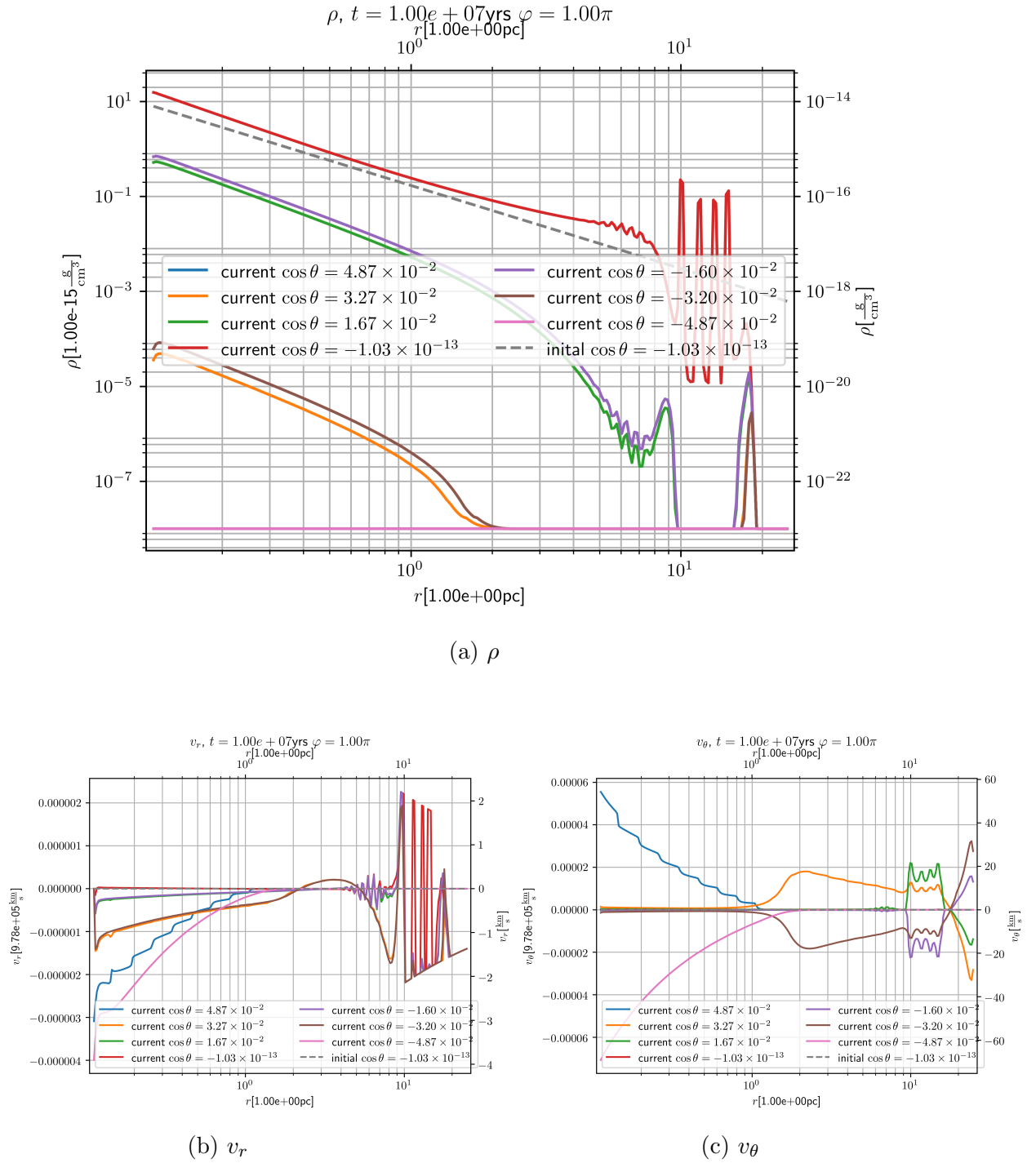


Figure 3.31.: 1D Plots of ρ , v_r and v_θ after 1.0×10^7 yrs from a 2D simulation with $\alpha_{K10} = 2.0 \times 10^{-1}$ with self-gravity, the blue line denotes the line of the initial minimum density which marks the borders of the integrated domain

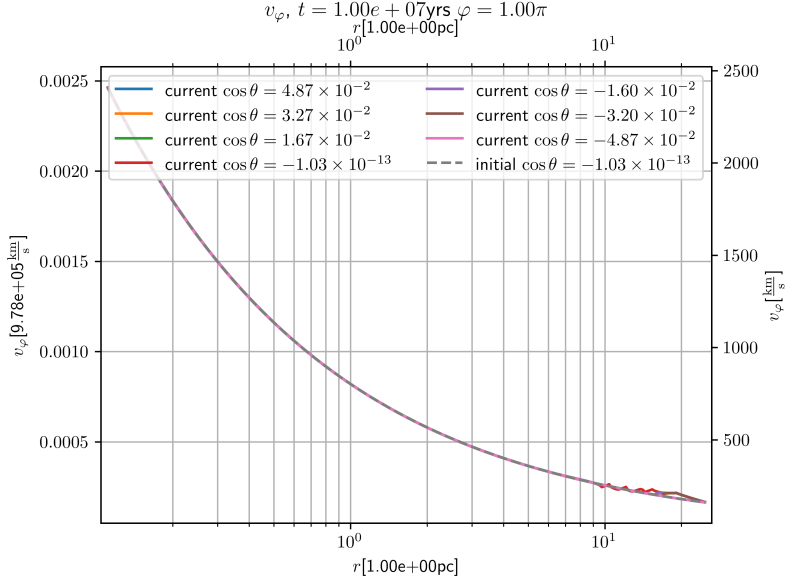


Figure 3.32.: v_ϕ after 1.0×10^7 yrs from a 2D simulation with $\alpha_{K10} = 2.0 \times 10^{-1}$ with self-gravity

So the scale-height has decreased in a similar manner. The constant scale-height value (predicted to be 2.5×10^{-2} pc by Kennedy et al. (2016)) can roughly be estimated to

$$h_{\text{const}} \approx 1.8 \times 10^{-2}. \quad (3.54)$$

This value is very close to the value predicted by Kennedy et al. (2016) which is a very encouraging result along with the correct transition. It also shows that the assumptions used in Just et al. (2012), Kennedy et al. (2016) in order to arrive at the constant scale-height as well as the transition radius are reasonable.

3.5.2.3. Analysis of the radial velocity

Again in similarity to the analysis performed for the case without self-gravity we take a closer look at the radial velocity by fitting a power law to the data and compare the results for different α values. Because of the oscillations we restrict the fitting to the region where the central SMBH gravity dominates over self-gravity. For more information on the fitting and this aspect please refer to Subsection 3.6.2. The corresponding results are displayed in Fig. 3.34. The plot of the constant a , which can be investigated in Fig. 3.34a, looks somewhat similar to the same figure for the none-self gravitating case (see Fig. 3.16a). The main difference is a more pronounced asymmetry in θ showing a shallower decline of the prefactor for $\cos \theta > 0$. Also, there seems to be a smaller amount of slightly positive values near the equatorial plane. The equatorial plane itself, however, is at 0 for both cases. Again the local minima appear at $\cos \theta \approx \pm 0.03$, but in contrast to the self-gravitating case the number value is about

3. Numerical simulations using the PLUTO code and NBODY6++GPU

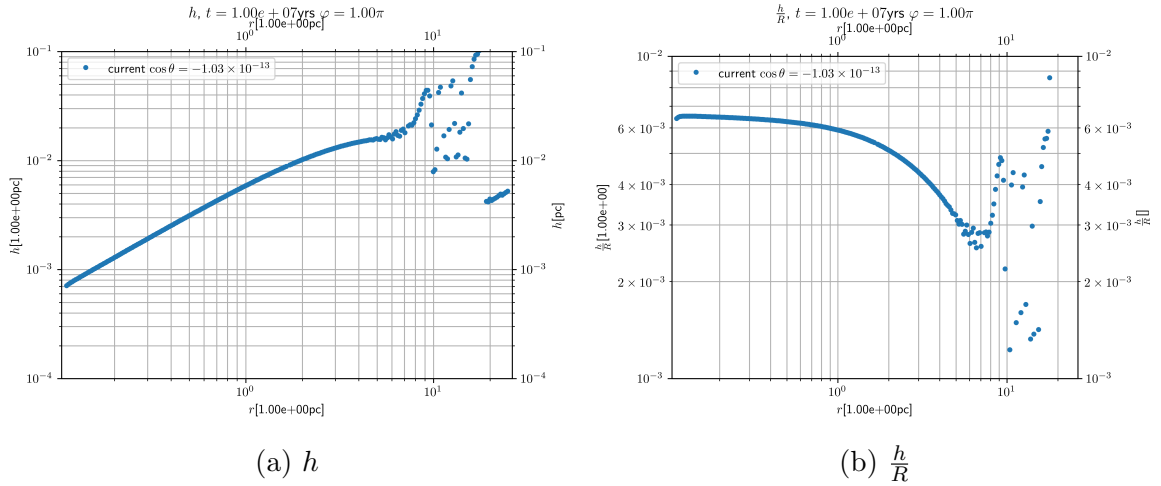


Figure 3.33.: Scale-height h and aspect ratio $\frac{h}{R}$ after 1×10^7 yrs derived from a 2D simulation with self-gravity and $\alpha_{K10} = 2.0 \times 10^{-1}$

16% less deeply negative. The overall range of values is roughly the same though. Now we focus our attention on the p parameter that is representing the exponent which, according to Shakura and Sunyaev (1973), should be $\frac{1}{4}$. This is plotted in Fig. 3.34b which only somewhat resembles the shape of the figure in the case without self-gravity (see Fig. 3.16b). It is far less symmetric and we do not see the characteristic very negative values of the none-self-gravitating case (-16). Instead of this we see a zero line for $\alpha_{K10} = 1.0 \times 10^{-2}$ and slightly positive values for the other α . Additionally, we see one downward spike at $\cos \theta \approx -0.05$ in the negative part and a dripping down of values for the positive case. What is still similar is that we see a region of roughly constant $p \approx -1$ in approximately $\cos \theta \in [\pm 0.01, \pm 0.04]$. In both the case with and without self-gravity $\alpha_{K10} = 1.0 \times 10^{-2}$ is not showing this behaviour. Summed up, the self-gravity gives us a slightly more clear result. For a more general overview we also plotted the radial velocities in Fig. 3.35. These are mostly similar to the non-self-gravitating case apart from the oscillations caused by the instabilities for high r . Even the fact that $\alpha_{K10} = 1.0 \times 10^{-2}$ shows a somewhat erratic behaviour compared to the other simulations with different α values. The values themselves are mostly similar. So apart from the oscillations there is no qualitative difference visible and it really needs the quantitative analysis executed above in order to see the differences.

3.5.2.4. Analysis of the radial mass flow as a precursor for the accretion rate

Again, the radial mass flow is investigated here. As the title already gives away we now again look at the integrated radial mass flow as a precursor for the accretion rate. The plots for varying α can be seen in Fig. 3.36. On first glance it is obvious that the ever-present oscillations due to the instabilities caused by the self-gravity prevent us from obtaining a proper values for $r \gtrsim 3$ pc which is a bit smaller of a radius than observed for the other quantities. Overall, it can be seen that there are less

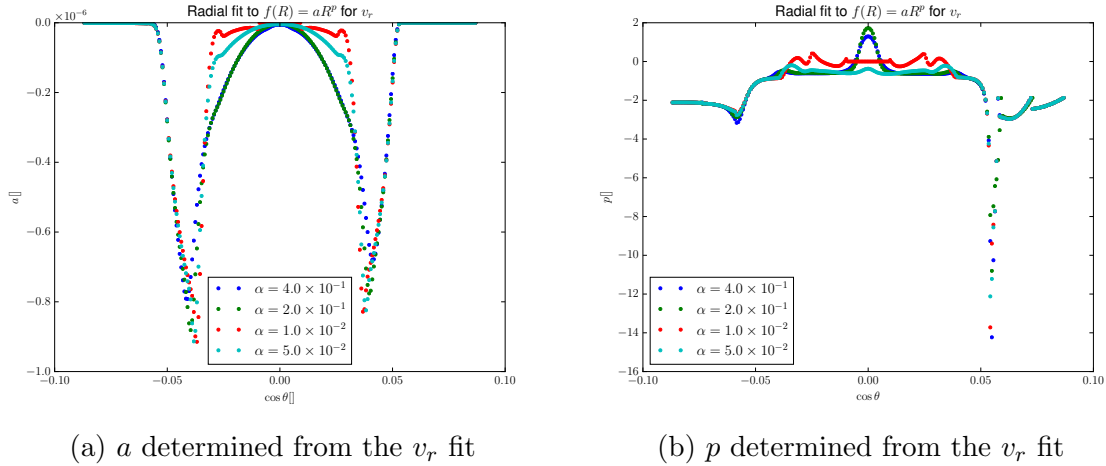


Figure 3.34.: Plots of the power law $f(R) = aR^p$ fitting parameters for v_r for different values of α determined from a 2D simulation with self-gravity, be aware that there is no unit stated for a as it depends on the value of p

differences from a straight line in the plots compared to the case without self-gravity (see Fig. 3.18). This is an encouraging results. The higher α values show more of a dip compared to the lower values of α . It is interesting that Fig. 3.36a and Fig. 3.36b are very similar suggesting that α does not have an influence beyond a certain lower limit. In contrast to the simulations without self-gravity we can see more clearly that a higher α results in a higher mass flow (and thus accretion rate) especially when looking at Fig. 3.36c and Fig. 3.36d. The self-gravity seems to stabilise the radial mass flow which shows that it is integral to the mass flow in AGN ADs. Looking at Fig. 3.36c we can again estimate

$$\dot{M} \approx (0.05 \pm 0.01) M_{\odot} \text{ yrs}^{-1} \quad (3.55)$$

again placing the values at roughly five times the value expected from Shakura and Sunyaev (1973). Overall this results is encouraging as we could arrive at a number this close despite of not yet including momentum transfer through radiation.

3.5.3. Results in 3D

Again we now look at fullscale 3D simulation to see if any significant changes appear when the φ dimension is fully simulated and axissymmetry is not enforced. The initial conditions are again the same as for the 2D case and we chose to use $\alpha_{K10} = 2.0 \times 10^{-1}$. First we look at plots made after 8.0×10^4 yrs as displayed in Fig. 3.37 and Fig. 3.37. On closer inspection Fig. 3.37 shows (as also the case for the simulations without self-gravity) no visible deviations from the symmetry in φ in neither of the quantities plotted. Fig. 3.37b and Fig. 3.38b, displaying v , gain show the well-known oscillation patterns caused by the self-gravity. When comparing it to the plot in 2D (Fig. 3.28)=,

3. Numerical simulations using the PLUTO code and NBODY6++GPU

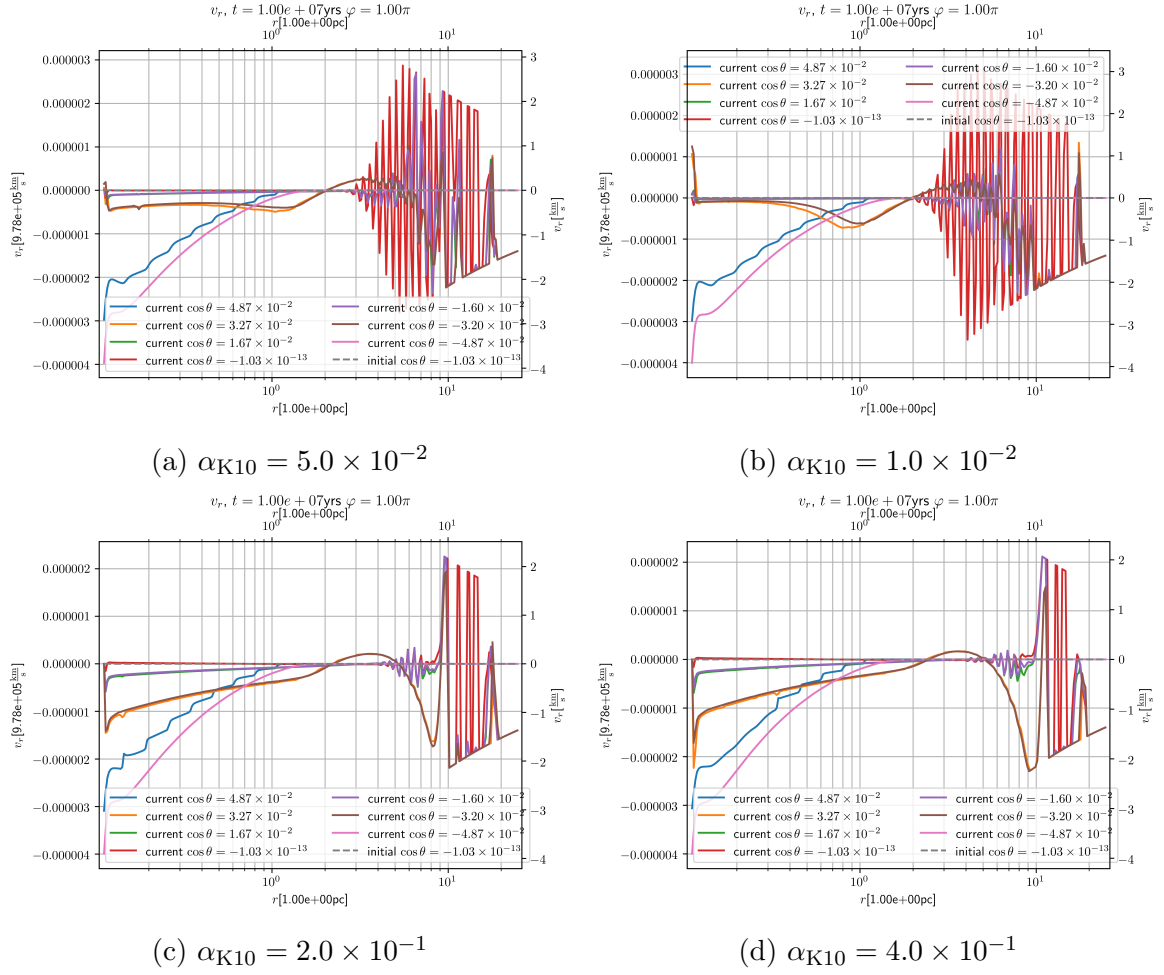


Figure 3.35.: Plots of v_r for a variety of θ values derived from 2D simulation with self-gravity for four different values of α

3.5. Numerical simulations with self-gravity

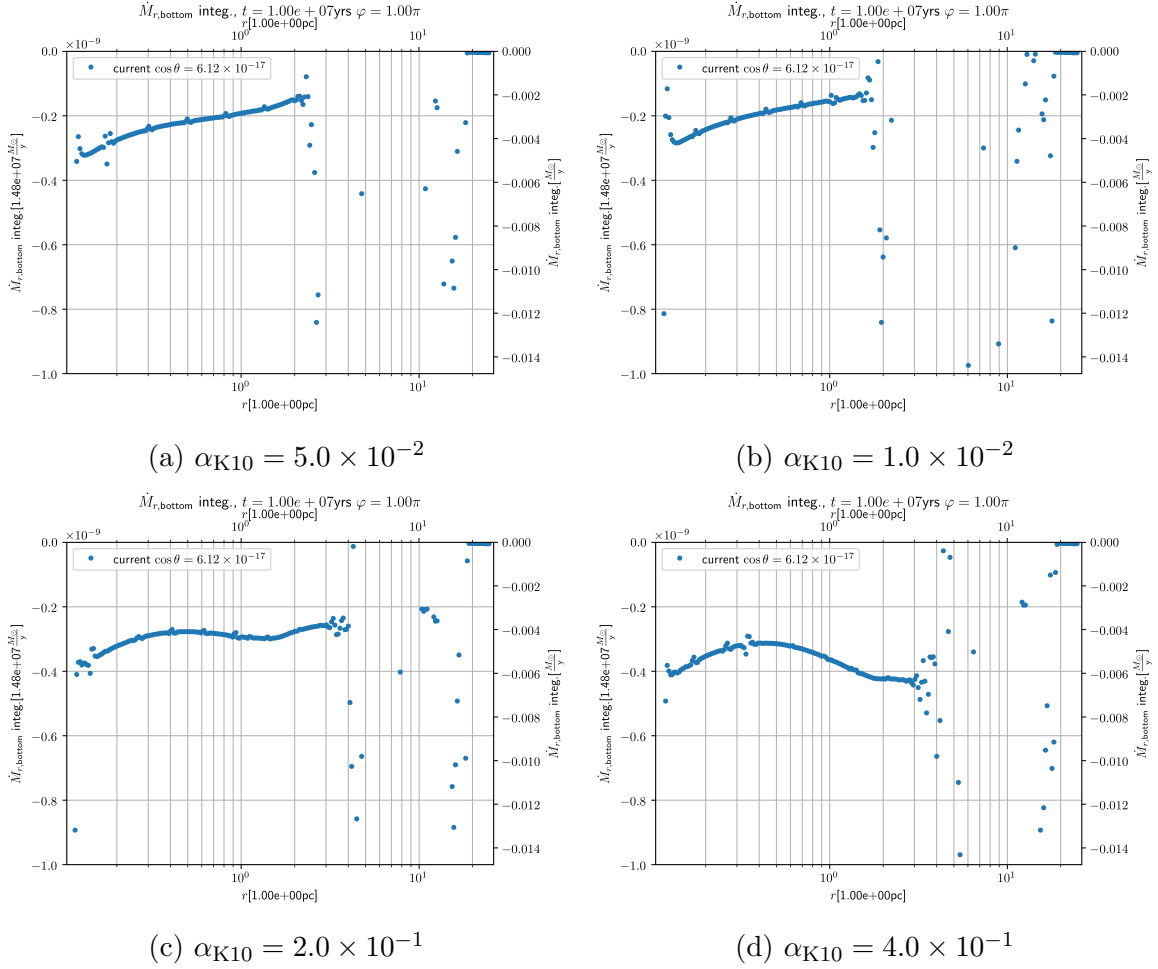


Figure 3.36.: Plots of the integrated radial mass flow from a 2D simulation with self-gravity for four different values of α after 1.0×10^7 yrs

they seem a bit less severe in the 3D case. This will be investigated in further detail for the mostly equilibrated state. No remarkable features can be seen in v_θ displayed in Fig. 3.37c and Fig. 3.38c apart from it being almost zero most of the time and having some odd features at the lower and upper radial boundaries.

3.5.3.1. Equilibrated state

As the beforementioned computational power demands prevent us from doing runs for millions of years a run with almost 1.0×10^6 yrs was performed in order to get an impression of the mostly equilibrated system. The know well-known plots for ρ , v_r and v_θ can be seen in Fig. 3.39 and Fig. 3.40. Fig. 3.40a clearly shows the oscillation pattern. However, it seems lighter than those seen in the 2D plots. The same can be said about v_r in Fig. 3.40b. This suggests that some effect is dampening the oscillations in the 3D simulations. What is still missing is an investigation of the state after 1.0×10^7 yrs which should be a subject of further work.

3.5.3.2. Analysis of scale-height

As before we investigate the scale height h and the aspect ratio $\frac{h}{R}$ determined by fitting. Fig. 3.41 contains time-averaged plots for both h and $\frac{h}{R}$. The time-averaging was employed in order to dampen the oscillations present. Especially the h , portrayed in Fig. 3.41a, showcases that the oscillations are a lot less prominent. When checking out Fig. 3.42, displaying the not time-averaged h , we see that this is not only due to the averaging, but also due to just less oscillations being present. This further encourages that there are less oscillations in the 3D simulations. In Fig. 3.41b the transition to a constant scale-height (and thus $\frac{h}{R} \propto \frac{1}{R}$) is visible again. It is even clearer here because of the smaller oscillations. However, because of the low simulation time this effect is not clearly obvious in Fig. 3.41a yet. We again try to estimate the constant scale-height for $r \geq R_{\text{SG}}$. Because of the bad visibility in the h plot we use the value for $r = 10$ pc in the $\frac{h}{R}$ figure to estimate

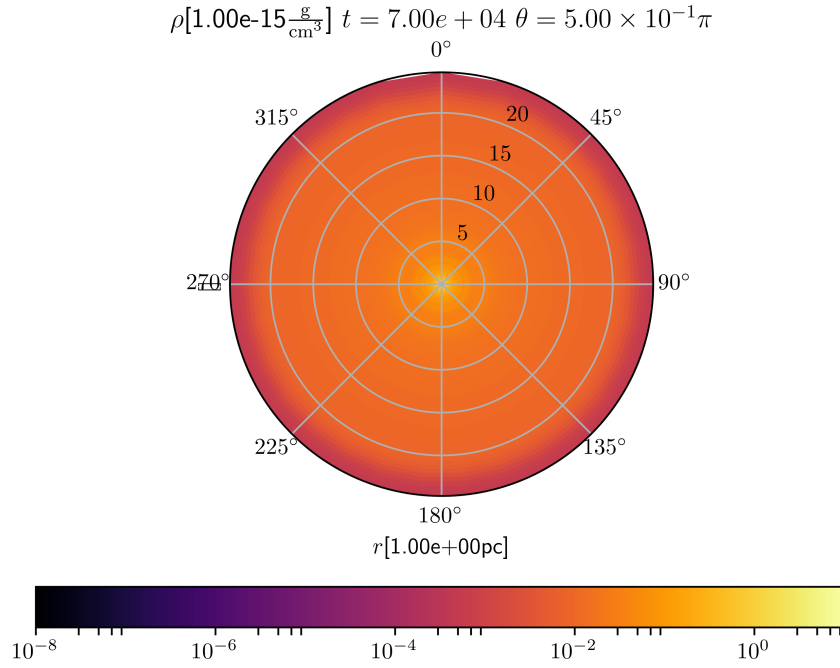
$$h = \frac{h}{R} (10 \text{ pc}) \approx 4.0 \times 10^{-2} \text{ pc}. \quad (3.56)$$

This number is quite close to the 1.8×10^{-2} pc determined for the 2D case. Potentially, the values might align if simulations of similar runtime would be possible. Once more, the result is close to the choice from Kennedy et al. (2016) (2.5×10^{-2} pc). Moreover, it is even closer to the choice from Kennedy et al. (2016) compared to the 2D case.

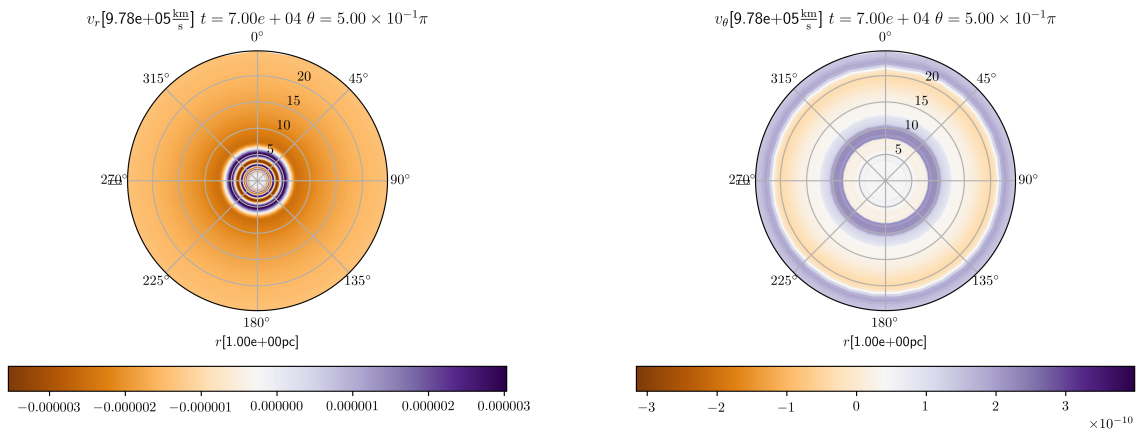
3.5.3.3. Analysis of the radial mass flow as a precursor for the accretion rate

Once more, the integrated radial mass flow is used as a precursor to the accretion rate. The result can be investigated in Fig. 3.43. Again we see roughly the same picture as before and again the result is equivalent to the ones from Kennedy et al. (2016). The somewhat higher oscillations, in comparison to the 2D simulations, are most probably

3.5. Numerical simulations with self-gravity



(a) ρ

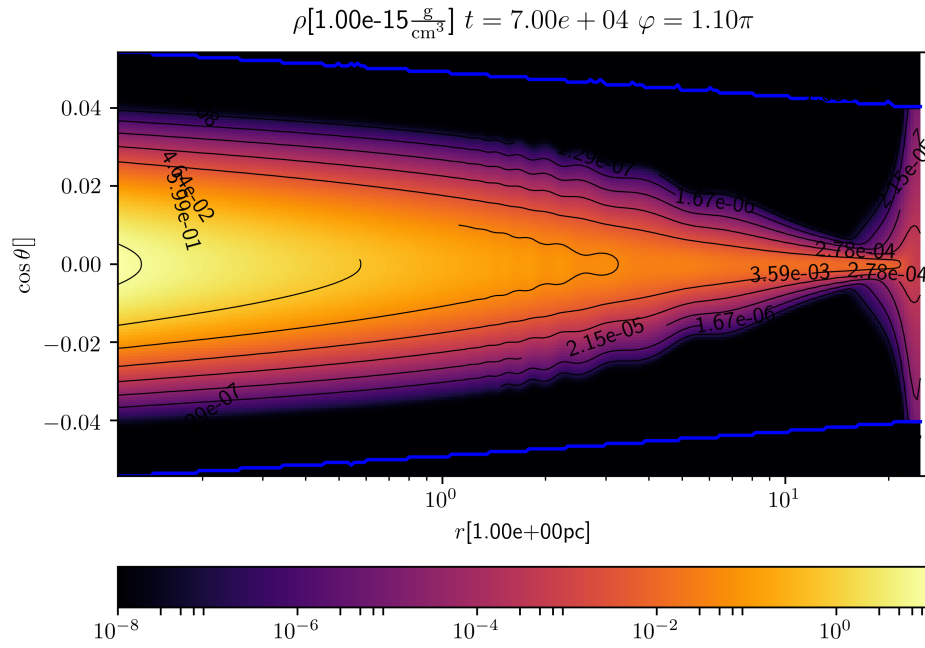


(b) v_r

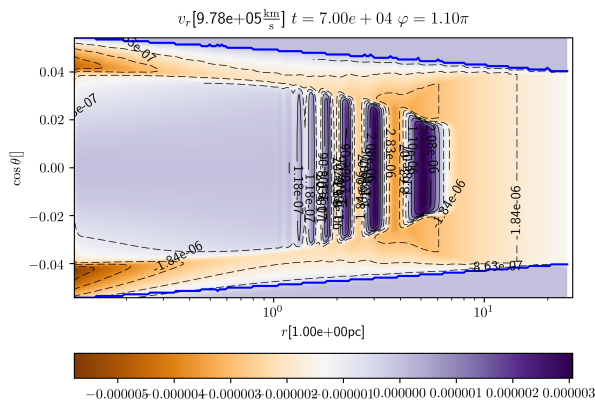
(c) v_θ

Figure 3.37.: Cut through the equatorial plane showing ρ , v_r and v_θ after 8.0×10^4 yrs from a 3D simulation with $\alpha_{K10} = 2.0 \times 10^{-1}$ wit self-gravity

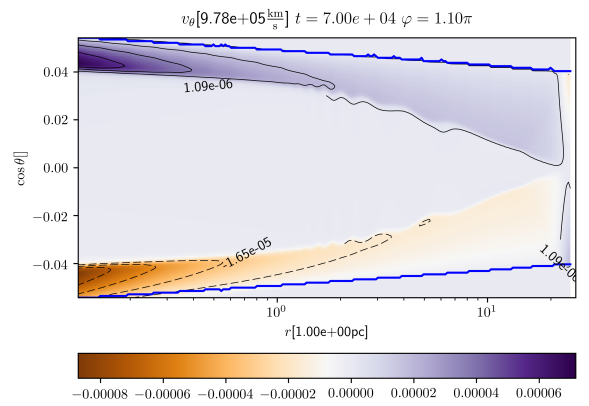
3. Numerical simulations using the PLUTO code and NBODY6++GPU



(a) ρ



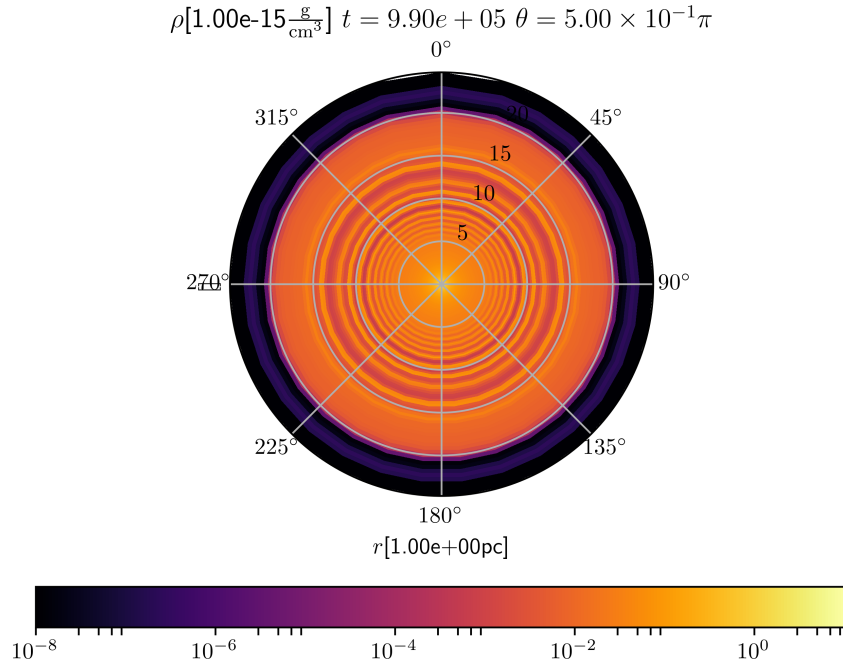
(b) v_r



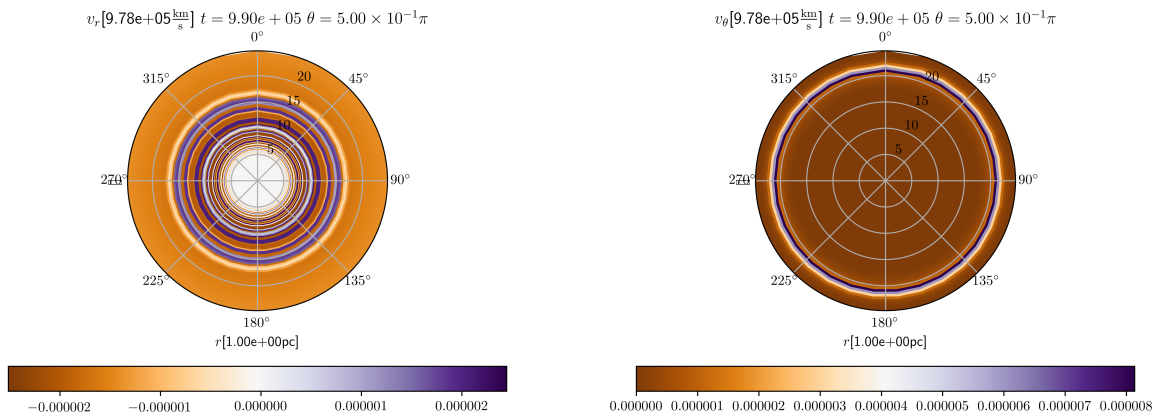
(c) v_θ

Figure 3.38.: Cut in φ showing ρ , v_r and v_θ after 8.0×10^4 yrs from a 3D simulation with $\alpha_{K10} = 2.0 \times 10^{-1}$ wit self-gravity

3.5. Numerical simulations with self-gravity



(a) ρ

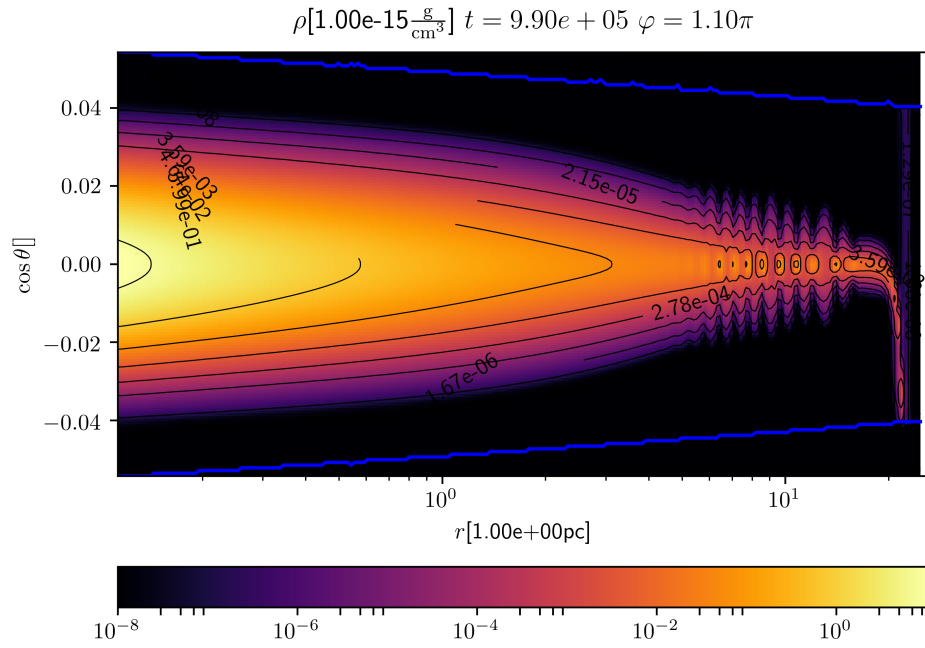


(b) v_r

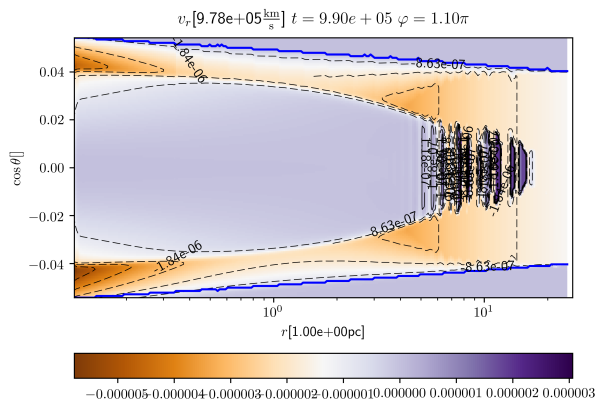
(c) v_θ

Figure 3.39.: Cut through the equatorial plane showing ρ , v_r and v_θ after 9.9×10^5 yrs from a 3D simulation with $\alpha_{K10} = 2.0 \times 10^{-1}$ wit self-gravity

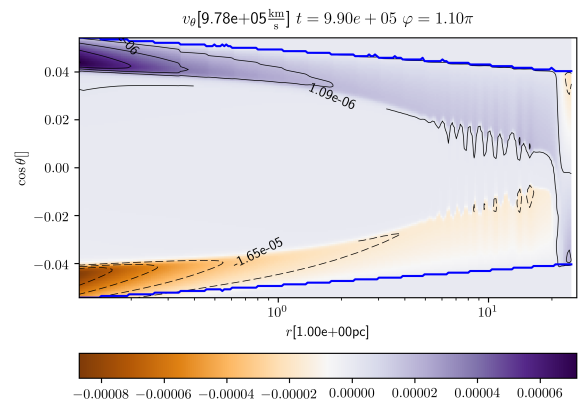
3. Numerical simulations using the PLUTO code and NBODY6++GPU



(a) ρ



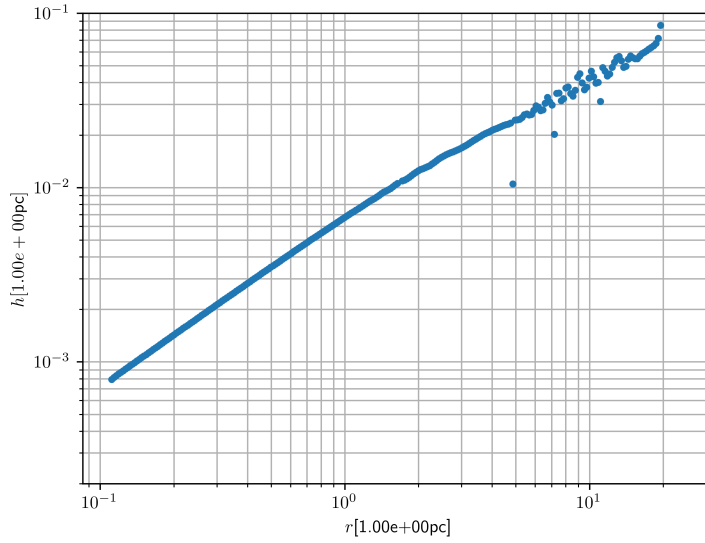
(b) v_r



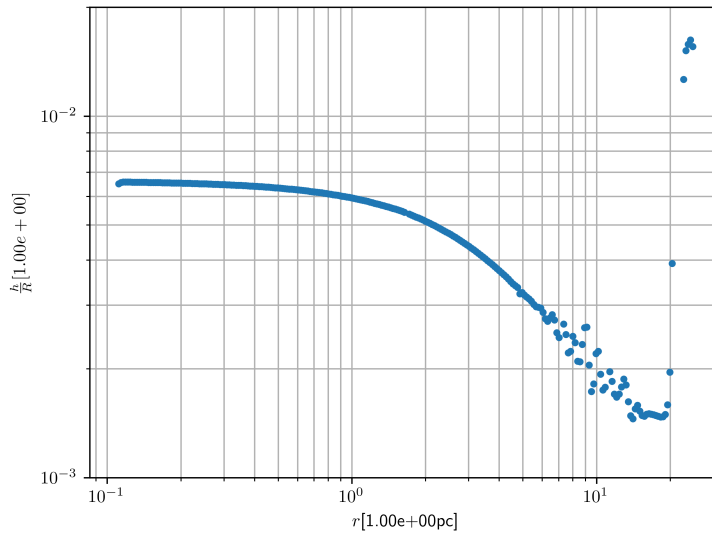
(c) v_θ

Figure 3.40.: Cut in φ showing ρ , v_r and v_θ after 9.9×10^5 yrs from a 3D simulation with $\alpha_{K10} = 2.0 \times 10^{-1}$ wit self-gravity

3.5. Numerical simulations with self-gravity



(a) h



(b) $\frac{h}{R}$

Figure 3.41.: Time-averaged (over 9.9×10^5 yrs) scale-height h and aspect ratio $\frac{h}{R}$ in a cut in φ obtained from a 3D simulation with self-gravity and $\alpha_{K10} = 2.0 \times 10^{-1}$

3. Numerical simulations using the PLUTO code and NBODY6++GPU

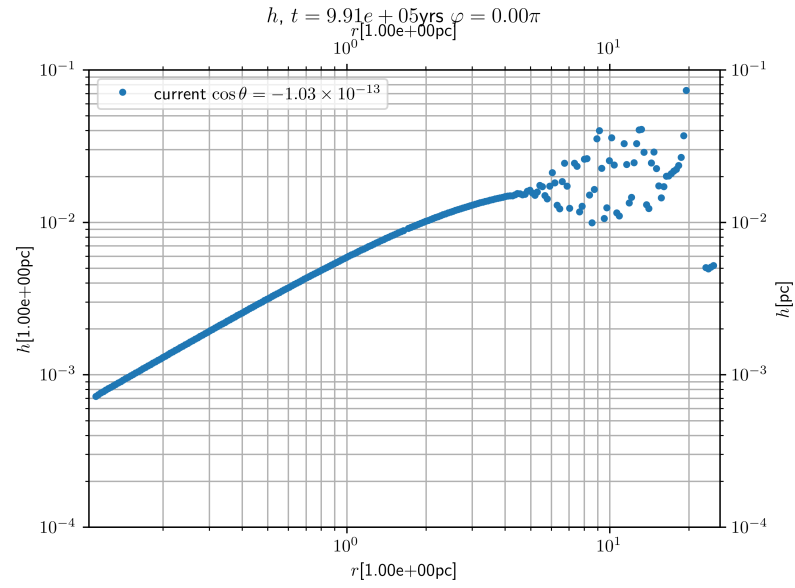


Figure 3.42.: None time-averaged after 9.9×10^5 yrs scale-height h in a cut in φ obtained from a 3D simulation with self-gravity and $\alpha_{K10} = 2.0 \times 10^{-1}$

related to the fact that only 9.9×10^5 yrs have passed here, while 1.0×10^7 yrs have passed in the 2D case. However, the general picture is confirmed.

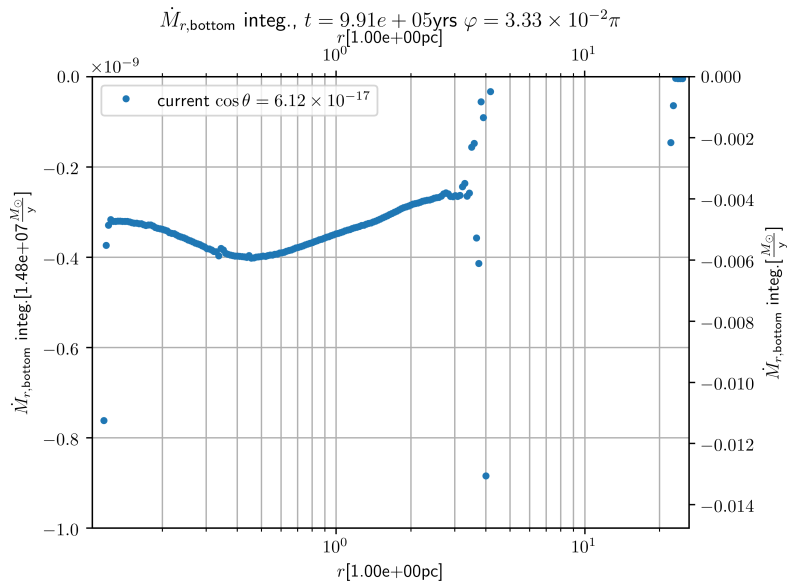


Figure 3.43.: Integrated radial mass flow obtained from a 3D simulation with $\alpha_{K10} = 2.0 \times 10^{-1}$ after 9.9×10^5 yrs

3.6. Using the data to do simulations with NBODY6++GPU

As we are interested if the equilibrated disk from the previous numerical simulations reproduces and/or changes the results from Just et al. (2012), Kennedy et al. (2016) (increased accretion rate compared to simulations without the disk). We expect at least slightly different results as the scale-height has equilibrated to a different value and we have non-zero v_r and v_θ . In order to be able to compare this we want to include the data in the direct nbody-code NBODY6++GPU (for details on the code see Spurzem (1999), Aarseth (2003), Wang et al. (2015)) and perform a simulation in the style of Kennedy et al. (2016) with this data. Basis for this is an implementation of the analytic drag acceleration into NBODY6++GPU created by Taras Panamarev. For the calculation of the resulting drag acceleration we will use equation (2.187) taken from Kennedy et al. (2016).

3.6.1. Creating a read-in module for the hydrodynamic simulation data

In order to make the data obtained in Section 3.5 available to NBODY6++GPU we need to get continuous data from the grid based data PLUTO supplies. Thus, a spatial interpolation scheme is required to obtain these values.

3.6.1.1. Spatial interpolation

First, given the Cartesian position (x, y, z) we need to calculate the corresponding spherical coordinates (r, θ, φ) via

$$r = \sqrt{x^2 + y^2 + z^2} \quad (3.57)$$

$$\theta = \arccos\left(\frac{z}{r}\right) \quad (3.58)$$

$$\varphi = \operatorname{atan}\left(\frac{y}{x}\right). \quad (3.59)$$

It should be noted that we need to take care to have $\varphi \in [0, 2\pi]$ by choosing the *atan2* function and adding 2π for negative results from that. In the following we determine the indices in the grid giving values closest to these i.e. find (i, j, k) such that the differences

$$|r_i - r|, |\theta_j - \theta|, |\varphi_k - \varphi| \quad (3.60)$$

are minimal. Due to using a logarithmic grid in r we use the formula

$$r = r_0 (1 + \epsilon)^I \Leftrightarrow I = \log \frac{r}{r_0} \frac{1}{\log 1 + \epsilon}, \quad (3.61)$$

where I is the index of r in the grid, r_0 is the lowest radius and $1 + \epsilon$ is a constant of the logarithmic grid. For r we employ equation (3.61) to determine I . As the result might not be an integer, we need a modulus operandi to arrive at one. Here, we always round-off the integer resulting in always arriving at I such that $r_I \leq r$ (r_I is the radius corresponding to the determined index). On top of that it is made sure that $I \in [0, I_{\max}]$ as given by the PLUTO data. The same is done for the other two coordinates but due to them using equidistant coordinates we can just use

$$\theta_J = \theta_0 + J\Delta\theta \Leftrightarrow J = \frac{\theta - \theta_0}{\Delta\theta} \quad (3.62)$$

$$\varphi_K = \varphi_0 + K\Delta\varphi \Leftrightarrow K = \frac{\varphi - \varphi_0}{\Delta\varphi} \quad (3.63)$$

along with the correct bounds for J and K . Depending on the chosen interpolation scheme we require a different number of grid cells separating them from the respective boundaries. When using linear interpolation and the lower index we require one cell to the right in each direction. The only special treatment is required at the last cell before the outer boundary. In this case we have to use the cell to the left. Thus for any quantity q in the PLUTO data we can determine the coefficients for the linear approximation

$$m_r = \begin{cases} \frac{q_{I+1,J,K} - q_{I,J,K}}{r_{I+1} - r_I} & \text{if } I < I_{\max} \\ \frac{q_{I,J,K} - q_{I-1,J,K}}{r_I - r_{I-1}} & \text{if } I = I_{\max} \end{cases} \quad (3.64)$$

$$m_\theta = \begin{cases} \frac{q_{I,J+1,K} - q_{I,J,K}}{\theta_{J+1} - \theta_J} & \text{if } J < J_{\max} \\ \frac{q_{I,J,K} - q_{I,J-1,K}}{\theta_J - \theta_{J-1}} & \text{if } J = J_{\max} \end{cases} \quad (3.65)$$

$$m_\varphi = \begin{cases} \frac{q_{I,J,K+1} - q_{I,J,K}}{\varphi_{K+1} - \varphi_K} & \text{if } K < K_{\max} \\ \frac{q_{I,J,K} - q_{I,J,K-1}}{\varphi_K - \varphi_{K-1}} & \text{if } K = K_{\max} \end{cases} \quad (3.66)$$

With this the final result will be

$$q_{\text{interpol}} = q_{I,J,K} + m_r(r - r_I) + m_\theta(\theta - \theta_J) + m_\varphi(\varphi - \varphi_I). \quad (3.67)$$

If we determine ρ_{interpol} , $v_{x\text{interpol}}$, $v_{y\text{interpol}}$ and $v_{z\text{interpol}}$ from the PLUTO data and combine it with the particle velocities in order to determine the relative velocity vector we can use equation (2.187) to determine the drag acceleration vector. It should be noted that in the case of only one cell in any of the dimensions, the corresponding linear interpolation factor has to be left out from the calculation because of vanishing denominators.

3.6.1.2. Estimation of the drag acceleration derivatives

As also the time derivative of the drag acceleration vector is required this also needs to be estimated. For this purpose we chose to use a finite difference scheme. We chose to use a three-point backward difference i.e.

$$f'(t_n) = \frac{3f(t_n) - 4f(t_{n-1}) + f(t_{n-2})}{t_{n-2} - 4t_{n-1} + 3t_n} + \mathcal{O}((t_{n-2} - t_n)^2), \quad (3.68)$$

where $f(t)$ is a t dependent function defined on a time-grid (i.e. $f_0 = f(t_0), \dots, f_{n-1} = f(t_{n-1})$), $f'(t)$ is its time derivative and t_n denotes the n -th timestep. As the time-step is usually not constant in our case we opted not to assume an equidistant time-grid. In the case of an equidistant grid (i.e. $t_n - t_{n-1} = t_{n-1} - t_{n-2} = h$) equation (3.68) takes the more familiar form

$$f'(t_n) = \frac{3f(t_n) - 4f(t_{n-1}) + f(t_{n-2})}{2h} + \mathcal{O}(h^2). \quad (3.69)$$

The order of this scheme should be sufficient as a start to serve the 4th order Hermite scheme of NBODY6++GPU. In the future, higher orders could be used. During the run this needs to be calculated for all components of the drag acceleration vector which will give us the three components of the derivative of the drag acceleration. Moreover, it requires us to develop the code such that we store the last two drag acceleration vectors along with the corresponding times for particles moving in the data-domain. Easily one can see that this means that we can only assign a derivative when the particle has had a history of two previous time-steps. This already hints that there are limits to this as explained in the next subsection.

3.6.1.3. Selection criteria

In the case of analytic drag acceleration calculations one can freely chose which part of the whole computational domain should be considered for these (i.e. by disk density threshold, height limits etc.). In contrast, when loading hydrodynamical data we are restricted to the domain supplied by that data. We thus choose to ignore particles that are not contained within the space spanned by the hydrodynamical data. Furthermore, as the drag acceleration history of a particle is required particles need to be ignored two times even when they are moving in the disk (The drag acceleration and time values are, however, stored). This requirement is obviously tied to the finite difference scheme employed to determine the derivative. The number of steps required may thus change when using different schemes.

3.6.1.4. Implementation

The module used is centred around a single Fortran type (class-like object introduced in newer Fortran versions). This type is used to store all the relevant information

like the Q used, the total particle number or the array containing the data read-in from the PLUTO simulation. On top of initialising these values it is also ready to change them or read-in a different datafile. This is especially important if the units the calculation is done in should change in the course of the NBODY6++GPU simulation or the new datafile uses different hydrodynamical units. The initial parameters given are also used to pre-calculate as many constant terms as possible. Apart from the structure holding the hydrodynamical data, the object storing the particle history data is the most important part of the type. The history is needed in order to calculate the derivatives of the drag acceleration as described before. As the integer array “NAME” stores the unchanging name-integer of each particle, the data-structure of an associative container was chosen to store the information. As a container like that is not readily available in Fortran, an interface to the C++-STL (Standard template library) container “unordered_map” was chosen. For more information see e.g. http://www.cplusplus.com/reference/unordered_map/unordered_map/ or the C++-Standard document. This container works on a “key-value” basis which means the elements are not accessed by their index, but by their unique “key”. In the current application it is logical to choose an integer “key” in the form of the “NAME” entry for each particle. For the value, we save the critical information needed for each particle in an STL “vector” container of double precision floating point numbers. The critical information consists of the data on the time at the last time-step as well as the components of the drag acceleration vector. Because a 2nd-order backward difference (i.e. a finite difference) is the scheme mainly used we store the data of the last two time-steps in the array, meaning we have a “vector” with 8 entries. This is sufficient as these quantities are always known for the current time-step. We are using “unordered_map” instead of the standard “map” because “unordered_map” uses a hashtable to retrieve the entries minimising lookup time at the price of not having an continuous data-alignment in memory. This is favourable over all other retrieval strategies as an integer cannot be mapped to an array index because it might be negative or zero (Fortran arrays start at element 1). These cases really occur in NBODY6++GPU e.g. when new binaries are generated and thus no direct “NAME” entry to index array mappings are possible. The algorithm used to determine the drag acceleration vector and its derivatives works as described in Fig. 3.44. At program startup, the type “readPLUTOPythonProcessed” is initialised with user supplied information, the PLUTO data as well as some constants from the simulation. As mentioned before all of this can be changed anytime. This algorithm is called for every single particle that appears in the “drag force” routine. This routine supplies the current position vector, velocity vector and “NAME” entry of the particle along with the current time. In the following, a routine is called that calculates the indices in the grid closest to the given position. Furthermore, it is determined whether the particle is in the data range loaded from PLUTO. If it is not, the particle’s data is removed from the container and zero is returned for both drag acceleration as well as its derivative. If the particle is in the data range the drag acceleration is calculated from the interpolated density and relative velocities. Next, the routine checks whether there are enough previous time-steps stored for the particle. If not, the drag acceleration

vector is saved along with the current time for later use and again zero is returned. If, however, the request ends in the affirmative, the finite difference method described previously is used to determine the derivative of the drag acceleration vector. In this case, both of them are returned with their proper, non-zero values. Before that, the current drag acceleration and time is incorporated into the history which might involve deleting old time steps and shifting data. The next relevant task is the inclusion of this scheme into the MPI communication used in the NBODY6++GPU code. We have to synchronise all the containers between all the different processes. In order to do that we incorporate the data into the so-called “XMPI” scheme which already manages sending the various relevant quantities to all other MPI processes. The history data is extracted for each particle and is sent, along with its “NAME” integer entry, to the other process. On the other end, the history is added to the correct particle using the “NAME” identifier. This scheme is possible as each particle’s data can only be changed once per time-step after which the MPI communication is executed.

3.6.2. Extrapolation of hydrodynamic simulation data to smaller radii

Because the simulations in Kennedy et al. (2016) are done using much deeper inner radii than the 0.11 pc used in the hydrodynamical simulations we employ an extrapolation of the simulation data for $r \leq 0.11$ pc. Because we only need ρ , v_r , v_θ and v_φ (actually we need the Cartesian vectors but they can easily be determined from the spherical ones) the extrapolation will be limited to these quantities. Fitting using the standard Levenberg-Marquardt algorithm is used for this purpose. For ρ we execute a fit for every θ value (i.e. $\theta = \text{const}$ during the fit) employing the function

$$\rho(r) = \rho'_0 r^p, \quad (3.70)$$

where ρ'_0 is a fitting parameter with units $[\text{g cm}^{-3-p}]$, r is the spherical radius. In this way we can determine all needed parameters in one fit instead of doing a radial fit followed by a vertical fit. Both the v_r and v_θ are fitted to a general power law

$$v_R \text{ or } v_\theta = aR^p, \quad (3.71)$$

where a and p are fitting parameters. As v_φ is mostly keeping its Keplerian shape we fit the function

$$v_\varphi = ar^{-\frac{1}{2}}, \quad (3.72)$$

where a and p are fitting parameters. The so determined parameters h , ρ'_0 , a_r , a_θ and a_φ are used to calculate ρ , v_r , v_θ and v_φ for smaller r values. If no convergence can be reached for any given fit the corresponding parameters are all set to zero. In order to minimise problems stemming from oscillations in the self-gravitating case as seen in Subsection 3.5.2 we will limit the fitting to the radial range $r \leq R_{\text{SG}}$ where no oscillations are present after equilibration as once more determined in Subsection 3.5.2. Fig. 3.45 displays an example of this extrapolation for a 2D simulation with self-gravity

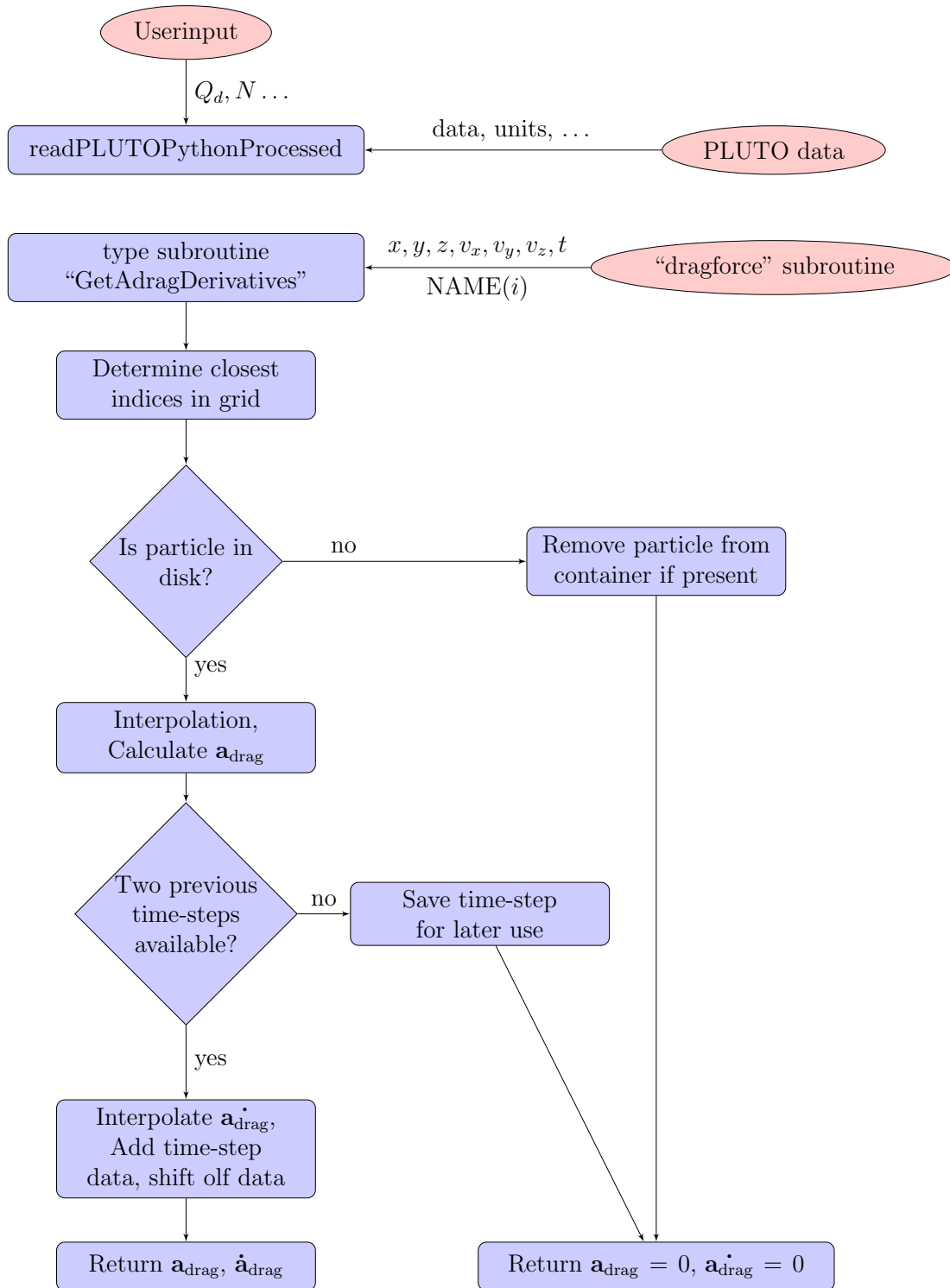


Figure 3.44.: Figure illustrating the algorithm to determine the drag acceleration vector and its derivative from grid-based data obtained from simulations with the PLUTO code. Determine the closest grid indices, if the particle is not in disk then return zero and remove from data structure if present, Otherwise, do interpolation to calculate the drag acceleration, if two previous are not time-steps present, save the drag acceleration and time and return 0, otherwise calculate derivative and return proper values

3. Numerical simulations using the PLUTO code and NBODY6++GPU

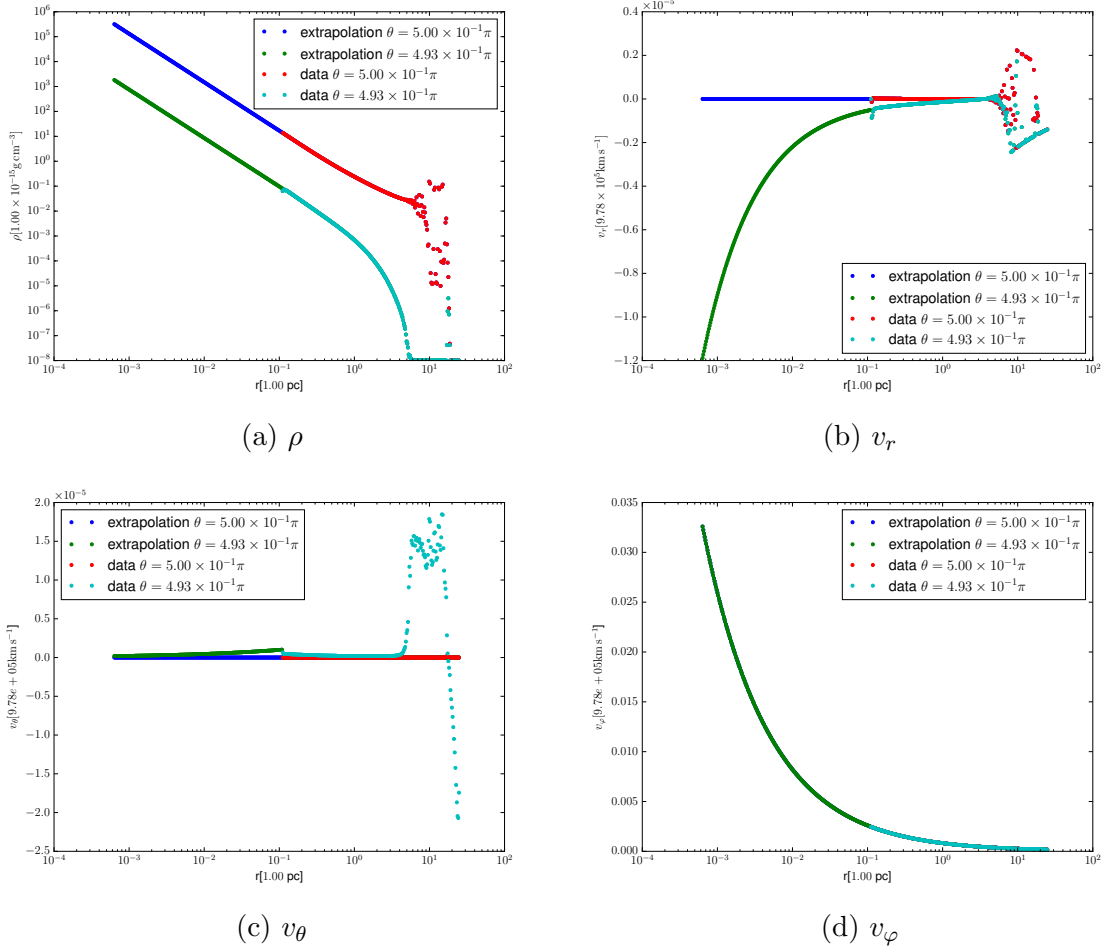


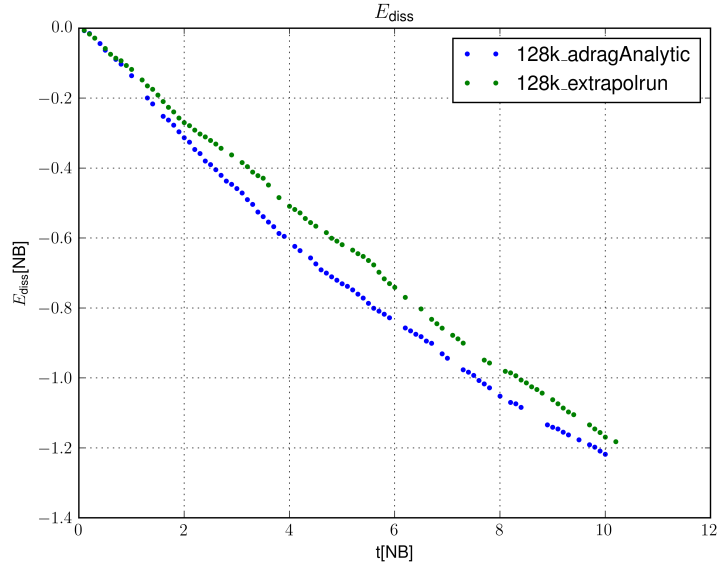
Figure 3.45.: Example for the extrapolation of ρ , v_r , v_θ and v_ϕ from a 2D simulation including self-gravity with $\alpha_{K10} = 2.0 \times 10^{-1}$ for two θ values, after 3.06×10^6 yrs

and $\alpha_{K10} = 2.0 \times 10^{-1}$ after 3.06×10^6 yrs. The density extrapolation displayed in Fig. 3.45a is very seamless and does not show any problems. The v_r extrapolation showcased in Fig. 3.45b looks quite well for the $\theta < \frac{\pi}{2}$ plot as it nicely continues the shape. However, the extrapolation in the equatorial plane shows slight deviations in the shape, but generally follows the almost zero line making the extrapolation useful. The least well extrapolation can be seen in Fig. 3.45c for v_θ . While things are fine for the equatorial plane, the curvature seems slight wrong outside of it. Despite of that the extrapolation should still be useful as the divergence is $\leq 1 \text{ km s}^{-1}$ and v_θ is a lot smaller than v_ϕ and its absolute value is smaller than v_r close to 0.11 pc where the original radial boundary is. In contrast to this, the extrapolation for v_ϕ displayed in Fig. 3.45d the curve is slightly too high outside of the equatorial plane. Nonetheless, the small scale of the discrepancies makes this problem a bearable one. Overall, the extrapolations are safe to use as shown here.

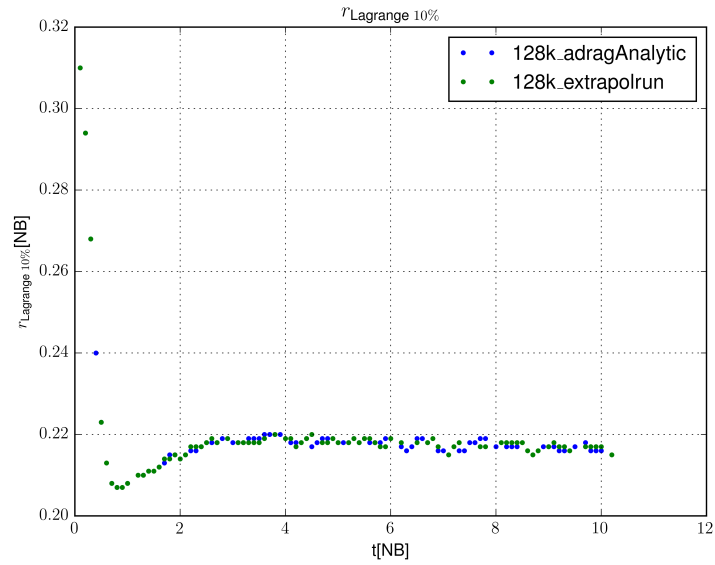
3.6.3. First preliminary test

In order to verify the code we performed two simulations with 128×10^3 particles with equal mass using a Plummer distribution equilibrated with a Super Massive Black Hole (SMBH) potential present that is also still present during the run. Additionally, we choose 2.12 pc as the basis length and $11\,718.75 M_{\odot}$ as the basic mass unit. The mass unit is chosen such that the total cluster mass is $1.5 \times 10^9 M_{\odot}$ and the SMBH mass is $1.5 \times 10^8 M_{\odot}$ akin to the M31 system used earlier. While this is not important for the N-body simulation, it is needed for converting the code units of PLUTO to the N-body units. Moreover, we choose R_{accr} (radius where a star is labelled as “accreted”) of 3.0×10^{-4} in N-body units. In one simulation, the analytical formulas for the drag acceleration and its derivative were used. In contrast, the other simulation used data from PLUTO containing the analytic profiles for density and the velocities as initial conditions. Additionally, the PLUTO data was extrapolated up $R = R_{\text{accr}}$ to confirm the extrapolation is working correctly one more time. It should be noted that we thus use the interpolation on the density and velocity profiles and also make use of the before-mentioned finite difference method in order to calculate the derivative of the drag acceleration. Both simulations were run up to 10.0 N-body time units as a test. Comparative plots of the dissipation energy E_{diss} (Energy lost to the drag forces) as well as the Lagrange radius containing 10% of the total cluster mass were created and are depicted in Fig. 3.46. When looking at the plot of the time evolution of the Lagrange radius containing 10% of the total mass, Fig. 3.46b reveals that the radius is very similar for the analytic formula and the interpolation of the initial conditions. There are some discrepancies in the initial drop, but then they are quickly aligning and equilibrate to the same value after about two N-Body time units. The very small discrepancies are expected because of the errors that came with interpolation. The dissipated energy displayed in Fig. 3.46a is quite the same for the analytic and the interpolated case up to $t \approx 1\text{NB}$, the interpolated simulation seems to underestimate the dissipated energy due to the drag forces. An explanation for this could be that only particles who have spent three consecutive time-steps in the data range are assigned a non-zero value for both the drag acceleration vector and its time derivative. While the slopes are also very much the same up to 1NB unit, they diverge a bit afterwards, but not by a large factor. Summed up these results are quite encouraging as no unexpected discrepancies occur between critical values of the two simulations. The next step is now to replace the initial conditions by a simulation more advanced in time.

3. Numerical simulations using the PLUTO code and NBODY6++GPU



(a) E_{diss}



(b) $R_{\text{lagr}10\%}$

Figure 3.46.: Comparative plots of E_{diss} and $R_{\text{lagr}10\%}$ (Radius within which 10% of the total mass are contained) determined from a simulation with 128×10^3 particles with equal with a position and velocity distribution of a Plummer sphere equilibrated to a SMBH present at the centre using $3.0 \times 10^{-4}[NB]$ as the radius a star is considered accreted to the SMBH (R_{accr}). Data was extrapolated to the centre up to $R = R_{\text{accr}}$.

4. Conclusions and Outlook

4.1. Conclusions for the hydrodynamical simulations with PLUTO

We have successfully performed hydrodynamical simulation of a numerical model of an Shakura and Sunyaev (1973)-style Accretion Disk (AD) in an Active Galactic Nucleus (AGN) in two and three dimensions with and without self-gravity. While most other simulations only cover two dimensions and only deal with a very limited radial range we have here produced a three dimensional set of self-consistent models of the AD. The initial conditions inferred were determined using a static-state approach. It was possible for the system to reach an equilibrium state within $\approx 1.0 \times 10^5$ yrs (without self-gravity) or $\approx 5 \times 10^5$ yrs (with self-gravity). As seen in Section 3.4 a almost perfect equilibrium is reached relatively quickly and no oscillations disturb the system without including self-gravity. For the simulations with self-gravity, as to be seen in Section 3.5, we were also able to reach an equilibrated state and could even confirm the change in scale-height R dependency from Shakura and Sunyaev (1973). There are non-subsiding oscillations which, however, do not significantly slow down the simulation or cause problems like strong shocks. As unfavourable as this may seem, the oscillations are actually the embodiment of the Toomre stability criterion as discussed in Subsection 2.3.10. The onset of the oscillations is almost exactly at the radius predicted by equation (3.31). This is an encouraging result as this shows that our simulation is governed by physical effects and not numerical effects. We later discuss how the oscillations could be prevented. The primary change after equilibration compared to the initial conditions was that the linear constant of the scale-height dropped from

$$\left(\frac{h}{R}\right)_{\text{initial}} \approx 8.46 \times 10^{-3} \quad (4.1)$$

to

$$\left(\frac{h}{R}\right)_{\text{end}} \approx 6.6 \times 10^{-3} \quad (4.2)$$

in the regime where self-gravity is not an important. This shows that the initially chosen constant using the arguments from Just et al. (2012), Kennedy et al. (2016) is not exactly correct, but is in the correct range. This is a confirmation of the model used in Just et al. (2012), Kennedy et al. (2016). Moreover, we were able to confirm that the self-gravity changes the scale-height from linear growing in R to constant in

4. Conclusions and Outlook

R. Some averaging was necessary due to the oscillations, but this was manageable quite well. This mostly confirms the assumption made about this in Kennedy et al. (2016) and greatly showcases the gradual change (as opposed to the abrupt change in Kennedy et al. (2016)). This is expected as the self-gravity is slowly growing to match and eventually surpass the gravity of the central Super Massive Black Hole (SMBH). Another aspect is the integrated radial mass flow which can be seen as a precursor for the accretion rate. In Shakura and Sunyaev (1973) and also Kennedy et al. (2016) the accretion rate is assumed to be constant. Despite not enforcing an value via an inflow from the outer boundary we still end up with a more or less constant value, which is even quite close to the determined value by using the profiles derived in Shakura and Sunyaev (1973). We can also see slight differences between different α values. This is something requiring more investigation as the differences are not this pronounced. This is very encouraging as it again confirms educated assumptions and we reach, despite of some problems, a state that closely resembles the theoretical predictions. Interestingly, the self-gravity seems to stabilise the radial mass flow as less oscillations can be seen. Additionally, we could see that full three dimensional simulations are a little less oscillation prone. However, more numerical experiments have to confirm this first. Furthermore, the axis-symmetry is mostly preserved in all three dimensional simulations mostly justifying analysing the axisymmetric two dimensional simulations without losing much information. Still, more three dimensional simulations would be beneficial to further investigate the system. Also, three dimensional data is best suited for combining it with simulations using NBODY6++GPU.

4.2. Conclusions for the hydrodynamical simulations with NBODY6++GPU

A module for NBODY6++GPU was written to read the data obtained in the earlier hydrodynamical simulations. In addition we were able to run a first preliminary test simulation with this module employing the analytic initial conditions as data from the PLUTO code. We could confirm that the module is working within the expected tolerances. This was proven by looking at the dissipated energy as well of the Lagrange radius in which 10% of the total star mass is contained. This now allows us to proceed to using real simulation data to arrive of significant physical results. The module was written in such a way that alterations and additions are easily possible.

4.3. Outlook

The first issue which should be addressed in future work is the lack of three dimensional simulations running 1.0×10^7 yrs and a variety of α values. For this purpose we could try to obtain computational resources capable of supplying roughly 5000 cores in order to reach the same grid cells per process for 30 grid points in the φ direction as for the two-dimensional simulations. It would also be interesting to increase the

number of grid points in the φ direction to see if this might break axis-symmetry. Another possible approach is to make use of the adaptive mesh refinement for PLUTO as described in Mignone and Zanni (2012). This would allow to tailor the grid to our problem making calculations more efficient. Of course, this would require answering the question what should be the basis for the adaptive mesh refinement. I.e. where the mesh should be fine and where coarse. Currently, we just assume that the inner parts require more resolution and are hence using a logarithmic grid with decreasing cell size towards the centre. The first step in this would be to make cells in the ignored region where $\rho_{\text{initial}} \leq \rho_{\text{min}}$ a lot coarser. Another point is the introduction of stars crossing the disk which would introduce heating into the disk. PLUTO already offers a mechanism for this, so future work could address this by reading data determined from NBODY6++GPU simulations. It would then just be added as another source term. Alternatively, one could strive to speed up the PLUTO calculations by e.g. including an GPU as an accelerator or profiling backed alterations of the code. This would also involve the inclusion of the modules developed by Rolf Kuiper (Kuiper et al. 2018, submitted; 2010a;b; 2011) into this process. The second most interesting area for future work is the inclusion of the radiative pressure into the simulation. While it can be simply activated in the “Makemake” module its correct treatment also involves looking at the equations of state and find a set of equilibrium initial conditions including. This is because some of the assumptions in the derivation of the current initial conditions, such as the vertically constant sound-speed, are no longer valid if radiation pressure and a proper equation of state is considered. Apart from a more correct force balance this would also supply information on the radiation pressure dominated and gas pressure dominated region boundaries which could be compared to Shakura and Sunyaev (1973). Likewise, the different sound-speed might stabilise the Accretion Disk (AD) bringing more of it in the region predicted to be stable by the Q_{Toomre} . Moreover, the temperature determined in this process can be compared to other estimations of it, e.g. in Collin-Souffrin and Dumont (1990). Furthermore, it could be used together with the already existing opacity treatment in “Makemake”, to determine spectra generated by the disk. These could than be compared to observations of real Active Galactic Nuclei (AGN) in the universe enabling direct comparison with nature. While the Special Theory of Relativity (STR) and General Theory of Relativity (GTR) effects are not treated yet information on the Broad Line Emitting Region (BLR) and Narrow Line Emitting Region (NLR) could be extracted. This open up another possibility to enhance the model in the future. PLUTO already posses a module for special-relativistic calculations which could be activated. However, this would require to also adjust the additional modules to be able to treat STR. A full treatment of the system would also involve the treatment of magnetic fields as well as GTR. While the first one might be feasible with PLUTO, GTR effects would require a different code or significant changes to PLUTO.

The next step for the NBODY6++GPU simulations is the usage of equilibrated snapshots later in time instead of just using the initial conditions used as a test case in order to verify the method. For this purpose we need to address the oscillations appearing in the outer parts of the disks as they might cause problems because of the

4. *Conclusions and Outlook*

strongly-varying density in this region. This would affect the interpolation of the density and thus the drag acceleration. Furthermore, a star moving through that part will experience very different drag forces (and thus drag acceleration) which would create problems for the finite difference calculation to determine the derivative of the drag acceleration. It would be possible to use an approach similar to the extrapolation that involves fitting. One would need to be a bit more careful because of the change of the scale height in that area. This will be addressed in future work shortly and we expect to have results in the near future. As flexibility was a great concern when writing the module, future work can profit a lot from this module. It is easily possible to add new time or space interpolation schemes or to use data provided by another great. The ultimate goal, however, would be to incorporate the hydrodynamic calculations into the NBODY6++GPU calculations creating a true mutual feedback between Nuclear Star Cluster (NSC) and AD.

Acknowledgements

First and foremost, I want to thank my supervisor Rainer Spurzem for the opportunity of this thesis. Without his continuing support and advice throughout all unforeseen complications this thesis would not have been possible. Moreover, he gave me the opportunity to meet many interesting and great people at interesting places. Furthermore, I want to thank my second supervisor, Andreas Just, who offered lots of helpful discussions and advice along with handling the administrative tasks if Rainer was not available. A big thank you also goes out to Yohai Meiron who has often times helped with the debugging of my code and gave useful insights on the consequences of problems and features observed in my data as well as proofreading this thesis. A special thank you goes to Martin Bies and René Heß who offered their time to proofread larger parts of this thesis. Additionally, I want to extend a warm thank you to Li Shuo and all members of the team in Beijing for their warm welcome, excursions and efforts to make my stays in Beijing a great experience. Also, I am grateful to all the members of the ARI lunch squad, where I learned a lot about many topics and was always blessed with good company for lunch. Moreover, I want to thank all of the ARI's administrative and IT staff for their support and care in the last 3.5 years. A very heartfelt thank you goes to all of my friends who were always there to talk to and as a very welcome distraction from stressful situations. I would not be where I am now without you. Last but not least, my deepest gratitude goes to my mother Gabriele Maria Hahn as well as the rest of my family, blood-related or not, for their unwavering support throughout my studies and the insurance that I will always have a home to return to, no matter the circumstances. This especially applies to the my closest family Gabriele Maria Hahn, Hans-Dieter Hahn, Sabine Jasiulek-Lauscher, Bruno Lauscher, Theresia Jasiulek, Paul-Josef Jasiulek and Wolfgang Klein.

A. List of Acronyms

AGN Active Galactic Nucleus

AD Accretion Disk

NSC Nuclear Star Cluster

HIL High Ionisation Lines

BLR Broad Line Emitting Region

NLR Narrow Line Emitting Region

SMBH Super Massive Black Hole

MHD Magneto Hydrodynamics

rms root mean square

MW Milky Way

quasar Quasi-stellar radio source

FLD Flux Limited Diffusion

STR Special Theory of Relativity

GTR General Theory of Relativity

,

B. Bibliography

- S. J. Aarseth. *Gravitational N-Body Simulations*. Oct. 2003.
- A. Agnello. Quasar lenses and galactic streams: outlier selection and Gaia multiplet detection. *Monthly Notices of the Royal Astronomical Society*, 471(2):2013–2021, 2017. doi: 10.1093/mnras/stx1650. URL <http://dx.doi.org/10.1093/mnras/stx1650>.
- S. Balay, S. Abhyankar, M. F. Adams, J. Brown, P. Brune, K. Buschelman, L. Dalcin, V. Eijkhout, W. D. Gropp, D. Kaushik, M. G. Knepley, L. C. McInnes, K. Rupp, B. F. Smith, S. Zampini, H. Zhang, and H. Zhang. PETSc Web page. <http://www.mcs.anl.gov/petsc>, 2016. URL <http://www.mcs.anl.gov/petsc>.
- S. A. Balbus and J. C. B. Papaloizou. On the Dynamical Foundations of α Disks. *Astrophysical Journal*, 521:650–658, Aug. 1999. doi: 10.1086/307594.
- D. C. Black and P. Bodenheimer. Evolution of rotating interstellar clouds. I - Numerical techniques. *Astrophysical Journal*, 199:619–632, Aug. 1975. doi: 10.1086/153729.
- G. R. Burbidge. Galactic Explosions as Sources of Radio Emission. *Nature*, 190: 1053–1056, June 1961. doi: 10.1038/1901053a0.
- A. G. W. Cameron. Star Formation in Elliptical Galaxies and Intense Radio Sources. *Nature*, 194:963–964, June 1962. doi: 10.1038/194963a0.
- J. Castor. *Radiation Hydrodynamics*. Radiation Hydrodynamics. Cambridge University Press, 2004. ISBN 9780521540629. URL <https://books.google.de/books?id=J48PULzdgSgC>.
- P. Colella, D. T. Graves, J. N. Johnson, H. S. Johansen, N. D. Keen, T. J. Ligocki, D. F. Martin, P. W. Mccorquodale, D. Modiano, P. O. Schwartz, T. D. Sternberg, and B. V. Straalen. Chombo software package for AMR applications design document. Technical report, 2003.
- S. Collin-Souffrin. Theoretical studies of the line emission spectrum. In G. Swarup and V. K. Kapahi, editors, *Quasars*, volume 119 of *IAU Symposium*, page 295–304, 1986.
- S. Collin-Souffrin. Line and continuum radiation from the outer region of accretion discs in active galactic nuclei. I - Preliminary considerations. *Astronomy and Astrophysics*, 179:60–70, June 1987. Litresearch2016.

B. Bibliography

- S. Collin-Souffrin and A. M. Dumont. Line and continuum emission from the outer regions of accretion discs in active galactic nuclei. II - Radial structure of the disc. *Astronomy and Astrophysics*, 229:292–328, Mar. 1990.
- R. Courant, K. Friedrichs, and H. Lewy. Über die partiellen Differenzgleichungen der mathematischen Physik. *Mathematische Annalen*, 100(1):32–74, 1928. ISSN 0025-5831. doi: 10.1007/BF01448839. URL <http://dx.doi.org/10.1007/BF01448839>.
- B. Czerny, Y.-R. Li, J. Sredzinska, K. Hryniewicz, S. Panda, C. Wildy, and V. Karas. Self-Consistent Dynamical Model of the Broad Line Region. *Frontiers in Astronomy and Space Sciences*, 4:5, 2017. ISSN 2296-987X. doi: 10.3389/fspas.2017.00005. URL <https://www.frontiersin.org/article/10.3389/fspas.2017.00005>.
- K. Davidson and H. Netzer. The emission lines of quasars and similar objects. *Reviews of Modern Physics*, 51:715–766, Oct. 1979. doi: 10.1103/RevModPhys.51.715.
- A. M. Dumont and S. Collin-Souffrin. Line and continuum emission from the outer regions of accretion discs in active galactic nuclei. III. Influence of the illumination model. *Astronomy and Astrophysics*, 229:302, Mar. 1990a.
- A. M. Dumont and S. Collin-Souffrin. Line and Continuum Emission from the Outer Regions of Accretion Discs in Active Galactic Nuclei - Part IV - Line Emission. *Astronomy and Astrophysics*, 229:313, Mar. 1990b.
- M. Elitzur and H. Netzer. Disc outflows and high-luminosity true type 2 AGN. *Monthly Notices of the Royal Astronomical Society*, 459(1):585–594, 2016. doi: 10.1093/mnras/stw657. URL <http://dx.doi.org/10.1093/mnras/stw657>.
- A. Evans. <https://www.flickr.com/photos/astroporn/4999978603/>, 09 2010.
- M. M. Fausnaugh, B. M. Peterson, D. A. Starkey, K. Horne, and t. A. S. C. . Continuum Reverberation Mapping of AGN Accretion Disks. *Frontiers in Astronomy and Space Sciences*, 4:55, 2017. ISSN 2296-987X. doi: 10.3389/fspas.2017.00055. URL <https://www.frontiersin.org/article/10.3389/fspas.2017.00055>.
- Fogasy, J., Knudsen, K. K., Lagos, C. D. P., Drouart, G., and Gonzalez-Perez, V. On the frequency of star-forming galaxies in the vicinity of powerful AGNs: The case of SMM J04135+10277. *A&A*, 597:A123, 2017. doi: 10.1051/0004-6361/201628173. URL <https://doi.org/10.1051/0004-6361/201628173>.
- M. Forum. MPI Web page. <http://www.mcs.anl.gov/research/projects/mpi/>, 2018. URL <http://www.mcs.anl.gov/petsc>.
- J. E. Gunn. On the Distances of the Quasi-Stellar Objects. *Astrophysical Journal, Letters*, 164:L113, Mar. 1971. doi: 10.1086/180702.
- J. E. Gunn and B. A. Peterson. On the Density of Neutral Hydrogen in Intergalactic Space. *Astrophysical Journal*, 142:1633–1641, Nov. 1965. doi: 10.1086/148444.

- S. L. a. Hans Petter Langtangen. *Finite Difference Computing with PDEs: A Modern Software Approach*. Texts in Computational Science and Engineering 16. Springer International Publishing, 1 edition, 2017. ISBN 978-3-319-55455-6, 978-3-319-55456-3. URL <http://gen.lib.rus.ec/book/index.php?md5=7FB3AB803CEFBB4E500329021949000C>.
- K. D. Horne and Agn Storm Team. AGN Space Telescope and Optical Reverberation Mapping Project. IV. Velocity-Delay Mapping of Broad Emission Lines in NGC 5548. In *American Astronomical Society Meeting Abstracts #225*, volume 225 of *American Astronomical Society Meeting Abstracts*, page 103.04, Jan. 2015.
- F. Hoyle and W. A. Fowler. On the nature of strong radio sources. *Monthly Notices of the Royal Astronomical Society*, 125:169, 1963a. doi: 10.1093/mnras/125.2.169.
- F. Hoyle and W. A. Fowler. Nature of Strong Radio Sources. *Nature*, 197:533–535, Feb. 1963b. doi: 10.1038/197533a0.
- D. Hutsemékers, L. Braibant, D. Sluse, T. Anguita, and R. Goosmann. New Constraints on Quasar Broad Absorption and Emission Line Regions from Gravitational Microlensing. *Frontiers in Astronomy and Space Sciences*, 4:18, 2017. ISSN 2296-987X. doi: 10.3389/fspas.2017.00018. URL <https://www.frontiersin.org/article/10.3389/fspas.2017.00018>.
- G.-S. Jiang and C.-W. Shu. Efficient Implementation of Weighted ENO Schemes. *Journal of Computational Physics*, 126(1):202–228, 1996. ISSN 0021-9991. doi: 10.1006/jcph.1996.0130. URL <http://www.sciencedirect.com/science/article/pii/S0021999196901308>.
- A. Just, D. Yurin, M. Makukov, P. Berczik, C. Omarov, R. Spurzem, and E. Y. Vilkoviskij. Enhanced Accretion Rates of Stars on Supermassive Black Holes by Star-Disk Interactions in Galactic Nuclei. *The Astrophysical Journal*, 758:51, Oct. 2012. doi: 10.1088/0004-637X/758/1/51.
- K. I. Kellermann, R. Sramek, M. Schmidt, D. B. Shaffer, and R. Green. VLA observations of objects in the Palomar Bright Quasar Survey. *Astronomical Journal*, 98: 1195–1207, Oct. 1989. doi: 10.1086/115207.
- G. F. Kennedy, Y. Meiron, B. Shukirgaliyev, T. Panamarev, P. Berczik, A. Just, and R. Spurzem. Star-disc interaction in galactic nuclei: orbits and rates of accreted stars. *Monthly Notices of the Royal Astronomical Society*, 460:240–255, July 2016. doi: 10.1093/mnras/stw908.
- A. E. Kimball, M. Lacy, C. J. Lonsdale, and J.-P. Macquart. ALMA detection of a disc-dominated [C ii] emission line at $z=4.6$ in the luminous QSO J1554+1937. *Monthly Notices of the Royal Astronomical Society*, 452(1):88–98, 2015. doi: 10.1093/mnras/stv1160. URL <http://dx.doi.org/10.1093/mnras/stv1160>.

B. Bibliography

- F. Klein. Efficiency and robustness of selected numerical solvers for modelling relativistic hydrodynamics in astrophysics. Master's thesis, Sept. 2014.
- J. Kristian. Quasars as Events in the Nuclei of Galaxies: the Evidence from Direct Photographs. *Astrophysical Journal, Letters*, 179:L61, Jan. 1973. doi: 10.1086/181117.
- R. Kuiper, H. Klahr, H. Beuther, and T. Henning. Circumventing the Radiation Pressure Barrier in the Formation of Massive Stars via Disk Accretion. *Astrophysical Journal*, 722:1556–1576, Oct. 2010a. doi: 10.1088/0004-637X/722/2/1556.
- R. Kuiper, H. Klahr, C. Dullemond, W. Kley, and T. Henning. Fast and accurate frequency-dependent radiation transport for hydrodynamics simulations in massive star formation. *Astronomy and Astrophysics*, 511:A81, Feb. 2010b. doi: 10.1051/0004-6361/200912355.
- R. Kuiper, H. Klahr, H. Beuther, and T. Henning. Three-dimensional Simulation of Massive Star Formation in the Disk Accretion Scenario. *Astrophysical Journal*, 732: 20, May 2011. doi: 10.1088/0004-637X/732/1/20.
- R. Kuiper, H. W. Yorke, and A. Mignone. MAKEMAKE + SEDNA: A Continuum Radiation Transport and Photoionization Framework for Astrophysical Newtonian Fluid Dynamics. *Astronomy and Astrophysics*, 2018, submitted.
- J. Kwan and J. H. Krolik. The formation of emission lines in quasars and Seyfert nuclei. *Astrophysical Journal*, 250:478–507, Nov. 1981. doi: 10.1086/159395.
- P. Lira, I. Botti, S. Kaspi, and H. Netzer. Reverberation Mapping of High-z, High-Luminosity Quasars. *Frontiers in Astronomy and Space Sciences*, 4:71, 2018. ISSN 2296-987X. doi: 10.3389/fspas.2017.00071. URL <https://www.frontiersin.org/article/10.3389/fspas.2017.00071>.
- G. Lodato. Classical disc physics. *New Astronomy Review*, 52:21–41, June 2008. doi: 10.1016/j.newar.2008.04.002.
- E. Lusso and G. Risaliti. The Physical Relation between Disc and Coronal Emission in Quasars. *Frontiers in Astronomy and Space Sciences*, 4:66, 2018. ISSN 2296-987X. doi: 10.3389/fspas.2017.00066. URL <https://www.frontiersin.org/article/10.3389/fspas.2017.00066>.
- D. Lynden-Bell. Galactic Nuclei as Collapsed Old Quasars. *Nature*, 223:690–694, Aug. 1969. doi: 10.1038/223690a0.
- M. A. Malkan and W. L. W. Sargent. The ultraviolet excess of Seyfert 1 galaxies and quasars. *Astrophysical Journal*, 254:22–37, Mar. 1982. doi: 10.1086/159701. Litresearch2016 FirstDisk.

- J. E. Mejía-Restrepo, P. Lira, H. Netzer, B. Trakhtenbrot, and D. Capellupo. The Virial Factor and Biases in Single Epoch Black Hole Mass Determinations. *Frontiers in Astronomy and Space Sciences*, 4:70, 2018. ISSN 2296-987X. doi: 10.3389/fspas.2017.00070. URL <https://www.frontiersin.org/article/10.3389/fspas.2017.00070>.
- A. Mignone and C. Zanni. Adaptive Mesh Computations with the PLUTO Code for Astrophysical Fluid Dynamics. In N. V. Pogorelov, J. A. Font, E. Audit, and G. P. Zank, editors, *Numerical Modeling of Space Plasma Slows (ASTRONUM 2011)*, volume 459 of *Astronomical Society of the Pacific Conference Series*, page 346, July 2012.
- A. Mignone, T. Plewa, and G. Bodo. The Piecewise Parabolic Method for Multidimensional Relativistic Fluid Dynamics. *The Astrophysical Journal Supplement Series*, 160(1):199, 2005. URL <http://stacks.iop.org/0067-0049/160/i=1/a=199>.
- A. Mignone, G. Bodo, S. Massaglia, T. Matsakos, O. Tesileanu, C. Zanni, and A. Ferrari. PLUTO: A Numerical Code for Computational Astrophysics. *The Astrophysical Journal Supplement Series*, 170:228–242, May 2007. doi: 10.1086/513316.
- D. Mihalas and B. Weibel-Mihalas. *Foundations of Radiation Hydrodynamics*. Dover Books on Physics. Dover, 1999. ISBN 9780486409252. URL https://books.google.de/books?id=f75C_GN9KZwC.
- M. Molina. <http://www.astro.wisc.edu/~molina/index.html>, 2018.
- I. Márquez, J. Masegosa, O. González-Martin, L. Hernández-García, M. Pović, H. Netzer, S. Cazzoli, and A. del Olmo. The AGN Nature of LINER Nuclear Sources. *Frontiers in Astronomy and Space Sciences*, 4:34, 2017. ISSN 2296-987X. doi: 10.3389/fspas.2017.00034. URL <https://www.frontiersin.org/article/10.3389/fspas.2017.00034>.
- H. Netzer. Meeting summary: A 2017 view of Active Galactic Nuclei. *Frontiers in Astronomy and Space Sciences*, 5:10, May 2018. doi: 10.3389/fspas.2018.00010.
- I. D. Novikov and K. S. Thorne. Astrophysics of black holes. In C. Dewitt and B. S. Dewitt, editors, *Black Holes (Les Astres Occlus)*, page 343–450, 1973.
- M. Oda, P. Gorenstein, H. Gursky, E. Kellogg, E. Schreier, H. Tananbaum, and R. Giacconi. X-Ray Pulsations from Cygnus X-1 Observed from UHURU. *Astrophysical Journal, Letters*, 166:L1, May 1971. doi: 10.1086/180726.
- P. Padovani. Active Galactic Nuclei at All Wavelengths and from All Angles. *Frontiers in Astronomy and Space Sciences*, 4:35, 2017. ISSN 2296-987X. doi: 10.3389/fspas.2017.00035. URL <https://www.frontiersin.org/article/10.3389/fspas.2017.00035>.

B. Bibliography

- G. Richards. Application of Independent Component Analysis to Legacy UV Quasar Spectra. HST Proposal, Aug. 2017.
- E. E. Salpeter. Accretion of Interstellar Matter by Massive Objects. *Astrophysical Journal*, 140:796–800, Aug. 1964. doi: 10.1086/147973.
- M. Schartmann, K. Meisenheimer, W. Jaffe, K. R. W. Tristram, H.-W. Rix, C. Leinert, S. Morel, M. Wittkowski, H. Röttgering, G. Perrin, B. Lopez, D. Raban, W. D. Cotton, U. Graser, F. Paresce, and T. Henning. Resolving the complex structure of the dust torus in the active nucleus of the Circinus galaxy. *Astronomy & Astrophysics*, 474:837–850, Nov. 2007. doi: 10.1051/0004-6361:20078369.
- B. Schutz. *A First Course in General Relativity*. Cambridge University Press, 2009. ISBN 9781139479004. URL <https://books.google.de/books?id=GgRRt7AbdwQC>.
- N. I. Shakura and R. A. Sunyaev. Black holes in binary systems. Observational appearance. *Astronomy & Astrophysics*, 24:337–355, 1973. URL <http://adsabs.harvard.edu/abs/1973A%26A...24..337S>.
- G. A. Shields. A Brief History of Active Galactic Nuclei. *Publications of the Astronomical Society of the Pacific*, 111:661–678, June 1999. doi: 10.1086/316378.
- R. Spurzem. Direct N-body Simulations. *Journal of Computational and Applied Mathematics*, 109:407–432, Sept. 1999.
- H. Tananbaum, H. Gursky, E. Kellogg, R. Giacconi, and C. Jones. Observation of a Correlated X-Ray Transition in Cygnus X-1. *Astrophysical Journal, Letters*, 177:L5, Oct. 1972. doi: 10.1086/181042.
- K. S. Thorne and R. H. Price. Cygnus X-1 - an interpretation of the spectrum and its variability. *Astrophysical Journal, Letters*, 195:L101–L105, Feb. 1975. doi: 10.1086/181720.
- A. Toomre. On the gravitational stability of a disk of stars. *Astrophysical Journal*, 139:1217–1238, May 1964. doi: 10.1086/147861.
- E. Toro. *Riemann Solvers and Numerical Methods for Fluid Dynamics: A Practical Introduction*. Third edition edition, 2009. ISBN 978-3-540-25202-3, 978-3-540-49834-6. URL <http://gen.lib.rus.ec/book/index.php?md5=804C3366C54FE7ABDA196F82E5CB494B>.
- B. Trakhtenbrot, P. Lira, H. Netzer, C. Cicone, R. Maiolino, and O. Shemmer. Fast-Growing SMBHs in Fast-Growing Galaxies, at High Redshifts: The Role of Major Mergers As Revealed by ALMA. *Frontiers in Astronomy and Space Sciences*, 4: 49, 2017. ISSN 2296-987X. doi: 10.3389/fspas.2017.00049. URL <https://www.frontiersin.org/article/10.3389/fspas.2017.00049>.

- C. M. Urry and P. Padovani. Unified Schemes for Radio-Loud Active Galactic Nuclei. *Publications of the Astronomical Society of the Pacific*, 107:803, Sept. 1995. doi: 10.1086/133630.
- L. Wang, R. Spurzem, S. Aarseth, K. Nitadori, P. Berczik, M. B. N. Kouwenhoven, and T. Naab. NBODY6++GPU: ready for the gravitational million-body problem. *Monthly Notices of the Royal Astronomical Society*, 450:4070–4080, July 2015. doi: 10.1093/mnras/stv817.
- B. L. Webster and P. Murdin. Cygnus X-1-a Spectroscopic Binary with a Heavy Companion ? *Nature*, 235:37–38, Jan. 1972. doi: 10.1038/235037a0.
- L. D. Zanna, N. Bucciantini, and P. Londrillo. An efficient shock-capturing central-type scheme for multidimensional relativistic flows. II. Magnetohydrodynamics. *Astron. Astrophys.*, 400(astro-ph/0210618):397–414. 18 p, Oct 2002.
- Y. B. Zel’dovich. The Fate of a Star and the Evolution of Gravitational Energy Upon Accretion. *Soviet Physics Doklady*, 9:195, Sept. 1964.